Simulation-Based Combustion Noise Assessment

Investigation of CNI and CKI for Diesel Combustion

Written and conducted at the Institute of Thermal Turbomachinery and Machine Dynamics at University of Technology Graz, in association with AVL-List GmbH.

Author:	Michael Schrottner BSc.
Internal Supervisor:	Priv.-Doz. Dipl.-Ing. Dr. techn. Andreas Marn
External Supervisors:	DI Thomas Resch Ing. Christoph Schweiger

Graz, 28.07.2019

Acknowledgements

As the following pages are filled with theoretical content, on this page I want to say thank you to all people supporting me during my studies and finally, writing my diploma thesis.
First, I want to thank DI Thomas Resch for giving me the opportunity to write this interesting thesis at AVL List GmbH. Also, I want to thank Ing. Christoph Schweiger from AVL List GmbH for his support on different simulation topics.
On university side, I want to thank Priv.-Doz. Dipl.-Ing. Dr. techn. Andreas Marn for supporting me with theoretical knowledge as well as with the scripture of this thesis.
Furthermore, I want to thank my family and friends, among them colleagues from university, for their support.
In the end, I want to say special thanks to my significant other Chiara, for her great support through my years at university. Although my time was often limited, she was always insightful.

Statutory Declaration

I declare that I have authored this thesis independently, that I have not used other than the declared sources / resources, and that I have explicitly marked all material which has been quoted either literally or by content from the used sources. The text document uploaded to TUGRAZonline is identical to the present diploma thesis.

…….. ……..

Date Signature

Abstract

Noise reduction in Diesel engines is still a major task in the present time. In the course of this work, simulation models are set up as well as indices are introduced to describe certain combustion phenomenon and to characterize them in terms of combustion harshness, both directly on the cylinder pressure trace but also their effects on the engine structure as well as the radiated noise.
To describe combustion effects, a 0D thermodynamic crank angle resolved model is set up and calibrated with measurement data. Through different parameter variations parameters supporting harsh combustion are determined. Originating from the simulated pressure traces an index (CNI) to quantify the harshness of the combustions is introduced.
These cylinder pressure traces are further used as load conditions for a full flexible 3D multi body model. To evaluate the influence of the type of load application, three individual variations are introduced and investigated in terms of a forced response analysis. By means of this model the effects of different injection strategies on the vibration of the engine structure are then further investigated.
With results achieved through the multi body model, an acoustic model, which calculates the radiated noise emitted through the vibrating surfaces of the engine is introduced. This airborne noise is then analysed in terms of frequency content as well as through a second index introduced (CKI).
The toolchain is able to evaluate combustion noise regarding to harshness both in combustion simulation as well as on forced response on the structure and in airborne noise. Furthermore, it is shown that both indices feature a good correlation among each other and with results coming direct from the structure response. Additionally, it is demonstrated that CNI is very sensitive in terms of changes to the pressure gradient and should be used mainly for evaluating trends of one combustion parameter variation rather than be compared between individual cases. Due to damping characteristics of the structure which are not considered in CNI, as it sets up directly on the cylinder pressure trace, but rather are considered in CKI, as it uses actual structural response as input, it is less sensitive than CNI and provides an important supplement to combustion noise valuation.

Table of Contents

Acknowledgements I

Statutory Declaration II

Abstract III

Table of Contents IV

List of Abbreviations VII

1 Introduction 1

2 Fundamentals of Diesel Combustion 3

2.1 Injection and Its Main Control Parameters 3

2.2 Combustion and ROHR 4

3 0D-Simulation of Diesel Combustion 6

3.1 Fundamental Equations 6

3.2 Injection and High-Pressure Rail Model 10

3.2.1 Rail 11

3.2.2 Injector 11

3.2.3 Pressure Pulsation 13

3.3 Spray Model and ROHR Calculation 13

3.3.1 Spray Model 14

3.3.2 Combustion Model 19

4 Theory of Multi Body Dynamic Systems 25

4.1 General Vibration Equation 25

4.2 Reduction of Degrees of Freedom (Condensation) 29

4.2.1 Dynamic Condensation of Degrees of Freedom 29

5 Basics on Acoustic Simulation in the Free Field 32

6 Fundamentals of Acoustics and Basic Operations in Signal Processing 35

6.1 Psychoacoustics 35

6.2 Basic Operations in Signal Processing 37

6.2.1 Discrete Fourier Transformation and Its Inverse 37

6.2.2 Convolution 38

7 Theory on Combustion Noise Index Algorithm 39

8 Theory on Combustion Knocking Index Algorithm 41

8.1 Evaluation of the Loudness Level 42

8.2 Evaluation of the Modulation 43

8.3 Evaluation of the Simultaneous Masking 45

9 Software 47

9.1 Cruise™ M 47
9.2 Excite™ 47
9.2.1 Excite™ Power Unit 48
9.2.2 Excite™ Acoustics 48
10 Measurements 49
10.1 Nomenclature Definition 50
10.2 Operating Points 50
10.3 Cycle Variation During Steady State Operation 52
10.4 CNI Sensitivity in Measurements 54
10.5 Influence of Sampling Rate 58
11 Combustion Noise Assessment 59
11.1 Model Introduction 59
11.1.1 Parameters for Combustion Variation 60
11.1.2 Boundary Conditions 60
11.2 Calibration 61
11.2.1 Calibration Workflow 62
11.2.2 Validation with Measurements 65
11.3 CNI Definition 67
11.3.1 Implementation 67
11.4 CNI Evaluation on Calibrated Cylinder Pressure Traces 71
11.5 Assessment of Different Injection Strategies 71
11.5.1 Case I – Variation of Rail Pressure 72
11.5.2 Case II – Variation of SOI of Pilot Injection 76
11.5.3 Case III – Variation of Parameter Sets 81
12 Combustion Knocking Assessment 88
12.1 Multi Body Dynamic Model Introduction 88
12.2 Modelling Comparison Gas Force Application 89
12.2.1 Model Comparison Results 89
12.3 Acoustic Model Introduction 94
12.4 Injection Strategies Influencing Structural Vibrations and Radiated Noise 96
12.4.1 Calibrated Cylinder Pressure Traces 97
12.4.2 Case I – Variation of Rail Pressure 101
12.4.3 Case II – Variation of SOI of Pilot Injection 104
13 Conclusion 107
13.1 Summary 107

13.2 Outlook 108
14 List of Figures 109
15 List of Tables 113
16 References 114
17 Appendix 116
17.1 Combustion Calibration 116
17.2 MBD Model Comparison Acceleration Signal Time Domain 121
17.3 1/3 Octave Frequency Bands 124

List of Abbreviations

A	Area [m²]
c	Heat Capacity [J/kgK]
c_D	Discharge Coefficient [-]
c_s	Speed of Sound [m/s]
d	Damping [Ns/m]
E	Elastic Modulus [Pa]
E_3	3x3 Unit Matrix [-]
f	Vector of Forces [N]
f_E	Eigenfrequency [Hz]
f_z	Frequency Dependent Weighting Factor [-]
F	Factor [-]
G	Free Enthalpy (Gibbs energy) [J]
G^*	Transformation Matrix [-]
H	Enthalpy [J]
H_u	Lower Heating Value [J/kg]
I	Inertia [kgm²]
K	Bulk Modulus [Pa]
k	Stiffness [N/m]
k_A	Model Constant [-]
k_m	Model Constant [-]
k_T	Turbulent Kinetic Energy [m²/s²]
k_n	Wave Number [1/m]
l_n	Needle Lift [m]
L_{st}	Stochiometric Air Requirement [kg Air/kg Fuel]
M	Momentum [kgm/s]
m	Mass [kg]
p	Pressure [Pa]
$p1$, $p2$	Weighting Factors [-]
p^*	Non-Linear Inertia Term [N]
$\tilde{p}$	Pressure Boundary Condition [Pa]
q	Vector of Generalized Displacement [-]
Q	Heat [J]
R	Ideal Gas Constant [J/kgK]
$R_{\alpha\beta\gamma}$	Transformation Matrix [-]
r	Reaction Rate [1/s]
$\bar{r}$	Radial Position [m]
$\bar{R}$	Outer Spray Radius [m]
T	Temperature [K]
T_A	Model Constant [-]
t	Time [s]
U	Inner Energy [J]
u	Velocity [m/s]
$\bar{u}$	Specific Inner Energy [J/kg]

V	Volume [m^3]
v	Specific Volume [m^3/kg]
$\tilde{v}_n$	Normal Velocity Boundary Condition [m/s]
W	Work [J]
$\tilde{Z}_n$	Impedance Boundary Condition [$kg/(m^2s)$]

Greek letters

ϑ	Spray Angle [rad]
λ	Air Fuel Ratio [-]
Φ	Mass Fraction [-]
φ	Crank Angle [deg]
μ	Mass Ratio [-]
ρ	Density [kg/m^3]
ω	Angular Velocity [rad/s]
Ω	Calculation field [-]
Γ	Boundary Condition Field [-]
ζ	Flow Coefficient [-]

Subscript

ABS	Absolut
Acc	Acceleration
Arr	Arrhenius
cl	Spray Centerline
cyl	Cylinder
diff	Diffusion
ex	Exhaust
ext	External
f	Fuel
F	Force
gyros	Gyroscopic
ign	Ignition
in	Intake
inj	Injection
int	Internal
Leak	Leakage
M	Moment
m	Molar
Mag	Magnussen
mix	Mixture
NH	Nozzle hole
NS	Needle seat
p	Pressure
pre	Premixed
r	Radial Position of Spray

R	Outer Spray Radius
rb	Rigid Body
sp	Spray
T	Temperature
v	Vapor
W	Wall

Abbreviations

ABN	Air Borne Noise
AKF	Amplitude Correction Factor
BDC	Bottom Dead Center
BMEP	Brake Mean Effective Pressure
CG	Center of Gravity
CS	Coordinate System
CT	Combustion trace
CKI	Combustion Knocking Index
CNI	Combustion Noise Index
DFT	Discrete Fourier Transform
DoE	Design of Experiment
DOF	Degree of Freedom
ECU	Engine Control Unit
EGR	Exhaust Gas Recirculation
EHP	End of High Pressure
EKF	Energy Correction Factor
FFT	Fast Fourier Transform
FIR	Finite Impulse Response
FMEP	Friction Mean Effective Pressure
IMEP	Indicated Mean Effective Pressure
IT	Injection trace
MBD	Multi Body Dynamics
NVH	Noise Vibration Harshness
ROHR	Rate of Heat Release
SBN	Structure Borne Noise
SHP	Start of High Pressure
SOC	Start of Combustion
SOI	Start of Injection
TDC	Top Dead Center
WBT	Wave Based Technique

1 Introduction

As statutory regulations for emissions and noise are getting tighter, it is essential for automobile and engine manufacturers to verify the prototypes still in the design phase of the project. Also, customers with their increasing demands on noise vibration and harshness (NVH) and cabin noise are placing their claims to the manufacturers. Thus, the demands on the capability of software packages are increasing with growing industry needs.
Over the last few years, AVL had a strong focus on combustion noise, especially at diesel engines. In internal R&D projects, two objective parameters for combustion noise where developed for testbed application. Those are the Combustion Noise Index (CNI) based on the measured cylinder pressure trace, and the Combustion Knocking Index (CKI) based on the measured sound pressure level on defined microphone positions around the running engine on a testbed. The target of those indices is a complete NVH assessment. This enables target setting, benchmarking and internal combustion development.
As development cycles are getting shorter over the time, it is necessary to detect potential problems still in the design phase of the project. In that way cost and money can be saved. Topic of the present work is the development of a purely simulation-based methodology for combustion noise assessment. This enables a fast way for manufactures to evaluate different concepts to optimize on a specific problem. Through this methodology, key performance indicators (KPI's) are introduced to evaluate trends as well as quantify trade-off relationships for target setting in NVH analysis.

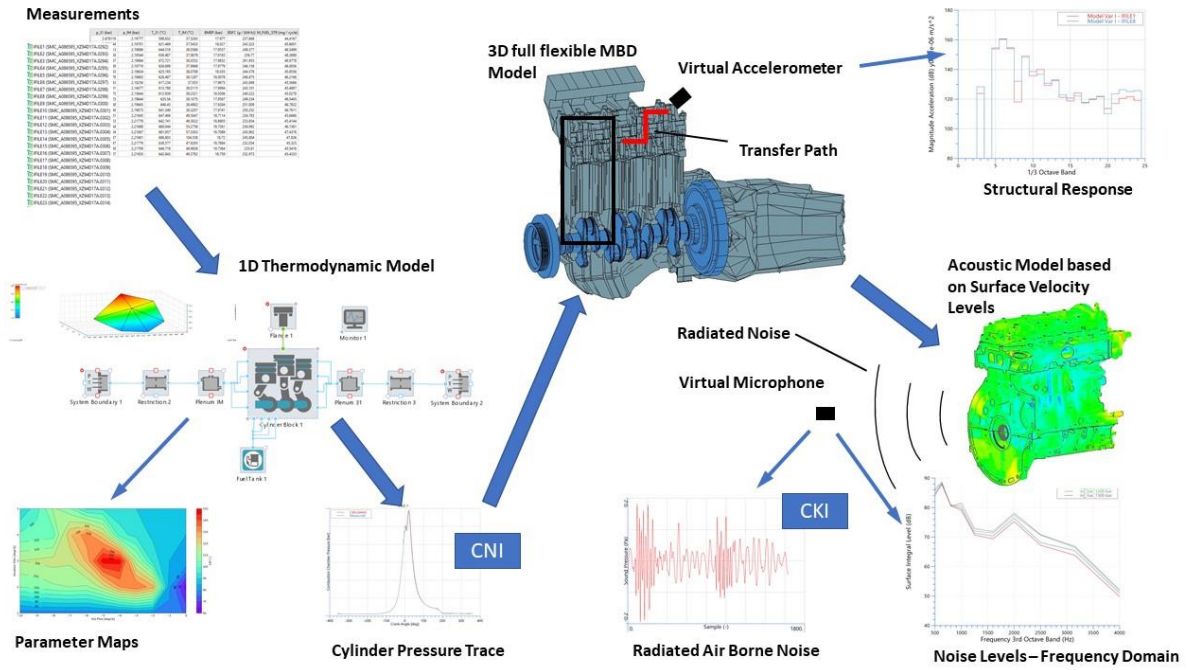

Figure 1: Combustion noise assessment - workflow

This is achieved by the development of a combustion noise assessment workflow, illustrated in Figure 1. The workflow itself subdivides thereby in three independent simulation models.

The first model, which is developed in chapter 11, includes a 1D thermodynamic combustion model that is calibrated with testbed measurement data. The model itself is resolved in crank-angle domain and consists out of the engine block including the combustion chambers, valves and intake- and outtake ports. The airpath at the intake section as well as the outlet section is neglected due to the availability of measurements directly at the ports. Through the calibration step it is ensured to achieve a highly predictive model in terms of combustion and cylinder pressure trace. Based on the resulting cylinder pressure traces CNI is introduced to quantify the harshness of the combustion during combustion simulation. Additionally, a trade-off analysis is performed to determine parameters relevant for combustions featuring high noise.
The second model, introduced in chapter 12.1, is a full flexible 3D multi body dynamic (MBD) model which uses previous simulated cylinder pressure data as input for simulation, and is resolved in time domain. It consists out of dynamic reduced (condensed) finite element model (FEM) bodies for power unit, crankshaft, conrods and pistons. The model is first investigated on different load application types for the cylinder pressure. Thereby, three different variations are introduced and analysed in terms of resulting structural vibrations. Excitations resulting from combustion variation and transferred through the structure are then evaluated on distinct nodes of the power unit regarding to vibrations. This allows an assessment of different injection strategies influencing structural vibrations on external engine parts.
In the third and last section, finally an acoustic model is set up which transforms the results generated by the MBD model in step two to radiated noise. The acoustic model, introduced in chapter 12.3, is resolved in frequency domain and includes the power unit as an uncondensed FEM body. Generated nodal results are therefore transformed from the condensed body used in the MBD analysis to the uncondensed body used in the acoustic simulation through a data recovery step. Originating from those results, in this case normal velocity levels of the engine surface, the radiated noise is calculated in the free field. Additional to the evaluation of radiated noise in frequency domain, the results are then transformed into time domain and used as an input for the calculation of the CKI.

2 Fundamentals of Diesel Combustion

In modern diesel engine development main objectives are fuel economy, low emissions and noise vibrations and harshness (NVH). These options can be achieved by various control strategies in the engine itself, as well as in their peripheral aggregates, like e.g. turbo charger and exhaust gas recirculation (EGR). Those main development targets are highly influenced by the combustion control parameters but have commonly a trade-off relationship. Thus, the optimization of combustion control parameters is a top-level priority for engine development. The internal combustion of diesel engines can be classified in various stages. First the fuel is injected into the combustion chamber by a high-pressure injection system (common-rail system), usually around the end of the combustion stroke before top dead center (TDC). Presently, the pressure in the injection system can be raised over 2000 bar. After injection the fuel gets vaporized by the high temperatures and mixed up with the hot air inside the cylinder. When the chemical reaction conditions (e.g. gas temperature, mixture conditions) are fulfilled, the combustion starts. During the combustion process, heat energy is released at a certain rate. This is commonly called rate of heat release (ROHR) [1].

2.1 Injection and Its Main Control Parameters

Through the variation of injection timing different aspects of the combustion itself as well as the formation of emission components can be controlled. The variation of the start of injection (SOI) for one single injection (main injection) for example, results in a quite different combustion. For an advanced injection the ignition delay is increased, and so is the mixing of air and fuel. Through this mechanism a large amount of fuel burns in the premixed combustion phase, leading to a steeper pressure gradient, as well as greater peak pressure and temperature. This leads on the one hand to a noisier combustion, but on the other hand to an effective reduction of NOx and soot emissions due to a faster reaction time triggered through higher pressure and temperature levels in the cylinder. With a shift of SOI to later injection timings for example, the amount of fuel which is burned in the premixed combustion phase is reduced, which leads to a smoother pressure raise and a quieter combustion. As combustion noise is linked with the sudden rise of cylinder pressure after the ignition of the air/fuel mixture, pilot injections reduce the abrupt increase of cylinder pressure, therefore the overall combustion noise can be lowered. Though this additional injection does not completely contribute to the work delivered by the piston, because pilot injections are commonly injected early and start burning before the piston reaches TDC. Another important engine parameter is given by the rail pressure of the injection system. Thereby, higher pressures are leading to a finer atomization of the of the fuel which leads to an enhanced mixing between fuel and air. Thus, the premixed combustion phase is again stronger, leading to a noisier combustion [1] [2] [3].

2.2 Combustion and ROHR

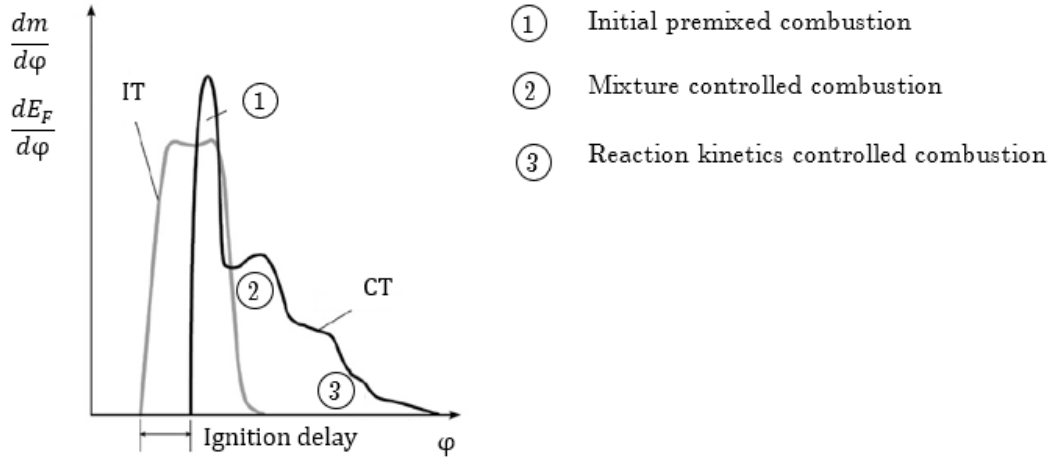

Figure 2: Injection and combustion trace of a diesel engine [4]

The period during SOI and start of combustion (SOC) refers as ignition delay. The physical key processes during the ignition delay are the atomization of the fuel, the vaporisation and mixing of the fuel as well as the forming of a flammable mixture.

Phase 1: Initial premixed combustion

This first phase follows directly after the ignition. A nearly homogenous mixture is formed by the during the ignition delay injected fuel. After the ignition delay, which is physically and chemically well controlled, the mixture burns very quickly. The ROHR is controlled by the velocity of the chemical reactions and the quantity of the injected fuel mass in this combustion phase. The typical combustion noise of the diesel engine (diesel knocking) is formed through high pressure gradient in this phase. As mentioned before, the rate of pressure raise can be manipulated by a shift of SOI. Whereby: the more early the injection takes place, the "rougher" or more impulsive the combustion gets. Thus, a later injection leads to a later and more "smooth" combustion. As mentioned before, for early injections the ignition delay is longer due to lower temperature and pressure levels. Therefore, the amount of fuel that burns in the premixed combustion phase is higher. For later injection timings the conditions are turning. The amount of fuel that burns in the premixed combustion phase is smaller due to a shorter ignition delay, the resulting pressure gradient is flatter. A further shift of SOI leads to a longer ignition delay because of lower temperatures inside the combustion chamber. The combustion noise gets louder again, refer to Figure 3.

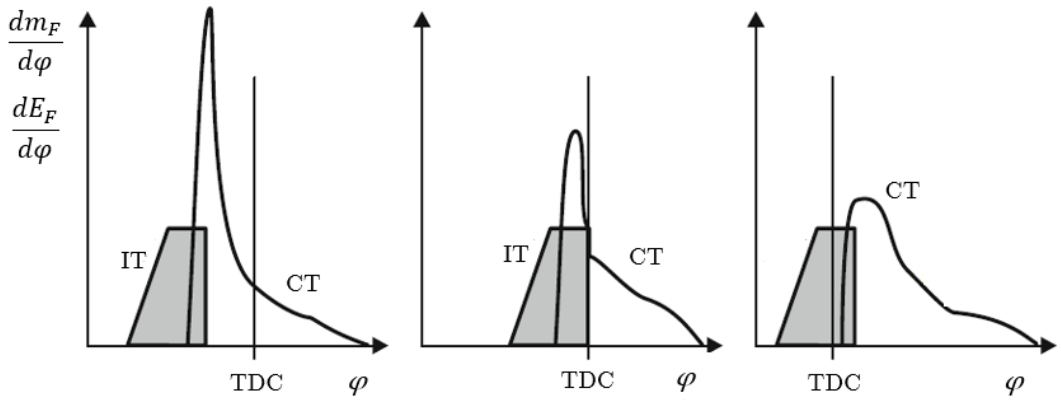

Figure 3: Injection and combustion trace for early (left) and late (right) combustion [4]

Through the introduction of multiply pre-injections, the combustions noise can be lowered significantly. Thereby a small amount of fuel is injected inside the combustion chamber before the main injection. After the ignition delay this leads to a minor ROHR and a low pressure raise. The through the pressure raise increased temperature, as well as the clash of the section of higher temperature induced by the pre-injection with the mixture of the main injection leads to a drastically decrease of the injection delay of the main injection. This leads to a clear reduction of the ratio of premixed combustion which has a positive impact on combustion noise.

Phase 2: Main combustion

In the second phase of the combustion, the ROHR is controlled by turbulent mixing procedures between injected fuel and air. Thus, this phase is also known as mixing-controlled phase. In this phase injection, spray disintegration, drop vaporization, mixing with air, combustion and pollutant formation takes place simultaneously.

Phase 3: Post-combustion

After the completion of the injection, the flame develops to a zone of partial oxidized products of the rich premixed combustion, which is surrounded by a diffusion flame. No further momentum is added through the injection spray. A fast closing of the injectors nozzle needle results in a high velocity of the last fuel packages. Thus, they have a similar combustion process as the main combustion. A slow closing of the nozzle needle leads to a low velocity of the last fuel packages and hence a poorer mixing with air. As a result, the oxidation process is slower, and the soot formation is higher. The temperature inside the combustion chamber lowers again through the expansion of the piston in the direction of bottom dead center (BDC). With lower temperatures the reaction rates are also lowered, thus the combustion is again chemical controlled. In this phase about 90% of the previous formed soot gets oxidized and removed.

The thermal energy released during this process is crucial for the thermodynamic quality of the overall process. This thermic energy leads to a heat up of the fuel air mixture inside the cylinder and thereby to a raise of temperature and pressure.

In the simulation of engine processes the calculation of the heat release is a key element. Whereby one must distinguish between simple empirical functions, phenomenological models or detailed physical and chemical models [4]. For this thesis a model based on a physical approach is used.

3 0D-Simulation of Diesel Combustion

In the scope of the following chapter the theory for a 0D-combustion model combined with a physical based injector model is introduced. At this point it is just mentioned that there are different approaches for combustion modelling such as quasi-dimensional, one-, or multidimensional models. Whereby those models can rely on a physical or phenomenological approach.

Phenomenological models describing phenomena through empirical or half-empirical functions of relevant parameters. Those models are generally simple build up and easy to use. Usually they need specific parameters which are generated through appropriate experiments.

Physical models are based on mathematical expressions of fundamental physical laws, e.g. conservation laws for mass, energy and momentum [5].

For 0D-combustion modelling a local variability of the quantities is not considered. Thus, they are only varying in time. The fundamental equations for the calculation of the combustion chamber are based on the first law of thermodynamics. The advantage of those models is the ability to deliver fast results. They also enable a thermodynamic correct assessment of the engine process, without the need to cover the spatial flow field inside the combustion chamber, nor to cover local phenomena. Is the combustion chamber considered with only one zone with locally constant substance properties, it is called a one zone model. In two zone models the combustion chamber gets divided in two zones, without performing a spatial assignment. Mostly a differentiation is done between one zone which contains the burned, as well as one zone which contains the unburned load. In analogy a separation of the combustion chamber in more zones is possible.

3.1 Fundamental Equations

The combustion chamber represents a transient open system (Figure 4), in which all quantities have a strong fluctuation in space and time.

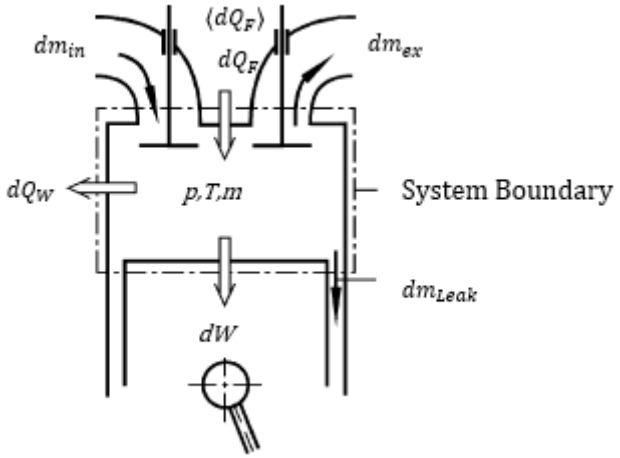

Figure 4: System combustion chamber [4]

During every work cycle a sequence of complex processes is running, which can be categorised as follows:

Mass transport: through the system boundaries the incoming gas mass dm_{in} as well as the outgoing gas mass dm_{ex}, the leakage dm_{leak} and for air aspirated engines the fuel mass dm_F is transported.
Energy transport: during the combustion of the fuel the chemical process releases heat dQ_F; through the working gas heat dQ_W and work dW is transferred through the system boundaries; all mass flows contribute with their enthalpy and external energy to the energy transport.
Change of the inner energy dU stored in the system.

For the calculation of that system usually the fundamental equations for mass, energy and momentum as well as the thermodynamic equation of state are provided. Usually following assumptions are made for a 0D thermodynamic modelling of the system combustion chamber:

- The system combustion chamber gets subdivided into different zones, each zone is thereby considered as homogenous. Thus, each quantity within one zone can be reduced to a time- respectively crank angle – dependency. Local distinctions are thereby not considered.
- The working gas is a mixture of ideal gases, whose components air, burned gas and fuel vapour are perfectly mixed at any given time.
- Friction within the working gas is not considered.
- The system boundaries are set, that the external energies have not to be considered.
- In the energy conservation the combustion is considered through an additional fuel heat dQ_F, which is equal to the chemical energy of the reacting fuel.

Conservation of mass: The general continuity law $\dot{m} = \sum_i \dot{m}_i$ states, that the change of the mass m in the control volume is equal to the sum of the on- and off-flowing mass fluxes. With reference to the crank angle φ the conservation law of mass for the system combustion chamber in differential form for air aspirated (3-2) or mixture aspirated (3-1) engines equals as follows:

$$\frac{dm}{d\varphi} = \frac{dm_{in}}{d\varphi} - \frac{dm_{ex}}{d\varphi} - \frac{dm_{Leak}}{d\varphi} \qquad 3\text{-}1$$

$$\frac{dm}{d\varphi} = \frac{dm_{in}}{d\varphi} - \frac{dm_{ex}}{d\varphi} - \frac{dm_{Leak}}{d\varphi} + \frac{dm_F}{d\varphi} \qquad 3\text{-}2$$

The change of the working gas m in the combustion chamber follows mostly through the inflowing mass m_{in} and outflowing mass m_{ex} during the load change. Over the course of the high compression phase the gas mass changes through the leakage mass m_{Leak} which is mainly lost through the piston rings as blow by gas.

Conservation of energy: The first law of thermodynamics, for open transient systems, under consideration of the above stated assumptions as a derivation by the crank angle φ is given by following equation (3-3):

$$-\frac{pdV}{d\varphi}+\frac{dQ_F}{d\varphi}-\frac{dQ_W}{d\varphi}+h_{in}\frac{dm_{in}}{d\varphi}-h_{ex}\frac{dm_{ex}}{d\varphi}-h_{ex}\frac{dm_{Leak}}{d\varphi}=\frac{dU}{d\varphi} \quad 3\text{-}3$$

The first term on the left-hand side $pdV/d\varphi$ stands for the delivered work in form of volume change work, which is a product of the current cylinder pressure and the change of the cylinder volume. The next two terms constitute the so-called heat release. It consists of a free fuel heat, the fuel trace $dQ_F/d\varphi$ as well as the discharged wall heat $dQ_W/d\varphi$. The following three terms represent the enthalpy flux from inflowing and outflowing mass as well as leakage. On the right side of the equation is the change of the inner energy inside of the combustion chamber $dU/d\varphi$ located.

Equation of state: In accordance to the previous assumptions, for the working gas in the combustion chamber the equation for ideal gases applies (3-4):

$$pV = mRT \quad 3\text{-}4$$

The derivation of equation (3-4) after the crank angle delivers:

$$p\frac{dV}{d\varphi}+V\frac{dp}{d\varphi}=mR\frac{dT}{d\varphi}+mT\frac{dR}{d\varphi}+RT\frac{dm}{d\varphi} \quad 3\text{-}5$$

Categorical those equations are available for the calculation of the system combustion chamber. Through appropriate assumptions during the modelling it should be attempted to express the terms of those three equations by a preferably small number of unknowns. Additionally, it is to consider, that for an explicit solution for each differential equation a initial condition is necessary. However, for a certain crank angle all values must be known. For one zone models, following unknows must be taken under consideration: The state of the working gas – defined through the traces of Temperature T and pressure p, - the current composition of the working gas, as well as the released fuel heat dQ_F. However, the most important initial condition of the engine cycle simulation is the mass of the working gas m, which condition and composition is to be stated mostly at the end of intake closing. If one of those four variables is known, it is possible to calculate on the basis of substance polynomials, by which a determination of the inner energy U, as well as the ideal gas constant R in relation of pressure p, temperature T and load composition the remaining three variables. The analysis of losses of the real engine process cycle shows the strengths and weaknesses of the engine, as well as the potential for improvements. For the simulation itself a burning trace has to be specified. This is done through a substitution burning trace or by a combustion simulation. The traces for pressure, temperature and composition of the load inside the combustion chamber are following out of this. Statements over the expected induced work, the fuel consumption or the losses are possible. The influence of different engine parameters can be investigated.

Materiel properties

For the solution of above stated equations, the material properties of the gas mixture inside the combustion chamber are necessary. For a determination of the material properties of the gas mixture, it is necessary to determine the material properties of the individual species inside the combustion chamber first. If they are known, the material properties of the gas mixture can be

determined through the composition of the individual species. For the calculation of the substance values of individual species, usually a polynomial approach is used. Here are examples with the 7-coefficient-polynomial-approach by NASA stated. Those apply for ideal gases. Thus, they are only depended from the temperature T. For the calculation the molar gas constant R_m is also needed.

Molar heat capacity at constant pressure:

$$\frac{c_p^0}{R_m} = a_1 + a_2 T + a_3 T^2 + a_4 T^3 + a_5 T^4 \tag{3-6}$$

Molar technical enthalpy:

$$\frac{H_T^0}{R_m T} = a_1 + \frac{a_2 T}{2} + \frac{a_3 T^2}{3} + \frac{a_4 T^3}{4} + \frac{a_5 T^4}{5} + \frac{a_6}{T} \tag{3-7}$$

Molar free enthalpy:

$$\frac{G_T^0}{R_m T} = a_1(1 - ln\, T) - \frac{a_2 T}{2} - \frac{a_3 T^2}{6} - \frac{a_4 T^3}{12} - \frac{a_5 T^4}{20} + \frac{a_6}{T} - a_7 \tag{3-8}$$

The coefficients for the stated polynomials are available at different sources. With these polynomials and with the molar mass M_i of the different species, it is possible to determine the specific heat capacities, the specific enthalpies as well as the free enthalpies. As an example, the calculation of the specific enthalpy for an arbitrary species i is done:

$$h_i = \frac{H_{T_i}^0}{M_i} \tag{3-9}$$

To determine the specific enthalpy h of the whole load, it is necessary to know the composition of the load through mass ratios μ_i besides the enthalpies of the individual species h_i:

$$h = \sum_i h_i \mu_i \tag{3-10}$$

For the remaining substance values the approach is the same.
With the specific heat capacity at constant pressure c_p and the specific gas constant R it is possible to determine the specific heat capacity at a constant volume:

$$c_v = c_p - R \tag{3-11}$$

With the pressure-volume work pv and the specific enthalpy h it is possible to calculate the specific inner energy u of the load. Over the ideal gas equation, the pressure-volume work can be written as RT. Here it is necessary to use the specific gas constant of the whole load.

$$\bar{u} = h - pv = h - RT \tag{3-12}$$

The above stated inner energy $\bar{u}$ consists out of a chemical bound energy as well as a thermal inner energy. If the chemical energy is stated through the calorific value or rather the heat trace, the inner energy must only consist out of the thermal energy [4].

3.2 Injection and High-Pressure Rail Model

The model used represents a common-rail injection model which calculates the fuel trace over a crank-angle basis. The basic components of the model are illustrated in Figure 5.

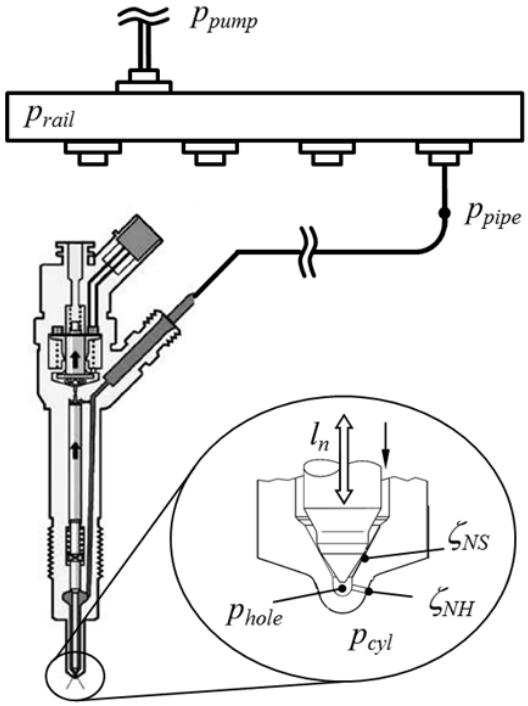

Figure 5: Illustration of the injection system: rail, pipe and injector with pressure positions [6]

Whereby the rail itself is modelled as a 0D-plenum. The injector flow gets calculated over the Bernoulli principle by modelling the nozzle flow and the needle seat throttling by two combined restrictions. The dynamics of the needle lift are represented by a force balance applied to the system. The injection signal, which comes as an input from the user, controls the opening and closing of the injector needle. Details to the individual models are stated in the following sections. Theory as well as equations for the injection and high-pressure rail model of the following chapters can be found in [6].

3.2.1 Rail

The compressibility of the working fluid is considered as a 0D-plenum. Whereby the pressure at isothermal flow is calculated by the continuity equation. The bulk modulus K for the working fluid (Diesel) gets determined out of the Cruise™ M fuel property database. Here, a value of $1.39 \cdot 10^9$ Pa can be taken as a reference. The rail pressure gets calculated according to the following equation:

$$\frac{dp_{rail}}{dt} = \frac{K}{V_{rail}} \cdot \frac{1}{\rho_{rail}} \cdot \left(\frac{dm_{pump}}{dt} + \frac{dm_{inj}}{dt} \right) \quad 3\text{-}13$$

The fuel delivered to the rail in common rail injection systems by the high-pressure pump, is stated by the fuel flow dm_{Pump}. Usually the pressure in the rail is controlled by an overpressure valve. This circumstance would lead to combined high frequency MBD model and a coupled flow problem. Thus, in the present model a simplified approach is used, where the high-pressure pump as well as the overpressure valve is substituted by an orifice with a constant diameter. The outer boundary condition of the orifice is defined equal by the user input and represents the pump pressure p_{Pump} (e.g. ECU target value). The outflow dm_{inj} from the rail to the injector is outlined in the section of the injector model.

3.2.2 Injector

The calculation of the injection rate from the nozzle hole area and the injection velocity is a commonly used approach. Thereby the velocity gets calculated from the Bernoulli equation for viscous flows. The obtained equation involves the fuel density and the discharge coefficient c_D. The friction losses in the entire injection system, from the pipe pressure measurement position over the injection pipe and injector flow and the injector nozzle hole, is represented by the discharge coefficient. The characteristic of the discharge coefficient must be measured on an injector test rig as a function from the needle lift. The incompressible flow through the orifice follows as:

$$\frac{dm_{inj}}{dt} = A_{NH} \cdot c_D \cdot \sqrt{2 \cdot \rho_{fuel} \cdot \left(p_{pipe} - p_{cyl} \right)} \quad 3\text{-}14$$

For this model an alternative approach is applied. The friction losses through the injector are here represented by two flow restrictions. At first the injector nozzle hole with the flow coefficient ζ_{NH}. It separates the cylinder from the injector blind hole. At second the restriction between the pipe pressure measurement and the blind hole, which includes also the needle seat gap, with the flow coefficient ζ_{NS}. A constant flow coefficient is assumed for both restrictions. The area of the needle seat flow is a function of the injectors needle lift. This approach has a more realistic representation of the system, because it separates the different effects in the needle seat and nozzle hole. This approach makes it also possible to parameterize the losses separately. In Figure 6 the system is shown schematically.

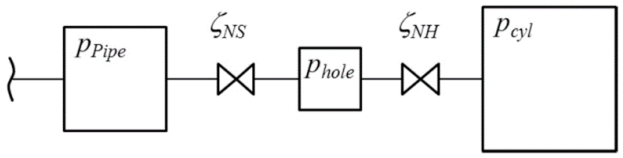

Figure 6: Schematic model of the injector flow determination [6]

Thereby, the Bernoulli principle is for both restrictions applied. In the injector itself an incompressible flow can be assumed. This allows to equalize the mass flow in the needle seat and in the nozzle hole. Now the blind hole pressure can be eliminated algebraically. Thus, the mass flow in the injector can be calculated from the pressure difference between the pipe and the cylinder, which is stated in equation 3-15.

$$\frac{dm_{inj}}{dt} = \sqrt{2 \cdot \rho_{fuel} \cdot \left(p_{pipe} - p_{cyl}\right) \cdot \frac{1}{\left(\frac{\zeta_{NS}}{A_{NS}{}^2} + \frac{\zeta_{NH}}{A_{NH}{}^2}\right)}} \qquad 3\text{-}15$$

For a specific injector system, the flow coefficients ζ_{NS} and ζ_{NH} need to be specified. It can be assumed that the needle throttling is negligible at a fully opened needle position. The flow coefficient ζ_{NH} can be estimated at a fully opened needle position by the steady state nozzle flow. This is usually done by the injector manufacturer. At this point it is highlighted that the effective pressure used in equation 3-15 is not equal to the total pressure in the common rail. However, it is equal to the corrected pipe pressure p_{pipe}. The determination of the corrected pipe pressure p_{pipe} is topic of the following sections.

With equation 3-15 it is possible to calculate the injector flow as a function of the needle lift. To find good correlation with measurements, this curve can be compared with measurement data to find good correlation values for ζ_{NS}. It is also possible to adapt the curve qualitatively to the curve of an already known injector of a similar type. It is already stated, e.g. in [7] and [8], that similar injectors have similar injections characteristics versus needle lift. The rate of the injection profile can be calculated with the above stated equation 3-15, when the needle lift and pipe pressure are measured on a testbed. In the simulation model the needle lift l_n needs to be calculated. This is done by the input of an injector signal. This signal contains out of an injection start, as well as an injection duration. Thus, the needle opens when the virtual current is on, and closes when no current is available at the injector.

The velocity of the needle during opening and closing is almost constant. This circumstance can be seen from the measurements. Whereby the velocity itself is proportional to the pipe pressure. This behaviour is quite obvious, when one thinks about the circumstance that the needle opening, and closing is actuated by the fluid pressure in the rail itself. This phenomenological connection is applied in the model by solving the differential equation 3-16 for the needle lift.

$$\frac{dl_n}{dt} = \begin{cases} +C_{accel} \cdot p_{pipe} \cdot F_{open}\big|_{signalOn} \\ -C_{accel} \cdot p_{pipe} \cdot F_{close}\big|_{signalOff} \end{cases} \qquad 3\text{-}16$$

F_{open} as well as F_{close} are constant values, since the opening and closing velocities are constant for a given injector. As stated before, this circumstance can be seen from the needle lift measurements. Generally, F_{open} and F_{close} have to be specified by measurements for a given injector. C_{accel} is a normalized needle acceleration parameter which functions as an input by the user to the model. Also, from measurement data it is evident, that there is a certain delay between the injector current signal and the beginning of the needle lift opening. This behaviour is due to the inertia of the whole system. By a constant delay time t_{open}, which is a characteristic value for the injection system and therefore a user input, this behaviour can be approximated quite well.

3.2.3 Pressure Pulsation

Pressure pulsations are omnipresent to the injection system due to the inertia and the compressibility of the working fluid. Especially for multiple injections, the pressure oscillations have a special relevance. Therefore, the quantity of the later injections depends on whether it hits a maximum or a minimum of an oscillating pressure wave. To achieve a detailed approach of the problem, a spatial discretisation of the injector system would be necessary. Here, the compressible fluid in the pipe can be seen as a spring-mass-damper system. For this simplified approach, it can be assumed that the length of the overall system is much greater than its diameter. Thus, we can equalize $dV/V = dl/l$. Therefore, the eigenfrequency of the pressure pulsations is approximated through the analogy of a mechanical spring-mass-system 3-17.

$$f_E = \frac{1}{2 \cdot \pi} \cdot \sqrt{\frac{c}{m}} = \frac{1}{2 \cdot \pi} \cdot \sqrt{\frac{K}{{l_{pipe}}^2 \cdot \rho_{fuel}}} \qquad 3\text{-}17$$

The only required input for the above stated equation, to determine the eigenfrequency is the length of the pipe l_{pipe}. The pipe length can be directly estimated by equation 3-17, if the measured pipe pressure curves are available and thus, the oscillations of the pressure is known. As a reference, for the bulk modulus a value of $1.39 \cdot 10^9$ Pa can be taken. The amplitudes of the oscillations correlate to the volume of the rail.
For the boundary between the rail and the pipe, an additional differential equation is solved in the simulation for the pipe pressure p_{pipe}. This pipe pressure is overlapped to the rail pressure. Though, it does not have a direct physical impact on the rail pressure. Thus, it works as a 'virtual' pressure to mimic the pipe pressure oscillations. For multi-cylinder arrangements there is no direct interaction between the pipe oscillations of the different injectors. In the measurements the pressure amplitude decreases due to frictions losses in the pipe which are damping the oscillation. In the model this effect is considered through an additional damping term. The quantity of the damping can be adjusted by the normalized damping constant C_{damp} [6].

3.3 Spray Model and ROHR Calculation

The combustion model used was developed by AVL in cooperation with the university of Ljubljana. It predicts the ROHR in direct injection Diesel engines as a function of the injection rate and in cylinder conditions. Multiple injections are enabled by this approach. The basis of the model is

formed through a mechanically based spray with a calculated air/fuel distribution in the spray based on a momentum conservation by applying first principles [9]. Further details and basic equations to the AVL SEW combustion model are outlined in the following sections. Theory as well as equations to spray model and combustion model are referenced to following publication: [10] and [6].

3.3.1 Spray Model

Inside the model, the mixing of air (in cylinder charge) and fuel is predicted by the spray model. Thus, it delivers the amounts of fuel contained by the spray within selected lambda limits. The amounts obtained by the spray model are furthermore the input to the combustion model which predicts the rate of heat release. The model itself is based on non-evaporating and non-reacting assumptions, as well as a spatially constant spray density.

Radial Distribution

According to [11] it is possible to assume for the velocity profile and the fuel concentration inside the spray a Gaussian radial distribution. Through these assumptions, the velocity profile and the radial fuel distribution are similar and can be stated as follows in equation 3-18.

$$\frac{u(x,\bar{r})}{u_{cl}(x)} = \frac{\phi(x,\bar{r})}{\phi_{cl}(x)} = e^{-k_m \cdot \left(\frac{\bar{r}}{\bar{R}}\right)^2} \qquad 3\text{-}18$$

Thereby, u is the velocity, ϕ is the mass fraction of the injected fuel, $\bar{r}$ is the radial distance from the center line of the spray (cl), $\bar{R} = x \cdot tan(\vartheta/2)$, x is equal to the distance from the nozzle and ϑ is the spray cone angle. The location where the velocity is equal to the velocity of 1% of the velocity at the axis is the point where the spray angle is defined. Furthermore, the model constant k_m can be derived directly out of the spray angle ϑ.

Axial Distribution

The basis of the spray model is the convection driven momentum equation, where diffusion, surface and volume sources are not directly modelled. Those former two effects are taken into account by the Gaussian velocity and the distribution of the fuel concentration 3-18. Thus, the momentum flux $\dot{M}$ as well as the mass flow of the fuel $\dot{m}_f$ are conserved along the centerline of the spray. The momentum flux can be stated as

$$\dot{M} = \int_0^{A(\bar{R})} \rho \cdot u^2 \cdot dA \qquad 3\text{-}19$$

which can be written with equation 3-18 to:

$$\dot{M} = \frac{\pi}{2 \cdot k_m} \cdot \rho \cdot x^2 \cdot \tan^2\left(\frac{\vartheta}{2}\right) \cdot u_{cl}^2(x) \cdot (1 - e^{-2 \cdot k_m}) \qquad 3\text{-}20$$

Due to the reason that the term $e^{-2 \cdot k_m}$ is a very small number, it can be neglected. Hence, equation 3-20 can be written as follows:

$$u_{cl}(x) = \sqrt{\frac{2 \cdot k_m \cdot \dot{M}}{\pi \cdot \rho}} \cdot \frac{1}{x \cdot \tan\left(\frac{\vartheta}{2}\right)} \tag{3-21}$$

According to above stated relationships, the fuel concentration along the centerline can be derived from the conservation of the fuel mass

$$\dot{m}_f = \int_0^{A(\bar{R})} \rho \cdot u \cdot \phi \cdot dA \tag{3-22}$$

as

$$\phi_{cl}(x) = \sqrt{\frac{2 \cdot k_m}{\pi \cdot \rho \cdot \dot{M}}} \cdot \dot{m}_f \cdot \frac{1}{x \cdot \tan\left(\frac{\vartheta}{2}\right)} \tag{3-23}$$

Spray Propagation

Through the assumption that there is only a momentum in flux by the fuel injected from the nozzle, the spray model can be derived, yielding

$$\frac{\partial}{\partial t} \int_{CV} \rho \cdot u \cdot dV = \rho_{f,l} \cdot u_0^2 \cdot A_0 = \dot{M} \tag{3-24}$$

where ρ is the local density in the evanescent volume dV. CV corresponds to the overall spray volume, $\rho_{f,l}$ is the density of the working fluid, u_0 is the velocity at the nozzle exit of the fuel, A_0 is the cross-sectional area of the nozzle and $\dot{M}$ is the momentum flux of the working fluid through the nozzle. Supposing a conservation of spray momentum in time, the overall momentum in the spray equals the integrated momentum flux through the nozzle at any given time instant t. This is stated by equation 3-25 which can be obtained by equation 3-21 through an integration in time.

$$\int_{CV} \rho \cdot u \cdot dV = 2 \cdot \pi \cdot \int_{l_1}^{l_{tip}} \int_0^{\bar{R}} \rho \cdot u \cdot \bar{r} \cdot d\bar{r} \cdot dx = \int_0^{\tau} \dot{M} \cdot dt = M \tag{3-25}$$

where l_{tip} is the penetration at the spray tip and l_1 is the penetration at the origin. As main input to the spray model functions the injection rate, which is calculated by the rail and injector model presented in section 3.2 Injection and High-Pressure Rail Model.
The spray tip penetration equation 3-26 can be received by combining equation 3-18, equation 3-21 and equation 3-25:

$$l_{tip} = \sqrt{l_1^2 + \frac{M}{\sqrt{\frac{\pi \cdot \rho \cdot \dot{M}}{2 \cdot k_m}} \cdot \tan\left(\frac{\vartheta}{2}\right) \cdot (1 - e^{-k_m})}}} \quad 3\text{-}26$$

Thus, equation 3-26 links the spray characteristics and the momentum flux to a spray tip propagation for a particular position of the spray origin.
The position of the nozzle exit corresponds to the spray origin l_1 during the injection. The model features also an approach where the spray continues spreading even after the injection has ended. This circumstance is not only applicable to l_{tip}, but also to l_1. Thereby it is assumed that the CG of the spray continues to propagate with a certain velocity u_{CG} after the injection has already ended.

$$u_{CG} = \frac{M}{m_{sp}} \quad 3\text{-}27$$

Whereby, M still stands for the momentum at the end of the injection. The mass of the spray can be written as:

$$m_{sp} = 2 \cdot \pi \cdot \rho \cdot \int_{l_1}^{l_{tip}} \int_0^{\bar{R}} \bar{r} \cdot d\bar{r} \cdot dx = \frac{\pi \cdot \rho}{3} \cdot \tan^2\left(\frac{\vartheta}{2}\right) \cdot \left(l_{tip}^3 - l_1^3\right) \quad 3\text{-}28$$

With the definition of the CG of the spray:

$$x_{CG} = \frac{\int_{CG} x \cdot \rho \cdot dV}{\int_{CG} \rho \cdot dV} \quad 3\text{-}29$$

Which leads to:

$$\dot{l}_1 = \frac{4}{3} \cdot \frac{u_{CG}}{\frac{4 \cdot C \cdot l_1}{l_{tip}^3 - l_1^3} - 3 \cdot \frac{2 \cdot C \cdot l_1^2 + C^2}{\left(l_{tip}^3 - l_1^3\right)^2} \cdot \left(l_{tip} \cdot l_1 - l_1^2\right)} \quad 3\text{-}30$$

Where C is expressed by:

$$C = \frac{M}{\sqrt{\frac{\pi \cdot \rho \cdot \dot{M}}{2 \cdot k_m}} \cdot \tan\left(\frac{\vartheta}{2}\right) \cdot (1 - e^{-k_m})} \quad 3\text{-}31$$

Through the combination of equation 3-26 and equation 3-31, the spray dynamics after the spray detachment from the nozzle can be modelled.

Fuel mass within Selected Lambda Limits

Through equation 3-32, the relation between the fuel mass fraction and the combustion air ratio can be stated.

$$f = \frac{1}{1 + \lambda \cdot L_{st}} \tag{3-32}$$

For a correct calculation of the fuel mass within selected lambda limits, it is important to determine the correct radius which corresponds to a certain axial distance originating from the nozzle and at a particular lambda limit. This is pictured in Figure 7. Where on the abscissa the distance from the nozzle is stated, and on the ordinate the radial distance from the spray centerline. The diagram schematically shows iso-lines for three representative lambda areas in the spray cone for a certain time instant t.

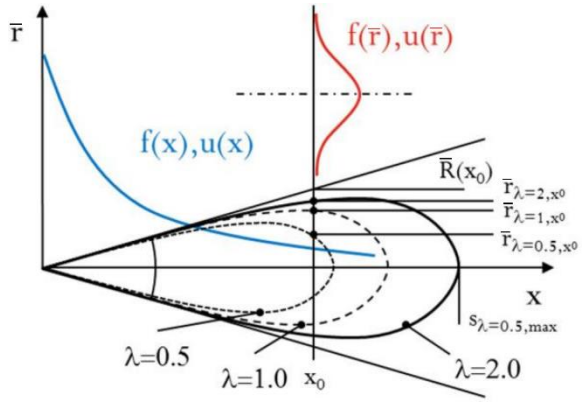

Figure 7: Illustration of the spray model [10]

For detailed information about the mathematical derivation of the formulations as well as the equation framework, it is referred to the work stated in [12] and [13]. In the following section, only the basic equations are derived.

$$\bar{r}_{\lambda,x} = \bar{R} \cdot \sqrt{\frac{\ln\left(\frac{\mathrm{x} \cdot \tan\left(\frac{\vartheta}{2}\right)}{\sqrt{\frac{2 \cdot k_m}{\pi \cdot \rho \cdot \dot{M}}} \cdot \dot{m}_f \cdot (1 + \lambda \cdot L_{st})}\right)}{-k_m}} \tag{3-33}$$

For a certain fuel mass contained in the region from the spray core ($\lambda = 0$) up to a λ_1 within a selected lambda value of λ_1 can be stated as:

$$m_{f,0<\lambda<\lambda_1} = 2 \cdot \pi \cdot \rho \cdot \int_{l_{\lambda_1,min}}^{l_{\lambda_1,max}} \int_0^{\bar{r}_{\lambda_1,x}} \phi_{cl}(x) \cdot e^{-k_m \cdot \left(\frac{\bar{r}}{\bar{R}}\right)^2} \cdot \bar{r} \cdot d\bar{r} \cdot dx \quad 3\text{-}34$$

Where according to Figure 7, $l_{\lambda_1,min}$ and $l_{\lambda_1,max}$ correspondent to the lower and upper axial distance that comply to λ_1.
Through an integration in $\bar{r}$ and x, and an algebraic manipulation of equation 3-34, the term can be written as:

$$m_{f,0<\lambda<\lambda_1} = \sqrt{\frac{\pi \cdot \rho}{2 \cdot k_m \cdot \dot{M}}} \cdot \dot{m}_f \cdot \tan\left(\frac{\vartheta}{2}\right) \cdot \left(l_{\lambda_1,max}^2 - l_{\lambda_1,min}^2\right) - \frac{\pi \cdot \rho}{3 \cdot k_m} \cdot \tan^2\left(\frac{\vartheta}{2}\right) \cdot \frac{1}{1 + \lambda_1 \cdot L_{st}} \cdot \left(l_{\lambda_1,max}^3 - l_{\lambda_1,min}^3\right) \quad 3\text{-}35$$

Thus, the fuel mass which is available between the lower lambda limit λ_1 and the upper lambda limit λ_2, where applies that $\lambda_2 > \lambda_1$, can be calculated as follows:

$$m_{f,\lambda_1<\lambda<\lambda_2} = m_{f,0<\lambda<\lambda_2} - m_{f,0<\lambda<\lambda_1} \quad 3\text{-}36$$

Equation 3-36 allows the determination of arbitrary numbers of fuel masses between arbitrary selected lambda values.
With equation 3-35 it is also possible to model the amount of fuel which has reached the combustion chamber wall at a distance $\bar{R}_W$ through first principles. This is the case if l_{tip} is larger than $\bar{R}_W$. Then $l_{\lambda_1,max}$ is replaced by $\bar{R}_W$, and equation 3-35 enables to calculate the fuel mass contained in the region from the spray core up to a λ_1 which has not yet reached the wall of the combustion chamber. Furthermore, it is directly possible to calculate the mass of the fuel that has reached the wall. Thus, the ratio of the overall fuel mass between the same lambda limits is:

$$R_{f,wall,\lambda_1<\lambda<\lambda_2} = \frac{m_{f,wall,\lambda_1<\lambda<\lambda_2}}{m_{f,\lambda_1<\lambda<\lambda_2}} \quad 3\text{-}37$$

Spray Mass within Selected Lambda Limits

For a determination of the oxygen availability in a certain lambda region, it is important to calculate the overall fuel mass as well as the charge inside a certain lambda limit. For this purpose, equation 3-28 gets integrated within the same limits as equation 3-34, which provides:

$$m_{sp,0<\lambda<\lambda_1} = 2 \cdot \pi \cdot \rho \cdot \int_{l_{\lambda_1,min}}^{l_{\lambda_1,max}} \int_0^{\bar{r}_{\lambda_1,x}} \bar{r} \cdot d\bar{r} \cdot dx \quad 3\text{-}38$$

Which leads through integration in x and $\bar{r}$ as well as algebraic reformulations to equation 3-39.

$$m_{sp,0<\lambda<\lambda_1} = -\frac{\pi \cdot \rho \cdot \tan^2\left(\frac{\vartheta}{2}\right)}{3 \cdot k_m} \cdot \left[l_{\lambda_1,max} \cdot \left(\ln\left(l_{\lambda_1,max} \cdot B\right) - \frac{1}{3} \right) - l_{\lambda_1,min} \cdot \left(\ln\left(l_{\lambda_1,min} \cdot A\right) - \frac{1}{3} \right) \right] \quad 3\text{-}39$$

Whereby the variable B stands for:

$$B = \frac{\tan\left(\frac{\vartheta}{2}\right)}{\sqrt{\frac{2 \cdot k_m}{\pi \cdot \rho \cdot \dot{M}}} \cdot \dot{m}_f \cdot (1 + \lambda_1 \cdot L_{st})} \quad 3\text{-}40$$

In analogy to $m_{f,\lambda_1<\lambda<\lambda_2}$ stated in equation 3-36, $m_{sp,\lambda_1<\lambda<\lambda_2}$ is calculated.

Spray Density

The local spray density can be stated as

$$\rho = \frac{1}{\frac{\phi}{\rho_{f,v}} + \frac{1-\phi}{\rho_{cyl}}} = \frac{\rho_{cyl}}{1 - f \cdot \left(1 - \frac{\rho_{cyl}}{\rho_{f,v}}\right)} = \frac{\rho_{cyl}}{1 - \frac{m_f}{m_{sp}} \cdot \left(1 - \frac{\rho_{cyl}}{\rho_{f,v}}\right)} \quad 3\text{-}41$$

where $\rho_{f,v}$ corresponds to the density of the fuel vapour, ρ_{cyl} is the in-cylinder charge density, m_f is the fuel mass injected and m_{sp} is determined by equation 3-28.

3.3.2 Combustion Model

At certain lambda limits, the spray is divided into different areas to determine the ROHR. As derived in the previous sections, the spray model provides the available fuel and oxygen fraction in these certain areas. On that basis, the combustion model calculates the ROHR. In the following sections the basic equations of the combustion model are derived. For a detailed information it is referred to [14].

Basic Principles of the Combustion Model

The combustion model calculates the ROHR from the different sections of a premixed and two diffusion parts at certain lambda limits.

$$\frac{dQ_{comb}}{dt} = \frac{dQ_{pre}}{dt} + \frac{dQ_{diff,\lambda_{low}<\lambda<\lambda_{hi}}}{dt} + \frac{dQ_{diff,\lambda_{hi}<\lambda<\lambda_{@\bar{R}}}}{dt} \quad 3\text{-}42$$

Where pre indicates the premixed charge, $diff, \lambda_{low} < \lambda < \lambda_{hi}$ denotes the diffusion combustion within the excess air ratio limits λ_{low} and λ_{hi} and $diff, \lambda_{hi} < \lambda < \lambda_{@\bar{R}}$ indicates the diffusion combustion within the excess air ratio limits λ_{hi} and $\lambda_{@\bar{R}}$. Furthermore, it is assumed that below λ_{low} no combustion occurs. As additional input to the combustion model, a distinction between two lambda areas as well as a possibility to treat the fuel which is adhering on the cylinder wall on a

physical basis is provided by the spray model. The terms of equation 3-42 can be interpreted as follows:

$$\frac{dQ_{pre}}{dt} = C_{pre} \cdot \lambda \cdot L_{st} \cdot \frac{m_{f,U,pre,A}^2}{V_{mix}} \cdot H_u \cdot e^{-\frac{k_A \cdot T_A}{T}} \cdot \left(t - t_{ign}\right)^2 \quad 3\text{-}43$$

$$\frac{dQ_{diff,\lambda_{low}<\lambda<\lambda_{hi}}}{dt} = C_{diff} \cdot m_{f,U,\lambda_{low}<\lambda<\lambda_{hi},A} \cdot H_u \cdot \frac{\sqrt{k_T}}{\sqrt[3]{V_{cyl}}} \cdot \left(1 - R_{f,wall,\lambda_{low}<\lambda<\lambda_{hi}} \cdot (F_{wall} - 1)\right) \quad 3\text{-}44$$

$$\frac{dQ_{diff,\lambda_{hi}<\lambda<\lambda_{@\bar{R}}}}{dt} = C_{diff} \cdot m_{f,U,\lambda_{hi}<\lambda<\lambda_{@\bar{R}},A} \cdot H_u \cdot \frac{\sqrt{k_T}}{\sqrt[3]{V_{cyl}}} \cdot \left(1 - R_{f,wall,\lambda_{hi}<\lambda<\lambda_{@\bar{R}}} \cdot (F_{wall} - 1)\right) \quad 3\text{-}45$$

where $m_{f,U,pre,A}$ addresses the available unburned fuel for premixed combustion, $m_{f,U,\lambda_{low}<\lambda<\lambda_{hi},A}$ and $m_{f,U,\lambda_{hi}<\lambda<\lambda_{@\bar{R}},A}$ are the available fuel within selected lambda limits for the diffusion combustion, C_{pre}, C_{diff}, k_A, T_A, and F_{wall} are model constants, the current time is expressed by t and t_{ign} is the ignition timing, k_T is the turbulent kinetic energy, V_{cyl} is the volume of the cylinder, $R_{f,wall,\lambda_{low}<\lambda<\lambda_{hi}}$ and $R_{f,wall,\lambda_{hi}<\lambda<\lambda_{@\bar{R}}}$ are stated by equation 3-37. The mixing volume V_{mix} is expressed by equation 3-46 as follows:

$$V_{mix} = m_{f,pre} \cdot \left(\frac{1}{\rho_{f,v}} + \frac{\lambda_{pre} \cdot L_{st}}{\rho_{cyl}}\right) \quad 3\text{-}46$$

where $\rho_{f,v}$ and ρ_{cyl} represent the density of the fuel vapor and in-cylinder charge, and λ_{pre} is the assumed lambda value for the premixed combustion.

Evaluation of the Unburned Fuel

From the spray model in the previous chapters, distribution of the fuel concentration is known. Past SOC, this fuel consists out of a fraction of burned as well as unburned fuel. Since only unburned fuel is relevant for the combustion, it is calculated according to equation 3-47.

$$m_{f,U,x} = m_{f,x} - m_{f,B,x} \quad 3\text{-}47$$

Whereby, x represents $\lambda_{low} < \lambda < \lambda_{hi}$ or $\lambda_{hi} < \lambda < \lambda_{@\bar{R}}$, $m_{f,x}$ is stated through the spray model and $m_{f,B,x}$ is calculated by the combustion model. When calculating the amount of fuel burned in a certain lambda region $m_{f,B,x}$, the transport of burned fuel between the different lambda zones must be considered. Thus, yields to

$$dm_{f,B,\lambda_{low}<\lambda<\lambda_{hi}} = \frac{1}{H_u} \cdot \frac{dQ_{diff,\lambda_{low}<\lambda<\lambda_{hi},G}}{dt} - dm_{f,B,\lambda_{low}<\lambda<\lambda_{hi}\rightarrow\lambda_{hi}<\lambda<\lambda_{@\bar{R}}} \quad 3\text{-}48$$

and

$$dm_{f,B,\lambda_{hi}<\lambda<\lambda_{@\bar{R}}} = \frac{1}{H_u} \cdot \frac{dQ_{diff,\lambda_{hi}<\lambda<\lambda_{@\bar{R}},G}}{dt} + dm_{f,B,\lambda_{low}<\lambda<\lambda_{hi}\rightarrow\lambda_{hi}<\lambda<\lambda_{@\bar{R}}} \quad 3\text{-}49$$

where

$$dm_{f,B,\lambda_{low}<\lambda<\lambda_{hi}\rightarrow\lambda_{hi}<\lambda<\lambda_{@\bar{R}}} = \frac{m_{f,\lambda_{hi}<\lambda<\lambda_{@\bar{R}},i} - m_{f,\lambda_{hi}<\lambda<\lambda_{@\bar{R}},i-1}}{dt} \cdot \frac{m_{f,B,x}}{m_{f,x}} \quad 3\text{-}50$$

stands for the transport between the different zones of the burned and unburned fuel. The indices i and $i-1$ represent the current and previous time step, which leads to a Euler like differentiation. As represented by the index G, equation 3-48 and equation 3-49 use gross terms for $\frac{dQ_{diff,\lambda_{low}<\lambda<\lambda_{hi},G}}{dt}$ and $\frac{dQ_{diff,\lambda_{hi}<\lambda<\lambda_{@\bar{R}},G}}{dt}$. In contrast to equation 3-44 and equation 3-45, the gross terms comprise the contribution of the premixed combustion. This is outlined in more detail in the following section.

Evaluation of the Fuel Available for Premixed Combustion

As outlined in the previous chapters, it is known that a certain amount of fuel burns in the premixed phase of the Diesel combustion. This amount is primary determined through the injection rate and the ignition delay period. As the spray model does not predict the available amount of fuel for the premixed combustion $m_{f,pre,A}$, because it is not a property of the spray itself, it must be determined separately. This is done by following equation.

$$m_{f,pre,A} = R_{pre} \cdot m_{f,inj}|_{@t_{ign}} \quad 3\text{-}51$$

where $m_{f,inj}|_{@t_{ign}}$ outlines the amount of fuel injected at SOC. As it is shown in experiments that the relative share of fuel which burns in the premixed combustion increases with the duration of the ignition delay. Thus, R_{pre} is set proportional to the ignition delay period.
In analogy to equation 3-47, the available fuel for the premixed combustion used in equation 3-43 can be written as

$$m_{f,U,pre,A} = m_{f,pre,A} - m_{f,B,pre} \quad 3\text{-}52$$

where $m_{f,B,pre}$ is received by the integration of equation 3-43 in time.

Evaluation of the Fuel Available for Diffusion Combustion

When determining the fuel mass for the diffusion combustion $m_{f,U,x,A}$, one has to consider that the actual available fuel mass $m_{f,U,x,A}$ can be smaller than the total fuel mass $m_{f,U,x}$ due to following reasons:

- Evaporation: is considered by the reduction factor F_{evap}
- Reduced oxygen availability is considered by the reduction factor $F_{diff,x}$

- Reduced fuel availability due to premixed combustion: the amount taken from the same fuel spray is being considered by the reduction factor F_{pre}

In the following equations the individual terms are stated.

$$m_{f,U,x,A} = F_{evap} \cdot F_{diff,x} \cdot F_{pre} \cdot m_{f,U,x} \tag{3-53}$$

Whereby, F_{evap} is determined from the evaporated fuel mass and the injected fuel mass as a ratio by

$$F_{evap} = 1 - \frac{m_{f,unevap}}{m_{f,inj}} \tag{3-54}$$

where the amount of evaporated fuel is calculated out of the unevaporated fuel $m_{f,unevap}$. The reduction factor $F_{diff,x}$ for the oxygen availability is determined as follows

$$F_{diff,x} = \frac{m_{air,x}}{L_{st} \cdot m_{f,U,x}} \tag{3-55}$$

where $m_{air,x}$ is determined through the spray and fuel mass between the selected lambda limits ($m_{sp,x}$ – equation 3-39 and $m_{f,x}$ – equation 3-36) and the in-cylinder charge composition. Thus, towards the end of combustion, the air availability gets reduced which affects the term $F_{diff,\lambda_{low}<\lambda<\lambda_{hi}}$ in particular. By F_{pre} the influence of the premixed combustion is calculated with the assumption that the amount of premixed fuel is taken from the evaporated fuel fraction which is mixed with adequate oxygen. Thus, yielding to

$$F_{pre} = 1 - \frac{m_{f,U,pre,A}}{m_{f,U,GA}} \tag{3-56}$$

where

$$m_{f,U,GA} = m_{f,U,\lambda_{hi}<\lambda<\lambda_{@\bar{R}},GA} + m_{f,U,\lambda_{low}<\lambda<\lambda_{hi},GA} = F_{evap} \cdot F_{diff,\lambda_{low}<\lambda<\lambda_{hi}} \cdot m_{f,U,\lambda_{low}<\lambda<\lambda_{hi}} + F_{evap} \cdot F_{diff,\lambda_{hi}<\lambda<\lambda_{@\bar{R}}} \cdot m_{f,U,\lambda_{hi}<\lambda<\lambda_{@\bar{R}}} \tag{3-57}$$

Also it is noted that reduction of the available mass for the combustion due to spray-wall interaction is not taken in account in previous equation, rather it is explicit covered by the term F_{wall} in equation 3-44 as well as equation 3-45.

Gross Diffusion Combustion Rates

According to the above modelled framework, the gross diffusion combustion rates used in equation 3-48 and equation 3-49 can be stated as

$$\frac{dQ_{diff,\lambda_{low}<\lambda<\lambda_{hi},G}}{dt} = \frac{dQ_{diff,\lambda_{low}<\lambda<\lambda_{hi}}}{dt} + \frac{m_{f,U,\lambda_{low}<\lambda<\lambda_{hi},GA}}{m_{f,U,GA}} \cdot \frac{dQ_{pre}}{dt} \quad 3\text{-}58$$

and

$$\frac{dQ_{diff,\lambda_{hi}<\lambda<\lambda_{@\bar{R}},G}}{dt} = \frac{dQ_{diff,\lambda_{hi}<\lambda<\lambda_{@\bar{R}}}}{dt} + \frac{m_{f,U,\lambda_{hi}<\lambda<\lambda_{@\bar{R}},GA}}{m_{f,U,GA}} \cdot \frac{dQ_{pre}}{dt} \quad 3\text{-}59$$

which is consistent to the division in equation 3-56 [10].

Ignition Delay

To consider both characteristic timescales of the chemical reaction as well as the turbulent mixing process, a combined Arrhenius and Magnussen formulation is used for the determination of the ignition delay. Thereby, the timespan needed to mix and also ignite the fuel gas mixture is given by:

$$t_{id} = t_{Arr} + t_{Mag} \quad 3\text{-}60$$

The ignition delay, consisting out of the Arrhenius reaction rate (equation 3-62) and the Magnussen reaction rate (equation 3-63), can be stated as the reciprocal values of the characteristic time respectively. From this assumption, equation 3-61 follows.

$$\frac{1}{t_{id}} = \frac{1}{\frac{1}{r_{Arr}} + \frac{1}{r_{Mag}}} \quad 3\text{-}61$$

If one of the reaction rates is a different order of magnitude, the lower rate is always the dominant one. Additional to the formulation stated in [12], the present formulation of the Arrhenius reaction rate (equation 3-62) includes also a term for the pressure dependency of the ignition delay. The volume of the mixture V_{mix} is calculated by the spray-model, while m_f is the mass of the fuel in the spray.

$$r_{Arr} = C_{Arr} \cdot \frac{m_f^2}{V_{mix}^2} \cdot \frac{1}{p} \cdot e^{-\frac{k_A \cdot T_A}{T}} \quad 3\text{-}62$$

Whereby, T is the cylinder temperature, k_A and T_A are model constants. From the Magnussen approach the turbulent reaction rate is derived by applying Taylor's approximation for the normalized dissipation rate. The square root of the turbulent kinetic energy k_T is thereby divided by a characteristic length. In this case it is calculated by the cubic root of the cylinder volume. Depending on rich or lean mixture, the reaction rate can be calculated either with fuel or oxygen, depending on the present case. In the case of Diesel combustion, the lean mixture predominates. Therefore, the concentration is expressed by the fuel density in the mixture volume m_f/V_{mix} which leads to equation 3-63 [6].

$$r_{Mag} = C_{Mag} \cdot \frac{m_f}{V_{mix}} \cdot \frac{\sqrt{k_T}}{\sqrt[3]{V_{cyl}}} \qquad 3\text{-}63$$

4 Theory of Multi Body Dynamic Systems

In the following chapter the fundamental approaches to describe a flexible multi body dynamic (MBD) model are derived. Content and equations of this chapter are related to following reference: [15]. These approaches are essential to understand the basic idea for calculating the global as well as local motions of a flexible body. These local motions again are used for determining the vibrations on the engine surface (structure borne noise - SBN) as well as the CKI-ABN (air borne noise) through the belonging surface velocity levels and the calculation of the radiated noise. Therefore, the whole assembly is broken down into different subsystems. These subsystems can be either purely rigid, which leads to a conventional MBD system, or flexible with reduced (condensed) degree of freedoms (DOF's). Whereas, the condensation can be of static, modal or mixed type, and is necessary to keep the number of DOF's of a system low to reduce calculation time. The couplings between the individual subsystems or bodies are implemented by joints which are either linear (e.g. spring - damper) or (highly) non-linear (e.g. hydrodynamic bearing).

4.1 General Vibration Equation

As outlined in the previous paragraph, the general motion of the considered bodies consists out of a global motion (e.g. circular rotation of a crankshaft) and a local vibration (e.g. bending vibrations of a crankshaft due to gas forces acting through the conrod on the body). Thus, these two motions must be considered by the mathematical model. To model local vibration components, each body is discretised by an adequate number of elements (partial masses). The elastic deformation of each uncondensed body is thereby described by a translational and rotational distortion component of each partial mass. The determination of each distortion component is thereby done by equation 4-1 and equation 4-2. Both equations are given in the absolute, global coordinate system.

$$m_i \cdot \frac{\partial^2 \boldsymbol{x}_i^{ABS}}{\partial t^2} = \boldsymbol{f}_{F,i}^{ABS} \tag{4-1}$$

$$\frac{\partial}{\partial t}\left(\boldsymbol{I}_{C,i}^{ABS} \cdot \boldsymbol{\omega}_i^{ABS}\right) = \boldsymbol{f}_{M,i}^{ABS} \tag{4-2}$$

Whereby equation 4-1 corresponds to the equation of motion and equation 4-2 corresponds to Euler's equation of angular momentum. The terms m_i and $\boldsymbol{I}_{C,i}^{ABS}$ represent the mass respectively inertia of the partial sub mass i. The global position as well as the angular velocity are represented by the vectors $\boldsymbol{x}_i^{ABS}$ and $\boldsymbol{\omega}_i^{ABS}$ with reference to the center of gravity (CG) of a partial mass. The vectors $\boldsymbol{f}_{F,i}^{ABS}$ and $\boldsymbol{f}_{M,i}^{ABS}$ contain the forces respectively moments which are acting on the partial mass. Also, the equations 4-1 and 4-2 have to be satisfied for each of the N partial masses of a body. To make the structure matrices invariant in time, they are transformed from a global coordinate system in a body fixed coordinate system. This transformation to the reference, or body coordinate system is done via equations 4-3 and 4-4.

$$\boldsymbol{a}^{ABS} = \boldsymbol{R}_{\alpha\beta\gamma} \cdot \boldsymbol{a} \tag{4-3}$$

$$\boldsymbol{A}^{ABS} = \boldsymbol{R}_{\alpha\beta\gamma} \cdot \boldsymbol{A} \cdot \boldsymbol{R}_{\alpha\beta\gamma}^{t} \tag{4-4}$$

Thereby $\boldsymbol{A}^{ABS}$ and $\boldsymbol{a}^{ABS}$ characterizes a general tensor respectively vector in the absolute, or global coordinate system. $\boldsymbol{A}$ and $\boldsymbol{a}$ denote a tensor or vector in the relative, or body coordinate system. The vector containing the relative rotations between the origin of the global (reference) and local (body) coordinate system is represented by $(\alpha, \beta, \gamma)^t$. The general transformation matrix $\boldsymbol{R}_{\alpha\beta\gamma}$ is built up by the sequential rotations α, β and γ. As outlined in equation 4-5, $\boldsymbol{R}_{\alpha\beta\gamma}$ is an orthogonal matrix.

$$\boldsymbol{R}_{\alpha\beta\gamma}^{-1} = \boldsymbol{R}_{\alpha\beta\gamma}^{t} \tag{4-5}$$

Equation 4-6 is received through derivation in time of the transformation matrix $\boldsymbol{R}_{\alpha\beta\gamma}$.

$$\boldsymbol{R}_{\alpha\beta\gamma}^{t} \cdot \dot{\boldsymbol{R}}_{\alpha\beta\gamma} = \begin{bmatrix} 0 & -\Omega_3 & \Omega_2 \\ \Omega_3 & 0 & -\Omega_1 \\ -\Omega_2 & \Omega_1 & 0 \end{bmatrix} := \boldsymbol{A}_{\Omega} \tag{4-6}$$

The angular velocity components between the relative and global coordinate system are thereby characterized by the vector $(\Omega_1, \Omega_2, \Omega_3)^t$. Through the above derived transformation relations, the translational distortion component for a partial mass in the associated body coordinate system can be stated as:

$$m_i \cdot \frac{\partial^2 \left(\boldsymbol{R}_{\alpha\beta\gamma} \cdot \boldsymbol{x}_i \right)}{\partial t^2} = \boldsymbol{R}_{\alpha\beta\gamma} \cdot \boldsymbol{f}_{F,i} \tag{4-7}$$

The vector $\boldsymbol{f}_{F,i}$ refers thereby to the forces in the relative coordinate system. The vector of the relative positions is split up into three components according to equation 4-8.

$$\boldsymbol{x}_i = \boldsymbol{x}_B + \boldsymbol{c}_i + \boldsymbol{u}_i \tag{4-8}$$

The position of the origin of the body coordinate system relative to the global coordinate system (measured in the reference coordinate system) is expressed by the vector $\boldsymbol{x}_B$. The position of the node in relation to the relative coordinate system is expressed through the time invariant vector $\boldsymbol{c}_i$, and the vector $\boldsymbol{u}_i$ which represents the translational displacement. Through substitution of equation 4-8 in equation 4-7 and second order time derivation equation 4-9 can be derived.

$$m_i \cdot [\boldsymbol{R}_{\alpha\beta\gamma} \cdot (\ddot{\boldsymbol{x}}_B + \ddot{\boldsymbol{u}}_i) + 2 \cdot \dot{\boldsymbol{R}}_{\alpha\beta\gamma} \cdot (\dot{\boldsymbol{x}}_B + \dot{\boldsymbol{u}}_i) + \ddot{\boldsymbol{R}}_{\alpha\beta\gamma} \cdot (\boldsymbol{x}_B + \boldsymbol{c}_i + \boldsymbol{u}_i)] = \boldsymbol{R}_{\alpha\beta\gamma} \cdot \boldsymbol{f}_{F,i} \tag{4-9}$$

Multiplication of equation 4-9 by the transposed transformation matrix $\boldsymbol{R}_{\alpha\beta\gamma}^{t}$ and considering equation 4-5 and equation 4-6 yields to equation 4-10.

$$m_i \cdot [\ddot{\boldsymbol{x}}_B + \ddot{\boldsymbol{u}}_i + 2 \cdot \boldsymbol{A}_\Omega \cdot (\dot{\boldsymbol{x}}_B + \dot{\boldsymbol{u}}_i) + (\boldsymbol{A}_{\dot{\Omega}} + \boldsymbol{A}_\Omega^2) \cdot (\boldsymbol{x}_B + \boldsymbol{c}_i + \boldsymbol{u}_i)] = \boldsymbol{R}_{\alpha\beta\gamma} \cdot \boldsymbol{f}_{F,i} \quad 4\text{-}10$$

Also, for Euler's equation for angular momentum, the transformation into the relative (body) coordinate system has to be done. Therefore, equation 4-3, 4-4 and 4-5 are substituted in equation 4-2. This leads to equation 4-11, which is the equivalent to equation 4-2 in the body coordinate system.

$$\frac{\partial}{\partial t}\left(\boldsymbol{R}_{\alpha\beta\gamma} \cdot \boldsymbol{I}_{C,i} \cdot \boldsymbol{\omega}_i\right) = \boldsymbol{R}_{\alpha\beta\gamma} \cdot \boldsymbol{f}_{M,i} \quad 4\text{-}11$$

Through substitution of equation 4-11 with equation 4-5 and 4-6, a multiplication with $\boldsymbol{R}_{\alpha\beta\gamma}^t$, and a second order time derivation, equation 4-11 can be written as:

$$\boldsymbol{A}_\Omega \cdot \boldsymbol{I}_{C,i} \cdot \boldsymbol{\omega}_i + \dot{\boldsymbol{I}}_{C,i} \cdot \boldsymbol{\omega}_i + \boldsymbol{I}_{C,i} \cdot \dot{\boldsymbol{\omega}}_i = \boldsymbol{f}_{M,i} \quad 4\text{-}12$$

For each partial mass i the vector of angular velocities $\boldsymbol{\omega}_i$ can be divided into the vector of angular velocity components with respect to the reference coordinate system relative to the global coordinate system $\boldsymbol{\Omega}$.Thus, the vector of the angular velocity components of the partial masses relative to the reference coordinate system can be stated as $\dot{\boldsymbol{\phi}}_i = \left(\dot{\phi}_{i,1}, \dot{\phi}_{i,2}, \dot{\phi}_{i,3}\right)^t$.

$$\boldsymbol{\omega}_i = \boldsymbol{\Omega} + \dot{\boldsymbol{\phi}}_i \quad 4\text{-}13$$

Substituting equation 4-11 with equation 4-12 yields after transformation to:

$$\left(\boldsymbol{A}_\Omega \cdot \boldsymbol{I}_{C,i} + \dot{\boldsymbol{I}}_{C,i}\right) \cdot \left(\boldsymbol{\Omega} + \dot{\boldsymbol{\phi}}_i\right) + \boldsymbol{I}_{C,i} \cdot \left(\dot{\boldsymbol{\Omega}} + \ddot{\boldsymbol{\phi}}_i\right) = \boldsymbol{f}_{M,i} \quad 4\text{-}14$$

For the inertia tensor can be considered that in the body fixed coordinate system the tensor is invariant in time. Thus, it can be written as:

$$\dot{\boldsymbol{I}}_{C,i} = \boldsymbol{A}_{\dot{\phi}_i} \cdot \boldsymbol{I}_{C,i} + \left(\boldsymbol{A}_{\dot{\phi}_i} \cdot \boldsymbol{I}_{C,i}\right)^t \quad 4\text{-}15$$

Through the linearization of the angular velocity and angular acceleration, as well as considering that the inertia tensor is invariant in time, equation 4-14 can be stated as follows:

$$\begin{aligned} &\boldsymbol{I}_{C,i} \cdot \ddot{\boldsymbol{\phi}}_i + \Delta\boldsymbol{I}_{C,i} \cdot \ddot{\boldsymbol{\phi}}_i + \left(\boldsymbol{I}_{C,i} + \Delta\boldsymbol{I}_{C,i}\right) \cdot \left(\dot{\boldsymbol{\Omega}} - \boldsymbol{A}_{\dot{\Omega}} \cdot \boldsymbol{\Omega}\right) + \\ &\left(\boldsymbol{A}_\Omega + \boldsymbol{A}_{\phi_i}\right) \cdot \left(\boldsymbol{I}_{C,i} + \Delta\boldsymbol{I}_{C,i}\right) \cdot \left(\boldsymbol{\Omega} + \dot{\boldsymbol{\phi}}_i\right) = \boldsymbol{f}_{M,i} \end{aligned} \quad 4\text{-}16$$

The following equation system is received by combining equation 4-10 and 4-16.

$$\boldsymbol{M} \cdot \ddot{\boldsymbol{q}} = \boldsymbol{f} \quad 4\text{-}17$$

Whereby, $\boldsymbol{M}$ is a blog diagonal matrix of following form:

$$\boldsymbol{M} = \begin{bmatrix} M_1 & 0 & 0 & 0 & 0 \\ 0 & M_2 & 0 & 0 & 0 \\ 0 & 0 & * & 0 & 0 \\ 0 & 0 & 0 & * & 0 \\ 0 & 0 & 0 & 0 & M_n \end{bmatrix} \quad 4\text{-}18$$

In the above stated mass matrix, each of the n sub-matrices $\boldsymbol{M}_i,\ i \in \{1, \dots, N\}$, is a block diagonal matrix itself, which contain the associated mass m_i that is multiplied by the 3x3 unit matrix $\boldsymbol{E}_3$ as well as the corresponding inertia tensor $\boldsymbol{I}_{C,i}$.

$$\boldsymbol{M}_i = \begin{bmatrix} m_i \cdot \boldsymbol{E}_3 & 0 \\ 0 & \boldsymbol{I}_{C,i} \end{bmatrix} \quad 4\text{-}19$$

The displacement vector of the n partial masses $\boldsymbol{q} = (q_1,\ q_2, \dots,\ q_n)^t$ for the second order derivation of the generalized displacements is $\ddot{\boldsymbol{q}}$. Whereby, $\boldsymbol{q}_i$ is a vector itself, containing the three translational and three rotational motion components $(\boldsymbol{q}_i = (u_1, u_2, u_3, \phi_1, \phi_2, \phi_3)_i^t)$. The force vector $\boldsymbol{f}$ contains the sub vectors $(\boldsymbol{f} = (f_1,\ f_2, \dots,\ f_n)^t)$ for every partial mass considering the forces and moments which are acting on the individual sub-bodies. Further on these force sub vectors can be split up into a sum of the external terms $\boldsymbol{f}_i^{ext}$, the internal terms $\boldsymbol{f}_i^{int}$ as well as the non-linear terms $\boldsymbol{p}_i^*$. Each of the terms consists thereby out of 6 components.

$$\boldsymbol{f}_i = \boldsymbol{f}_i^{ext} + \boldsymbol{f}_i^{int} + \boldsymbol{p}_i^* \quad 4\text{-}20$$

Due to the 6 DOF belonging to one node in 3D space, the force vector $\boldsymbol{f}_i^{int}$ consists out of 6 components:

$$\boldsymbol{f}_i^{int} = \begin{pmatrix} f_{i,\ 1}^{int} \\ f_{i,\ 2}^{int} \\ f_{i,\ 3}^{int} \\ f_{i,\ 4}^{int} \\ f_{i,\ 5}^{int} \\ f_{i,\ 6}^{int} \end{pmatrix} \quad 4\text{-}21$$

As a linear elastic approach is used, each component $\boldsymbol{f}_{i,\ k}^{int}, k = 1, \dots,6$ of equation 4-12 is calculated through

$$\boldsymbol{f}_{i,\ k}^{int} = \sum_{j=1}^{6 \cdot n} \boldsymbol{f}_{i,\ j,\ k}^{int} \quad 4\text{-}22$$

with

$$f_{i,\ j,\ k}^{int} = -\left(d_{i,\ j,\ k} \cdot \dot{q}_k + k_{i,\ j,\ k} \cdot q_k\right) \quad 4\text{-}23$$

Through rearranging equation 4-20 and substitution with equation 4-17 the equation of motion for linear systems for a linear elastic body can be derived.

$$\boldsymbol{M} \cdot \ddot{\boldsymbol{q}} + \boldsymbol{D} \cdot \dot{\boldsymbol{q}} + \boldsymbol{K} \cdot \boldsymbol{q} = \boldsymbol{f}^{ext} + \boldsymbol{p}^{*} \tag{4-24}$$

Whereby, $\boldsymbol{D}$ and $\boldsymbol{K}$ are the damping, respectively stiffness matrix assembled by the damping ($d_{i,\ j,\ k}$) and stiffness ($k_{i,\ j,\ k}$) coefficients. The vector of external forces $\boldsymbol{f}^{ext}$ can be split up into forces and moments introduced through couplings $\boldsymbol{f}^{*}$ as well as external loads $\boldsymbol{f}^{a}$.

$$\boldsymbol{f}^{ext} = \boldsymbol{f}^{a} + \boldsymbol{f}^{*} \tag{4-25}$$

The external loads (e.g. cylinder pressure traces, gas forces, output torques) are either functions given over time (or crank angle) and are pre-calculated or measurement data. Through the joints non-linear forces are introduces to the node.
The non-linear terms $\boldsymbol{p}^{*}$ are a result of the coordinate transformation of equation 4-1 and equation 4-2 in the relative coordinate system of the body. They also cover the inertia components of the body which are a result from global motion.

$$\boldsymbol{p}^{*} = \boldsymbol{f}^{gyros} - \boldsymbol{f}^{rbACC} = (p_1^{*},\ p_2^{*}, \dots,\ p_N^{*})^{t} \tag{4-26}$$

Due to the high non-linearity of $\boldsymbol{p}^{*}$, which considers the rigid body acceleration $\boldsymbol{f}^{rbACC}$ and the gyroscopic force vector $\boldsymbol{f}^{gyros}$, the calculation is highly CPU demanding. Thus, different solution strategies are applied, depending on the global motion properties of each structural component [15].

4.2 Reduction of Degrees of Freedom (Condensation)

In the previous chapter the equation of motion for linear elastic bodies was derived. As outlined before, the equation features highly non-linear terms which are very CPU-costly to calculate. Also, due to the non-linearity as well as the high number of DOF's, a solution in the frequency domain cannot be provided. Thus, an integration in the time domain needs to be done. The number of DOF's significantly influences the time needed to execute the integration. As a reason to this the number of DOF's has to be reduced in order to provide a satisfactory calculation time for the solution. In general, there a several approaches available to reduce the number of DOF's. Thereby, the reduced number of DOF's can be either a sub-quantity of all DOF's, which is called static condensation, or a linear combination of DOF's, which is called modal condensation. Finally, a combination of both approaches is possible and called mixed, or dynamic condensation. As for dynamic problems the third approach is used, it is outlined in more detail in the following section.

4.2.1 Dynamic Condensation of Degrees of Freedom

The through dynamic condensation received set of DOF's consists out of a set of physical DOF's $\boldsymbol{q}_t$, which is retained out of the uncondensed set of DOF's, and a modal set of DOF's which can be understood as the amplitudes of the linear combinations of the unreduced set of DOF:

$$\boldsymbol{q}_a = \begin{bmatrix} \boldsymbol{q}_t \\ \boldsymbol{z} \end{bmatrix} \tag{4-27}$$

The transformation between the physical DOF's $\boldsymbol{q}$ and the modal DOF's $\boldsymbol{z}$ is described by the matrix $\boldsymbol{G}_q^*$.

$$\boldsymbol{q} = \boldsymbol{G}_q^* \cdot \boldsymbol{z} \tag{4-28}$$

Whereby, $\boldsymbol{G}_q^*$.consists of:

$$\boldsymbol{G}_q^* = \begin{bmatrix} G_{tq}^* \\ G_{oq}^* \end{bmatrix} = [a_1, a_2, \dots, a_r] \tag{4-29}$$

$[a_1, a_2, \dots, a_r]$ are the r eigenmodes describing the dynamic behaviour of the system. Due the impossibility of a fully vibrational description done by a purely static reduced system, to the static equation

$$\boldsymbol{q}_o = \boldsymbol{G}_{ot} \cdot \boldsymbol{q}_t \tag{4-30}$$

a term correcting the dynamic behaviour is added:

$$\boldsymbol{q}_o = \boldsymbol{G}_{ot} \cdot \boldsymbol{q}_t + \boldsymbol{G}_{oq} \cdot \boldsymbol{z} \tag{4-31}$$

By a substitution of the modal transformation equation

$$\boldsymbol{q}_t = \boldsymbol{G}_{tq}^* \cdot \boldsymbol{z} \tag{4-32}$$

and

$$\boldsymbol{q}_o = \boldsymbol{G}_{oq}^* \cdot \boldsymbol{z} \tag{4-33}$$

following equation is derived:

$$\boldsymbol{G}_{oq}^* \cdot \boldsymbol{z} = \left(\boldsymbol{G}_{ot} \cdot \boldsymbol{G}_{tq}^* + \boldsymbol{G}_{oq}\right) \cdot \boldsymbol{z} \tag{4-34}$$

As equation 4-34 is valid for all modal DOF's z, following relation can be stated:

$$\boldsymbol{G}_{oq} = \boldsymbol{G}_{oq}^* - \boldsymbol{G}_{ot} \cdot \boldsymbol{G}_{tq}^* \tag{4-35}$$

Through that relation, it is possible to quote a transformation equation which links the physical DOF's with the DOF's of the condensed system.

$$\boldsymbol{q} = \begin{bmatrix} \boldsymbol{q}_t \\ \boldsymbol{q}_0 \end{bmatrix} = \begin{bmatrix} E & 0 \\ \boldsymbol{G}_{ot} & \boldsymbol{G}_{oq} \end{bmatrix} \cdot \begin{bmatrix} \boldsymbol{q}_t \\ \boldsymbol{z} \end{bmatrix} \tag{4-36}$$

With below stated definition

$$\boldsymbol{G}_{fa} := \begin{bmatrix} E & 0 \\ \boldsymbol{G}_{ot} & \boldsymbol{G}_{oq} \end{bmatrix} \tag{4-37}$$

follows

$$\boldsymbol{q} = \boldsymbol{G}_{fa} \cdot \boldsymbol{q}_a \tag{4-38}$$

Through equation 4-38, the relation between the reduced generalized displacement vector $\boldsymbol{q}_a$ and the uncondensed generalized vector $\boldsymbol{q}$ is given by the transformation matrix $\boldsymbol{G}_{fa}$.Thereby, $\boldsymbol{G}_{fa}$ is a dense transformation matrix which includes the static as well as the modal DOF's. Through subdivision, the matrix $\boldsymbol{G}_{fa}$ can be split up in a matrix $\boldsymbol{G}_{fa}^{u}$, which links the vector $\boldsymbol{q}_a$ with the local displacements $\boldsymbol{u}_i$ regarding a node i

$$\boldsymbol{u}_i = \left\{\boldsymbol{G}_{fa}^{u}\right\}_i \cdot \boldsymbol{q}_a \tag{4-39}$$

and a matrix $\boldsymbol{G}_{fa}^{\varphi}$, which links the vector $\boldsymbol{q}_a$ with the local rotations $\boldsymbol{\varphi}_i$ of a node i

$$\boldsymbol{\varphi}_i = \left\{\boldsymbol{G}_{fa'}^{\varphi}\right\}_i \cdot \boldsymbol{q}_a \tag{4-40}$$

[15].

5 Basics on Acoustic Simulation in the Free Field

A brief introduction to the theory of acoustic simulation in the free field is given in this chapter. The mathematical formulation of the steady-state pressure field as well as the boundary conditions at the model are covered. Furthermore, the concept of the wave-based technique (WBT) is stated. Based on an indirect Trefftz approach, the WBT uses wave functions which satisfy the homogenous Helmholtz equation for describing the dynamic response variables. Thus, no error is made inside the calculation domain. For the residuals at the boundaries, a weighted residuals formulation is used to push them towards zero in the integral sense. When directly compared to conventional methods, such as finite element method (FEM) or boundary element method (BEM) which approximate shape functions to describe the dynamic response variables, the WBT models are small. Therefore, the numerical effort is reduced, and calculation time is accelerated. Moreover, models using the WBT approach are not frequency depended [16]. For detailed information it is referred to following publications [17] [18].

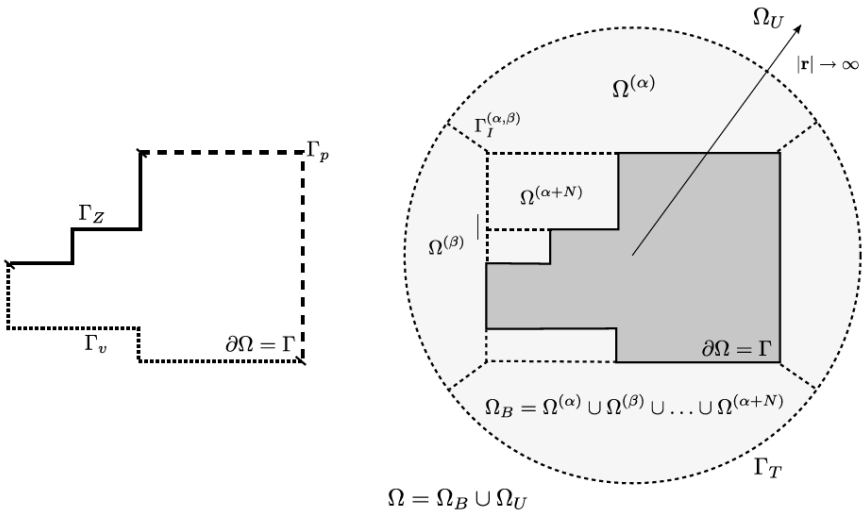

Figure 8: Problem definition of free field with boundary conditions [16]

The acoustic problem illustrated in Figure 8 consists out of an area Ω containing the fluid, as well as a region Γ defining boundary conditions. The boundary conditions separate thereby the calculation area from the free field, they can either be from Dirichlet, Neumann or Robin type and are described in more detail below. Thereby, the fluid is described by its speed of sound c_s as well as its ambient fluid density ρ_0 [16]. For a linear system, with inviscid fluid and an adiabatic process, the steady state pressure field is given wave equation:

$$\frac{1}{c^2}\left(\frac{\partial^2 p'(\boldsymbol{r})}{\partial t^2}\right) - \Delta p'(\boldsymbol{r}) = 0 \qquad 5\text{-}1$$

Thereby, equation 5-1 can be obtained by reformulation of the well-known equations for continuity, impulse, energy as well as the equation of state. Additionally, the equation is valid only for small pressure fluctuations $p'(\boldsymbol{r})$. It describes the pressure field and must be fulfilled for every point in

the calculation domain Ω. Furthermore, equation 5-1 is a homogenous, linear, partial differential equation of second order type. To solve this type of differential equation an arbitrary time harmonic function that is two times differentiable is chosen:

$$p^*(\boldsymbol{r}) = p_h(\boldsymbol{r}) \cdot e^{j\omega t} \tag{5-2}$$

Whereby $\boldsymbol{r}$ describes the position, ω characterizes the circular frequency and j represents the imaginary unit.

Through a substation with the homogenous as well as the particulate approach

$$p'(\boldsymbol{r}) = p^*(\boldsymbol{r}) + p_p(\boldsymbol{r}) \tag{5-3}$$

the system is transferred to an inhomogeneous 2nd order differential equation:

$$-\frac{1}{c^2}\frac{\partial^2 p_p(\boldsymbol{r})}{\partial t^2} - \Delta p_p(\boldsymbol{r}) = \frac{\omega}{c^2} p(\boldsymbol{r}) \cdot e^{j\omega t} \tag{5-4}$$

Through a time harmonic two times differentiable approach for $p_p(\boldsymbol{r})$:

$$p_p(\boldsymbol{r}) = p(\boldsymbol{r}) \cdot e^{j\omega t} \tag{5-5}$$

the homogenous Helmholtz equation is achieved:

$$\nabla^2 p(\boldsymbol{r}) + {k_n}^2 p(\boldsymbol{r}) = 0 \tag{5-6}$$

Where ∇^2 is the Laplace operator Δ and $k_n = \frac{\omega}{c_s}$ is the wave number [16] [19].
For the edge regions of the calculation field, the boundary conditions $\Gamma = \Gamma_p \cup \Gamma_v \cup \Gamma_Z$ are applied as follows:

- Dirichlet (pressure) boundary condition $\tilde{p}(\boldsymbol{r})$ at Γ_p

$$p(\boldsymbol{r}) = \tilde{p}(\boldsymbol{r}), \boldsymbol{r} \in \Gamma_p \tag{5-7}$$

- Neumann (normal velocity) boundary conditions $\tilde{v}_n(\boldsymbol{r})$ at Γ_v

$$v_n(\boldsymbol{r}) = \tilde{v}_n(\boldsymbol{r}), \boldsymbol{r} \in \Gamma_v \tag{5-8}$$

- Robin (impedance) boundary condition $\tilde{Z}_n(\boldsymbol{r})$ at Γ_Z

$$Z_n(\boldsymbol{r}) = \frac{p(\boldsymbol{r})}{v_n(\boldsymbol{r})} = \tilde{Z}_n(\boldsymbol{r}), \boldsymbol{r} \in \Gamma_Z \tag{5-9}$$

Whereby, quantities written with tilde, correspond to values at the boundary conditions of the calculation field.
Additionally, the solution $p(\boldsymbol{r})$ for the above stated problem definition has to fulfil the Sommerfeld-radiation equation, stated in equation 5-10, for $r \to \infty$ at the outer boundary of the calculation domain.

$$\lim_{\boldsymbol{r}\to\infty}\left[|\boldsymbol{r}|\left(\frac{\partial p(\boldsymbol{r})}{\partial|\boldsymbol{r}|} + jk_n p(\boldsymbol{r})\right)\right] = 0 \tag{5-10}$$

Through the above stated boundary conditions as well as the Helmholtz equation, a distinct pressure field $p(\boldsymbol{r})$ is described [16].

6 Fundamentals of Acoustics and Basic Operations in Signal Processing

A short introduction in psychoacoustics, containing the human hearing with its characteristics, as well as the introduction of basic operations in signal processing, necessary for the derivation of CNI and CKI, is given.

6.1 Psychoacoustics

The human hearing operates in a frequency range between around 16 Hz to 16000 Hz, depending on age and physical condition. The lower limit is thereby set by the so-called glimmer bound. Below 16 Hz individual events can be recognized, above they are blurring into one continuous sound [20]. In between, the frequency is grouped into 24 bands, which are in a way selected that each frequency band has the same length of 1.3 mm on the 32 mm long basilar membrane. The basilar membrane is thereby the actual sound receiver, located in the cochlea of the inner ear. The cochlea itself is thereby formed as a spiral. At the beginning it is narrower and stiffer as it is at the end. Through the change of the mechanical characteristics, different frequencies are transmitted at different locations. High frequencies at the beginning of the cochlea (high stiffness, narrow width), and low frequencies at the end (low stiffness, larger width). Each section of the basilar membrane transforms thereby a different frequency group of the received sound to nerve signals. Those 24 frequency bands are also often referred as Bark-scale and listed in Table 1.

Table 1: Bark Scala [19]

z [Bark]	**f [Hz]**	**z [Bark]**	**f [Hz]**	**z [Bark]**	**f [Hz]**
1	100	9	1080	17	3700
2	200	10	1270	18	4400
3	300	11	1480	19	5300
4	400	12	1720	20	6400
5	510	13	2000	21	7700
6	630	14	2320	22	9500
7	770	15	2700	23	12000
8	920	16	3150	24	15500

Each frequency group is again subdivided in 100 Mel. The whole range of audibility consists therefore out of 2400 Mel, corresponding to a linear sectioning of the basilar membrane [19].
When it comes to the subjective hearing impression, the dependency of the perceived tone level is dependent from the frequencies the tone consists of. Thus, same tones emitted from different frequencies, trigger a different sense regarding the perceived sound level. This fact is known as auditory sensation area and illustrated in Figure 9. The different lines mark thereby lines of same sensed sound level over the frequency band. The unit of subjective sound level is Phon.

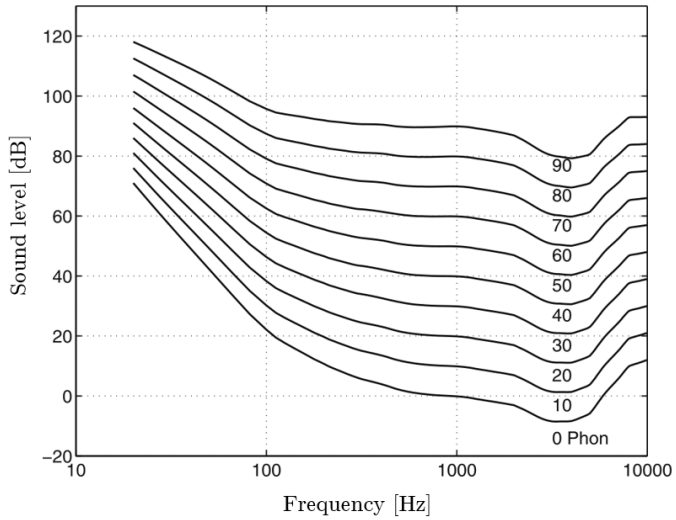

Figure 9: Auditory sensation area [20]

From this fact, the so-called A-weighting can be directly derived. As mentioned above, tones with the same sound pressure level are perceived differently, it is often necessary to rate certain sound events as they are perceived by the human ear. For this case, the A-weighting is introduced in Figure 10.

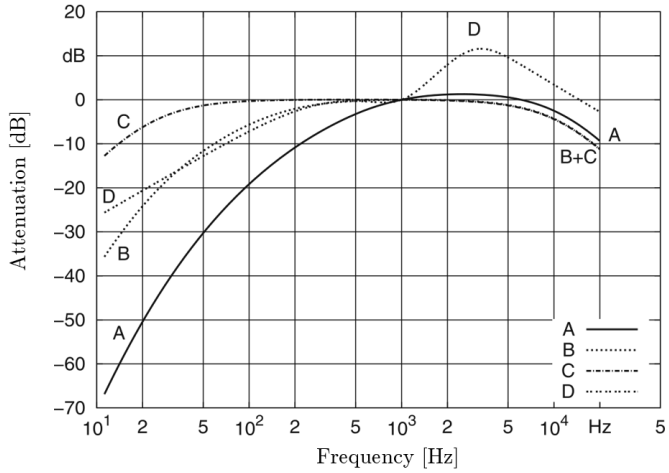

Figure 10: A-, B-, C-, and D-weighting filter traces [20]

The A-weighting corresponds to the inverse curve progression of the trace of same loudness level, passing through 30 dB at 1kHz. In reality, the relation between the objective quantity sound pressure and the subjective quantity loudness is very complex. Thus, a correct consideration of all ear characteristics in the field of technical acoustic would make assessments difficult. As a reason, the A-weighting is introduced as a simple approach [20].
Another important characteristic addresses the masking effect of the human hearing. Thereby, three different types of masking effects are present (Figure 11). Pre-masking is active in a time frame before a masker is active. Directly after follows the simultaneous-masking. In this time frame, the

sound as well as the masker are both simultaneously active. After the end of the masker impulse the post-masking is taking place. Thereby, the masker still acts on the sound even though, it is not physically active any more.

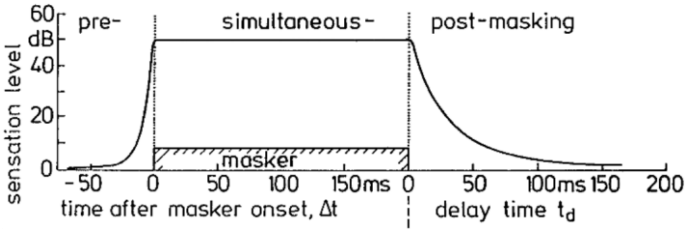

Figure 11: Masking effects [21]

Unlike the post-masking, which is more or less expected, the pre-masking is a surprising effect. It relates on the circumstance, that for a perception a certain time is necessary. If a short processing time is necessary for a loud sound, and a longer timespan for a quiet sound on the edge of perception threshold, it is self-evident that a post-masking has to take place. As the pre-masking takes time for around 20 ms, post-masking lasts up to 100 ms. Therefore, the post-masking is often the dominant masking effect.
The simultaneous-masking describes an effect, where frequency bands in a spectral proximity have an influence on each other. Thus, certain frequency bands are experienced louder or dominant as other bands, which could even be imperceptible completely [21].

6.2 Basic Operations in Signal Processing

In this chapter basic operations in signal processing are derived to satisfy the fundamental knowledge needed to fully derive the CNI code in chapter 11.3 CNI Definition.

6.2.1 Discrete Fourier Transformation and Its Inverse

Periodic functions play an important role in many aspects of nature or engineering, e.g. the work cycle of an internal combustion engine, unbalance of rotating shafts. Those periodic functions contain out of a large number of different frequencies. For certain tasks it is inevitable to know which frequencies a signal contains and on what level of energy they are involved. For this task the discrete Fourier Transformation as well as its inverse are introduced. Both operations are subsections of the so-called Fourier Analysis. To transform a discrete signal, which consists out of measured or calculated samples, from the time domain into the frequency domain (spectrum), the discrete Fourier transformation (DFT) is used. The DFT is defined as:

$$X(k) = \sum_{n=0}^{N-1} x(n) e^{-j2\pi kn/N} \qquad 6\text{-}1$$

For the discrete Fourier Transformation, it is assumed that the signal is sampled by discrete timesteps Δt. Further it is assumed that N is the length of the sampled signal, called the blocksize. Therefore, it can be written as $x(n) = x(n+N)$. Due to computational efficiency the block size N

usually is an integer power number of 2. Whereby the index k runs from $k = 0, 1, \dots, N-1$. This is called the *forward* DFT.
To transform a spectrum from the frequency domain to a signal in the time domain, the *inverse* DFT, or IDFT is used. The IDFT is defined as:

$$x(n) = \frac{1}{N} \sum_{n=0}^{N-1} X(k) e^{j2\pi nk/N} \qquad 6\text{-}2$$

Where $n = 0, 1, \dots, N-1$. [22]

6.2.2 Convolution

By the convolution many different operations are enabled in the field of signal processing. One of the most important one is the task of impulse decomposition. Thereby, the output signal of a linear signal can be described by the input signal and its impulse response. So, it links the three signals of interest *input signal, output signal* and *impulse response* of a system. Also, a convolution of two signals in the time domain, is equivalent to their multiplication in the frequency domain, and a convolution of two signals in the frequency domain corresponds to their multiplication in the time domain. Often, the convolution is outlined by the symbol asterisk *. Thus, the convolution of two signals $x(t)$ and $h(t)$, which results in $y(t)$ can be written as:

$$y(t) = x(t) * h(t) = \int_{-\infty}^{\infty} x(t) h(t-u) du \qquad 6\text{-}3$$

For example, if a *Dirac* impulse is convolved with a signal, the signal is shifted by the time t_0 of the *Dirac* impulse (Figure 12: Convolution of a Dirac impulse with a Signal) [22] [23].

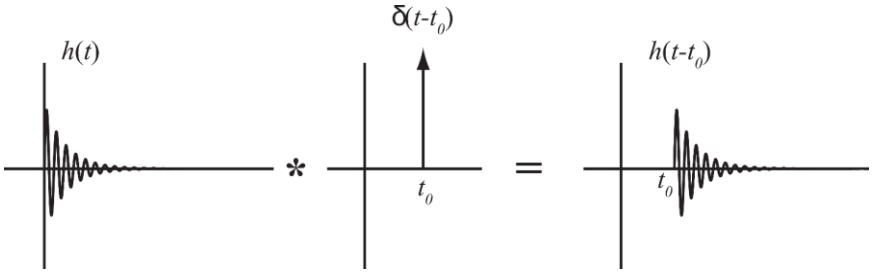

Figure 12: Convolution of a Dirac impulse with a Signal [22]

7 Theory on Combustion Noise Index Algorithm

The combustion noise index (CNI) is a method to describe the harshness of a combustion and is based either on the measured or simulated cylinder pressure trace. It uses the amplitude response of the filtered cylinder pressure trace. With that approach no transformation to frequency domain with following re-transformation after the filtering to time domain is necessary. Through the convolution between the impulse response of the filter with the input signal, the output signal which contains frequency content only between 200 Hz − 6300 Hz is generated. The CNI itself is thereby the peak to peak value divided by the nominal speed of the evaluated engine cycle (equation 7-1). The filter itself is thereby a passband filter for a certain frequency band, relevant for diesel combustion

$$CNI = \frac{abs(max - min)}{angvel} \tag{7-1}$$

In the following paragraph, additional theory on the CNI is outlined. In 11.3 CNI Definition, details to the implementation of the CNI are stated.
For receiving CNI from calculated cylinder pressure traces, a signal filter is used. To realise the implementation of the CNI evaluation in the simulation environment, a script is written in python to process the necessary mathematical operations. As filter type a *FIR* filter is used. Whereby, *FIR* stands for Finite Impulse Response. So, these types of filters deliver a finite number of samples for the impulse response, no matter how the filter parameters are chosen. Also, it is not possible to excite the filter to oscillations, so it gets unstable. The definition of the filter's frequency response was thereby received company internal. This way it is ensured that the simulation results have a good correlation to the measurements.

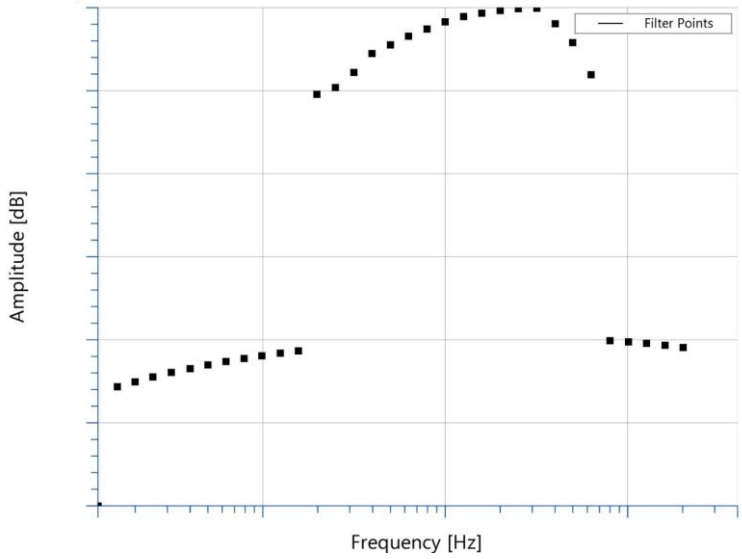

Figure 13: Grid points for filter definition

As pictured in Figure 13, the filter uses a bandpass with best transition between around 200Hz − 6300Hz. Amplitudes at lower and higher frequencies are damped out of the input signal. Since the

filter definition itself was received and developed company intern, no specific explanation of the filter's frequency response is given at this point. The filter itself covers thereby a subjective range of combustion noise, which was developed internal by different acoustic testbed studies. According to Khaira et al. [3], this frequency range is also stated as dominant for internal combustion. The frequency range is thereby subdivided in a low frequency range < 200 Hz, dominated by mechanical phenomena, a medium frequency range from 200 Hz $-$ 6kHz, dominated by combustion, and a high frequency range > 6 kHz which is dominated by resonance phenomena. A general approach for linear, time invariant systems is, to convolve the input signal with the impulse response of the system in time domain to receive the output signal. In Figure 14 the simplified process is outlined. Thus, the convolution links the three signals of a linear time invariant system, namely the input signal, the output signal and the impulse response.

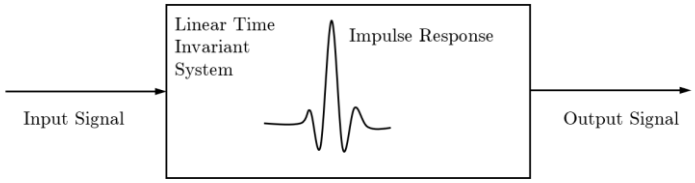

Figure 14: Linear time invariant Systems - Signals

8 Theory on Combustion Knocking Index Algorithm

In this chapter the introduction of the combustion knocking index (CKI) algorithm is established. The algorithm itself was developed internally by AVL and is documented in [24]. The purpose of the CKI is to obtain an objective evaluation index for irritating combustion knocking effects. The algorithm uses a measured or simulated sound pressure signal in time domain as an input. It considers different psychoacoustic effects as frequency dependent listening perception, time masking and frequency masking effects. Those effects are calculated for individual frequency groups and used together with weighting factors for the determination of the CKI:

$$CKI = \sum_{z=1,1.25,\dots}^{24} ((ModulationRest(z))^{p1} * (LoudnessLevel(z))^{p2} * f_z) \qquad 8\text{-}1$$

Whereby p1 and p2 are weighting factors, and f_z is a frequency dependent weighting factor. Details on the algorithm are outlined in the following sections.
According to the characteristics outlined in 6.1 Psychoacoustics, the CKI algorithm is split in 3 independent subsections. After the signal is read in by the algorithm, different tasks are carried out. They are pictured in Figure 15.

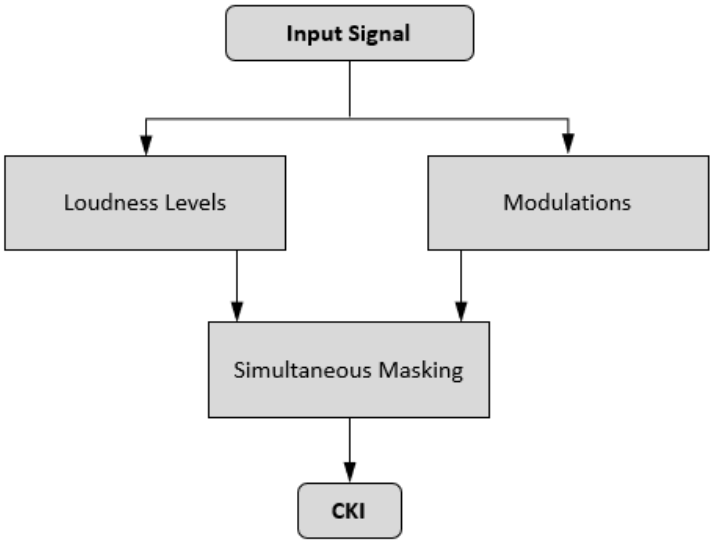

Figure 15: CKI algorithm – structure [24]

In the section "Loudness Levels" the signal is split into blocks, evaluated according to the human hearing through an A-weighting and summed up. The resulting loudness levels are then used as input for the calculation of the simultaneous masking. In the section "Modulations" the signal is again split up into individual blocks and filtered with respect to the human hearing through an A-weighting as well as a bark filter bank. After consideration of the post-masking, the signal is re-sampled with the actual engine speed to cover modulation effects. The calculated modulation values are used as an input for the simultaneous masking. Finally, the simultaneous masking covers the

consideration of the frequency masking as well as the appearance of simultaneous frequency contents in a spectral proximity. Both contents weighted are than used to derive the CKI.

8.1 Evaluation of the Loudness Level

In Figure 16 the individual steps for the calculation of the loudness levels are illustrated. First the signal is split in calculation blocks of 4096 samples each, which overlap at 50%. The overlapping is necessary as too much signal content at the boundary region would be lost when the following window function is applied. For a signal containing N samples

$$M = \frac{N}{2048} - 1 \qquad 8\text{-}2$$

signal blocks are created.
Due to the windowing, the amplitude as well as the energy the signal contains, it is necessary to correct the signal by an amplitude correction factor (AKF) (equation 8-3) as well as an energy correcting factor (EKF) (equation 8-4).

$$AKF = \frac{1}{\frac{1}{T}\int_0^T W(t)dt} = \frac{1}{\bar{A}} \qquad 8\text{-}3$$

$$EKF = \frac{1}{\frac{1}{T}\int_0^T W(t)^2 dt} = \frac{1}{\bar{A}^2} \qquad 8\text{-}4$$

Through an FFT the signal blocks are transformed in the frequency domain, where they are weighted with an A-weighting to consider the frequency dependency of the human hearing.

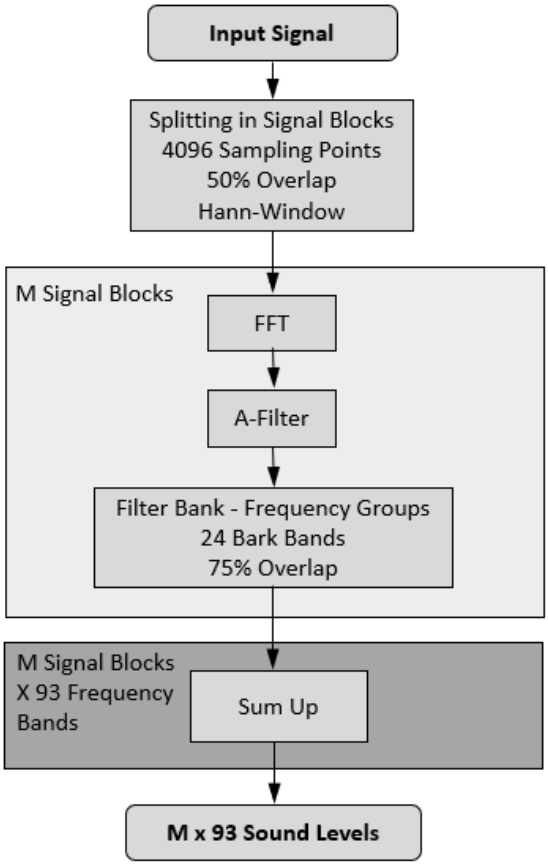

Figure 16: CKI algorithm - evaluation of loudness levels [24]

To take account on the tonal characteristics, the signal blocks pass a filter bank, containing the 24 bark bands with an overlap of 75%. Resulting in a total of 93 filters. The frequencies are cut out with a rectangular window where the stopband has a weighting factor of -100 dB and the passband a weighting factor of 0 dB. For each time block and frequency band a sound level is calculated according to the mean energy of the individual frequencies.

8.2 Evaluation of the Modulation

According to Figure 17, the input signal is split into signal blocks with a size of 28672 samples each, with an overlap of 50% for each block. Again, the overlap is necessary to minimize the amount of information which is lost through the windowing at the boundary areas. By adding 2048 zeros left and right of the original signal block, artefacts which are a result of the convolution in the following calculation steps, can be cut out afterwards. Thus, new signal blocks with a size of 32768 samples result. Through the block size and the overlap

$$P = \frac{N}{14336} - 1 \qquad 8\text{-}5$$

signal blocks result for a signal which is defined by N samples.

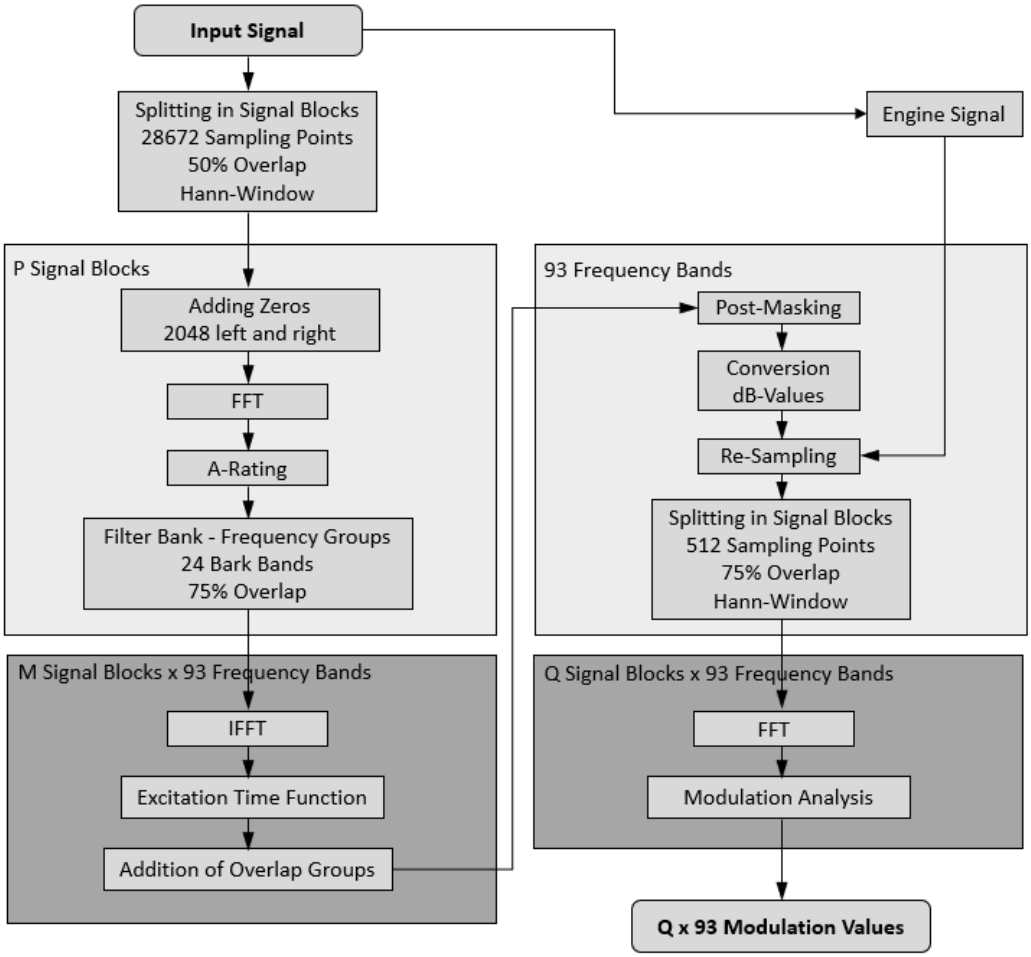

Figure 17: CKI algorithm - calculation of modulation [24]

By an FFT the signal blocks are transformed from time domain to frequency domain and weighted by an A-weighting to comply with human perception. After passing a filter bank containing the 24 bark bands and an overlap of 75%, the signal blocks are transferred back to time domain by an IFFT. Through a Hilbert transformation the excitation time function is calculated from the absolute signal trace.

For each frequency band the signal blocks are added to one continuous time signal. For this task the boundary areas, that consist of 2048 samples left and right, are rejected and the remaining blocks are added with an overlap of 50%.

As described in 6.1 Psychoacoustics, the masking of the human hearing is a nonlinear process. For the CKI implementation the pre-masking is neglected completely due to small relevance. For the post-masking, a time-depended approach is used. Thus, the frequency-dependence is ignored. Instead, an exponential decay curve with 10 dB per 50 ms is chosen.

In the next step the 93 envelopes are transformed to dB-values, as the logarithmic scale corresponds better to the human hearing perception. As reference level for the transformation 20 μPa are select, which matches with the auditory threshold.

As the reason of diesel knocking relates directly to the engine speed, respectively is induced by the engine's fundamental oscillation as well as their harmonics, the time signal is re-sampled in accordance to the engine orders. As the engine orders change during a transient run-up, the frequency spectrum has to be calculated with respect to the engine modulation spectrum. Thus, the former constant sample rate is now adopted on the engine speed. The sampling rate is thereby chosen in a way to achieve results up to the 10^{th} engine order. The interpolation for the individual sampling points is done through a polynomial of 8^{th} order.
After the re-sampling, the signal is again divided in signal blocks. Each block is thereby 512 samples long and has an overlap of 75% for the next block. Resulting in

$$Q = \frac{N'}{128} - 3 \tag{8-6}$$

signal blocks, N' corresponds to the number of samples for the now speed-dependent signal. Each block is windowed with a Hann-window.
For every frequency band z, each signal block Q is transformed through an FFT to frequency domain.
Finally, the modulation orders are analysed.

8.3 Evaluation of the Simultaneous Masking

The process for the evaluation of the simultaneous masking is illustrated in Figure 18. Inputs are the M time values from the level trace, Q time values from the modulation trace, as well as M x 93 frequency band sound levels and Q x 93 frequency band modulation levels. Due to the different block lengths of 4096 samples for the sound level trace and 512 samples for the new speed dependent modulation trace, different time axis for level and modulation are present. Thus, all sound levels of the 93 frequency bands are linear interpolated on the modulation axis. For further processing only these interpolated sound levels are used.
According to 6.1 Psychoacoustics, the masking of certain frequencies through frequencies in a spectral proximity is described. Thereby, the degree of masking is determined by the ratio of the sound levels as well as the spectral distance. In the CKI algorithm modulations which are not audible are neglected, and partial masked modulations are considered in a reduced way.
The left flank (to lower frequencies) of the frequency components is assumed with a level drop of 27 dB per bark, independent from level and frequency. The right flank (to higher frequencies) is dependent from frequency and level. For every timestep and all 93 frequency bands the masking curve is calculated from the sound level values and summed up to a total masking curve.

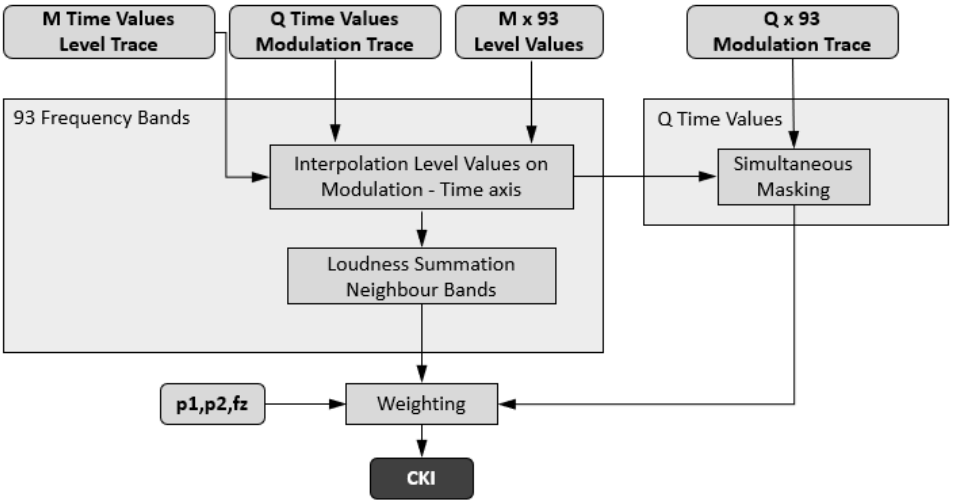

Figure 18: CKI algorithm - calculation of simultaneous masking [24]

From every sound level of each frequency band, the calculated modulation level is subtracted. If the result of the subtraction is above the masking threshold, the modulation level is multiplied by 2 to consider the positive and negative modulation hub. If the result is below the masking threshold the modulation rest is calculated by subtracting the total masking level from the sum of sound level and total modulation.
The sound levels are added up with respect to neighbouring frequency bands, to consider the band width of a signal which goes beyond over a critical band.
Finally, the summed-up sound levels as well as the modulation values are raised to a higher power by weighting factors, and get summed up along the modulation axis to result in the CKI [24].

9 Software

This chapter provides a short introduction of the software environments which are used in this thesis. The theoretic fundamentals of each software package are outlined in the respective theory chapter.

9.1 Cruise™ M

AVL Cruise™ M is a vehicle system simulation platform, which is intended for a model-based system development. In this simulation environment different sub systems like e.g. engine model, driveline, 1D fluid flow, aftertreatment and electrical control systems are integrated into one model. The numerical solver which is adapted for multi-physics vehicle system simulation is thereby combined with a multi-level modelling approach with additional interface standards. This leads to a re-use of subsystems for different tasks in the powertrain development process. Cruise™ M features following tools in its software environment:

- pre- and post-processing
- simulation process control
- parametrization and scenario management
- DoE and optimization
- model compiler for model generation

As for this thesis the engine simulation with mainly combustion simulation tasks is essential, the other parts of the software environment are not further discussed at this point.
The dedicated numerical solvers used for engine simulation are working with either constant time step or implicit adaptive time step integration using transient and steady-state 0D and quasi-dimensional model components. Thereby, basic flow characteristics are modelled through steady-state approaches as well as maps. There are two characteristics to describe the fundamentally different engine approaches:

- Cylinders are crank-angle resolved (including ports) within the framework of a time-resolved gas-path, mechanical and control network components. For the interaction between cylinder and air path, different approaches are thereby possible.
- Modelling of the system with a surrogate engine model which uses support vector machines to predict arbitrary engine quantities (e.g. air delivery, wall heat losses, torque, exhaust enthalpy flow) based on arbitrary data that comes either from test-bed measurements or Boost™ cycle simulation models [9].

At this point it is mentioned that the first outlined approach is used for the engine simulation.

9.2 Excite™

AVL Excite™ is a software tool which features the simulation of rigid as well as flexible multi body dynamic (MBD) of powertrains. With this tool the calculation of dynamics, strengths, vibrations and acoustics of combustion engines, transmissions and conventional or electrical drivelines is possible [15].

9.2.1 Excite™ Power Unit

Excite™ Power Unit is a simulation tool especially for engine analysis and optimization for existing engines as well as power units. The field of application covers thereby:

- Dynamics of crank train an engine components
- Vibration and acoustics of power units (structure born noise)
- 3D piston dynamics
- Bearing analysis

Based on dividing non-linear mechanical systems into linear elastic sub systems the simulation is performed. Whereby non-linearities occur only at the connections between these sub systems. Thus, during the simulation linear elastic bodies interact with each other through highly non-linear connections (e.g. oil film slider bearings). With this approach it is possible to simulate complex structures such as entire power units with a good computational efficiency valid in a range up to 3-5 kHz. The elastic bodies are thereby represented by FE-models which use reduced structure matrices. Typical models that are used for noise, vibrations and harshness (NVH) analysis are composed out of several hundred thousand degrees of freedom (DOF's). Those DOF's are then reduced to approximately 1000 to 3000 dynamic DOF's. To archive this task, an approach based on combined static as well as dynamic reduction, existing in FE-Software, is used. One of the main features are the joints, which allow the coupling of different engine components to simulate real physical effects in gaps and clearances. Due to the highly non-linear behaviour, the simulation is carried out in time domain. An effective time integration algorithm with step size adjustment is thereby provided. Afterwards the results can be transferred in frequency domain [15].

9.2.2 Excite™ Acoustics

Excite™ Acoustics is a tool which enables sound radiation calculation in the free field emitted by vibrating structures such as gear boxes and engine blocks using the so-called Wave Based Technique (WBT). So additional information about the assembly's noise emissions can be provided through direct simulation of radiated air borne noise (ABN). With the structure borne noise (SBN) of the flexible MBD analysis as well with a transfer path analysis, the ABN calculation enables a detailed assessment of the overall noise radiation [16].

10 Measurements

To achieve good results with simulations, measurements are necessary to validate the simulation models. For this thesis, an inline 4-cylinder diesel engine with a displacement of 1.6 litre and a common rail injection system was measured on a testbed. To bypass the need to simulate the whole airpath for the thermodynamic simulation, pressures as well as temperatures directly at the intake respectively outtake were measured. Regarding basic engine parameters speed and torque were measured through a dyno. For the combustion variation performed in chapter 11 Combustion Noise Assessment, detailed data regarding the injection timings are necessary. For this task the injection start, the injection duration as well as the fuel amount was measured. Additionally, the pressure of the common rail system was measured as well.
For the structural vibrations analysis, excitations were measured for the front bracket as well as the torque arm, microphones for acoustic investigations were placed at multiple positions around the engine and illustrated in Figure 19 and Figure 20. The distance between the engine and the microphones was thereby set for 1 meter.

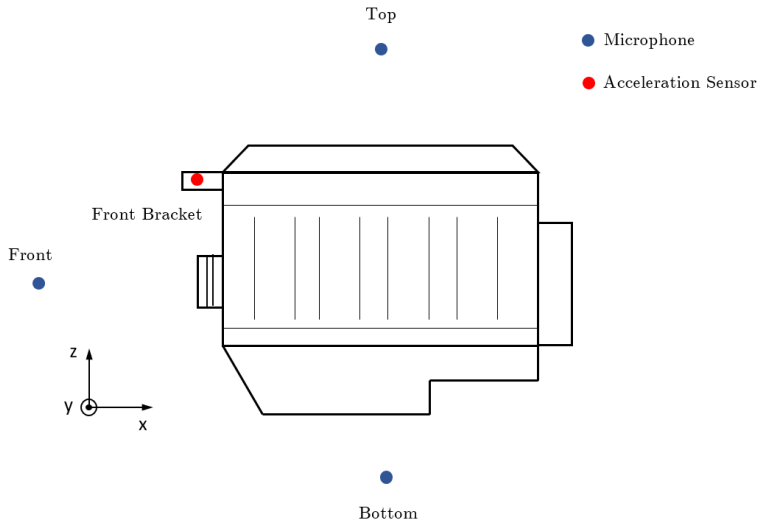

Figure 19: Acceleration sensor and microphone positions - side view

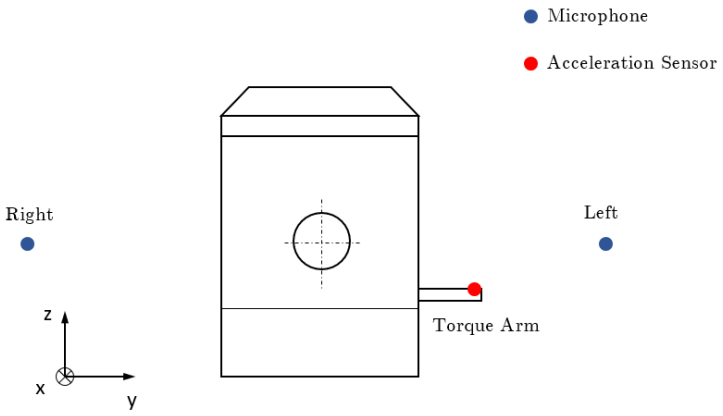

Figure 20: Acceleration sensor and microphone positions - front view

10.1 Nomenclature Definition

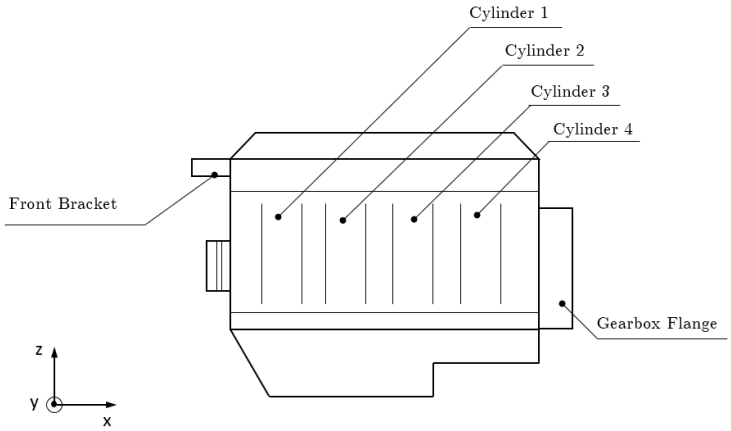

Figure 21: Engine nomenclature measurements

As illustrated in Figure 21, the front bracket is directly located at cylinder 1. The counting scheme for the numeration of the cylinders is starting thereby at 1 at the opposite side of the output shaft (where the clutch is located). As rotation axis for the crank, x-axis is set.

10.2 Operating Points

To fit the characteristics of the physical engine that was measured, it is necessary to calibrate the model for the measured operating points. Those operating points are stated in Table 2.

Table 2: Speeds and number of injections for the measured engine

Operating Point	Speed [rpm]	Number of Injections
IFILE 1	1500	3
IFILE 2	1500	3
IFILE 3	1500	3
IFILE 4	1500	3
IFILE 5	1500	3
IFILE 6	1500	3
IFILE 7	1500	2
IFILE 8	1500	1
IFILE 9	1500	1
IFILE 10	1500	1
IFILE 11	1500	1
IFILE 12	1500	3
IFILE 13	1500	3
IFILE 14	1500	3
IFILE 16	2000	3
IFILE 17	2000	3
IFILE 18	2000	3
IFILE 19	2000	3

IFILE 20	2000	3
IFILE 22	2000	3
IFILE 23	2000	2
IFILE 24	2000	1
IFILE 25	2000	1
IFILE 26	2000	1
IFILE 27	2000	1

All operating points are steady state for every case. The measurements where performed for 10 seconds each at a load of 100%. To eliminate the deviations between different cycles of the same operating point, approximately 100 cycles were measured and averaged afterwards. Through this approach it is ensured to level out certain errors occurring cycle dependent during the run as well as during the measurements itself. A variation of the injection timing was therefore performed regarding Table 3. To cover different injection strategies, a variation of the injection regarding main -, pilot -, and pre – injection was done. Therefore pilot -, and pre - injections were switched off for main injection operation or introduced for multi - injection operation.

Table 3: Injection variation timings for combustion calibration

Operating Point	SOI MA [deg CA]	SOI PR [deg CA]	SOI PI [deg CA]	DUR MA [deg CA]	DUR PR [deg CA]	DUR PI [deg CA]
IFILE 1	2,48	-6,07	-14,73	7,78	1,38	1,42
IFILE 2	3,49	-5,07	-13,72	7,88	1,39	1,46
IFILE 3	5,51	-3,06	-11,71	8,09	1,37	1,44
IFILE 4	7,49	-1,08	-9,73	8,39	1,41	1,45
IFILE 5	9,45	0,93	-7,73	8,44	1,36	1,43
IFILE 6	2,48	-6,09	-14,74	7,98	1,37	1,42
IFILE 7	2,51	-6,14	-	8,84	1,49	-
IFILE 8	4,00	-	-	9,21	-	-
IFILE 9	2,51	-	-	9,14	-	-
IFILE 10	1,52	-	-	9,08	-	-
IFILE 11	0,52	-	-	9,03	-	-
IFILE 12	2,48	6,08	-14,74	8,05	1,37	1,42
IFILE 13	2,59	-5,95	-14,57	7,60	1,39	1,43
IFILE 14	2,70	-5,83	-14,46	7,56	1,32	1,38
IFILE 16	-0,92	-12,26	-23,79	9,25	1,71	1,83
IFILE 17	-0,01	-11,42	-23,01	9,23	1,73	1,85
IFILE 18	0,93	-10,45	-22,04	9,32	1,74	1,86
IFILE 19	2,84	-8,55	-20,14	9,58	1,74	1,86
IFILE 20	4,75	-6,64	-18,23	9,61	1,76	1,88
IFILE 22	-0,97	-12,32	-23,84	9,27	1,72	1,83
IFILE 23	-0,90	-23,84	-	10,89	1,85	-
IFILE 24	-0,90	-	-	11,13	-	-
IFILE 25	0,59	-	-	11,42	-	-
IFILE 26	-1,91	-	-	11,12	-	-
IFILE 27	-2,91	-	-	11,02	-	-

Where (SOI) stands for start of injection, (DUR) characterizes the duration of the injections and (MA), (PR) and (PI) cover the main, pre and pilot Injection. All values are measured in degree crank angle and are related to the top dead center (TDC).

10.3 Cycle Variation During Steady State Operation

In this subchapter a deeper glance is thrown at the cycle variation which occurs in the measurements. Under the term cycle variation, one can commonly understand the deviation between individual cycles of one operating point and condition. In this case, approximately 150 cycles were performed for each operating point. Through many effects in the measurement chain as well as the testing procedure itself, it is evident that fluctuations over steady state cycles will occur in the final measurement results.
During the testbed measurements, vibrations at three positions for three spatial directions were measured. One accelerometer was located at the front-bracket, one at the rear-bracket and one accelerometer at the torque arm of the engine. For each engine operating point, the measurement was performed for 10 seconds. Below the cycle variation for individual operating points is shown by means of a 1/3 octave band. Therefore, per case the 10 seconds vibrational measurement data is split into 10 partitions containing one second of signal content each. For 1500rpm, one second contains approximately 12,5 engine cycles, for 2000rpm one second contains approximately 16,67 engine cycles. As reference points two operating points are selected for each speed. Thereby, the selected operating points represent highest and lowest knock for their referenced speed. For 1500rpm operating point IFILE 1 corresponds to the lowest combustion knock, IFILE 8 to the highest. Due to confidentiality reasons, only the min. as well as max. value is marked for the ordinate in the following plots.

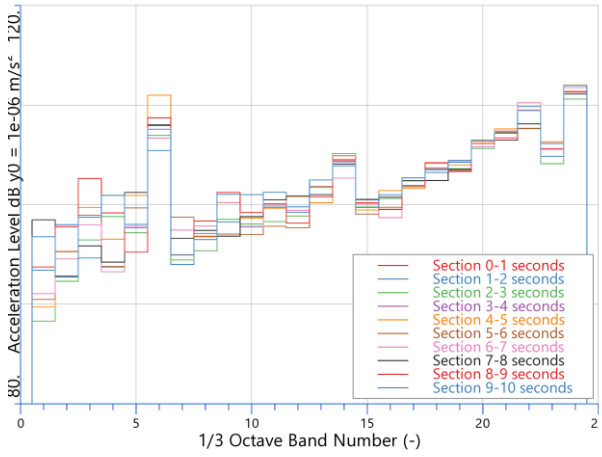

Figure 22: Cycle variation front bracket DOF 2 - IFILE 1 - 1500rpm

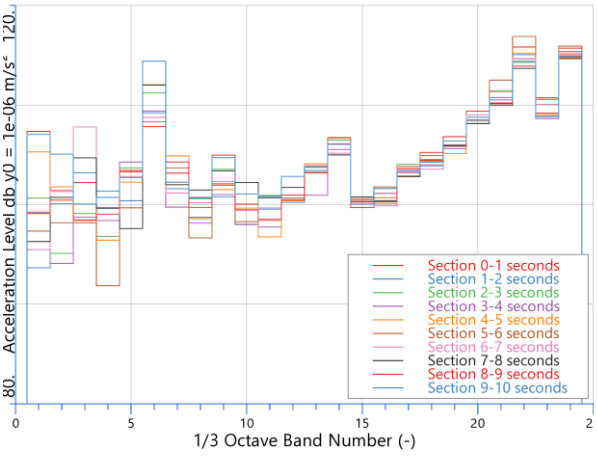

Figure 23: Cycle variation front bracket DOF 2 - IFILE 8 - 1500rpm

In Figure 22 and Figure 23 the cycle variation between operating point high knock and low knock for 1500rpm is illustrated through a third octave band. Thereby, the cycle variation for third octave bands starting from #12 (or 160 Hz center frequency) upwards is smaller than 3 dB acceleration level. 3 dB is thereby set as a rough quality criterion as a deviation of 3 dB in level corresponds to around 40 % fluctuation in amplitude. Furthermore, the hearing threshold of a human being is located at around 3 dB. As frequency ranges of interest are starting around third octave band #17

(or 500 Hz center frequency), the deviation in cycle variation is satisfying for dominant frequency ranges.
To get a better understanding of the influence of the front bracket regarding the transfer path for the cycle variation evaluation, the third octave band over 10 one second cycles is also illustrated for the torque arm in Figure 24 and Figure 25.

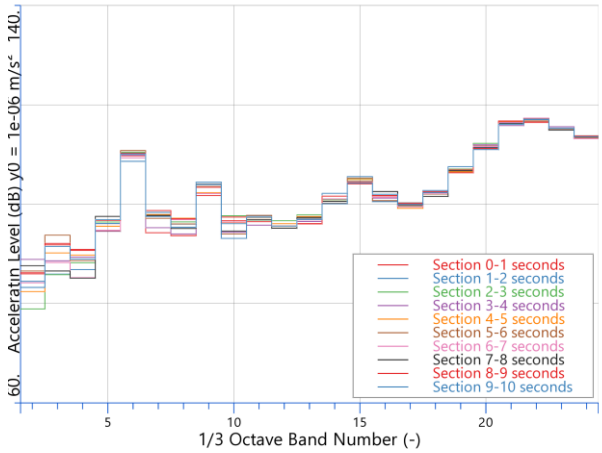

Figure 24: Cycle variation torque arm DOF 2 - IFILE 1 - 1500rpm

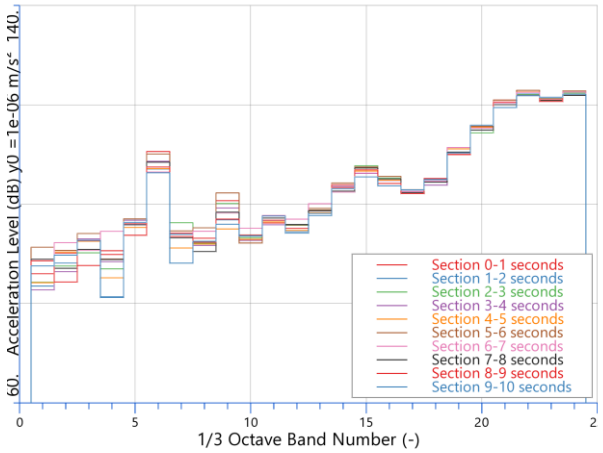

Figure 25: Cycle variation torque arm DOF 2 - IFILE 8 - 1500rpm

A similar picture as for the front bracket, is also given for the torque arm. However, the deviations for acceleration levels above third octave band #17 with around 1 dB are even lower compared to the front bracket.
For 2000rpm IFILE 22 is selected for low knock as well as IFILE 25 for high knock. The acceleration is again evaluated at the front bracket. With a deviation of 2 dB for the third octave band #12 and above, the measurements are again in a satisfying range regarding cycle to cycle variation. The associated third octave bands are illustrated in Figure 26 and Figure 27.

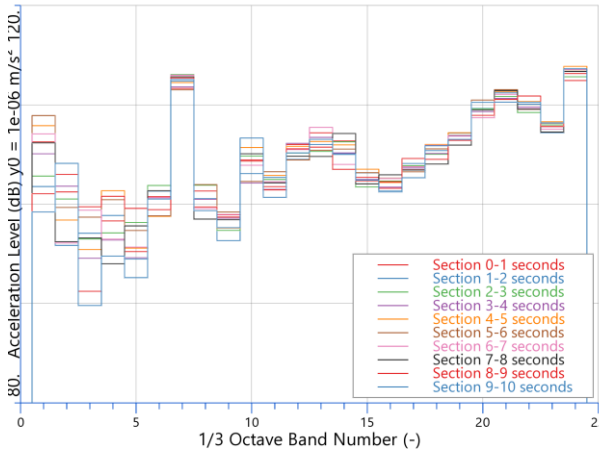

Figure 26: Cycle variation front bracket DOF 2 - IFILE 22 - 2000rpm

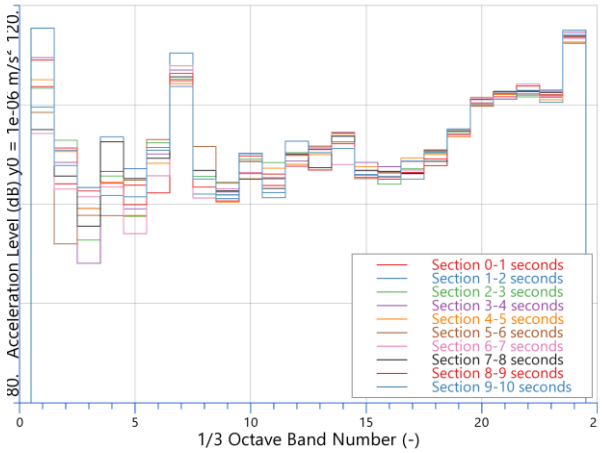

Figure 27: Cycle variation front bracket DOF 2 - IFILE 25 - 2000rpm

10.4 CNI Sensitivity in Measurements

To analyse the impact of the deviation in the CNI in terms of cycle to cycle variation, the highest as well the lowest CNI of one operating point are compared against each other. The comparison is thereby done by acceleration on the front bracket as well as sound pressure both in time- and frequency domain. As reference, operating point IFILE 1 which features 3 injections, and operating point IFILE 8 which features 1 injection are picked.

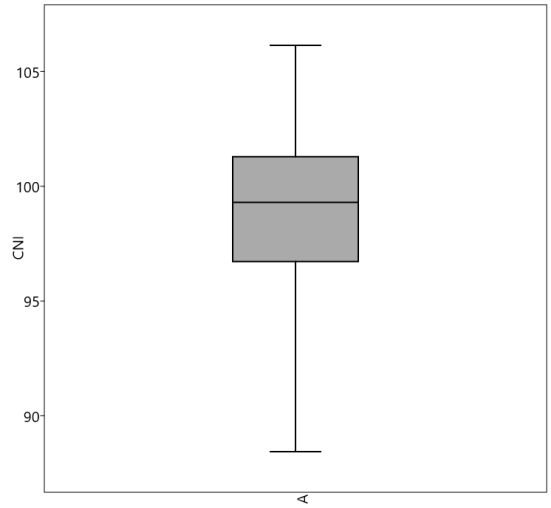

Figure 28: Distribution CNI IFILE 1

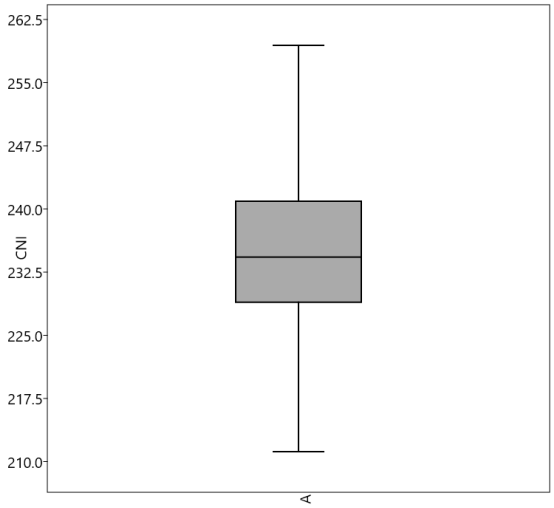

Figure 29: Distribution CNI IFILE 8

Figure 28 and Figure 29 illustrate the distribution of the CNI index for the two picked operating points IFILE 1 and IFILE 8. Thereby, approximately 200 cycles each where evaluating regarding to CNI. The boxplot which is used demonstrates the overall scattering of the CNI index. The box itself contains thereby 50% of the samples, the arithmetic average is marked by a horizontal line through the box. The upper, respectively lower, antenna contains 25% of the measured values each. What is clearly evident, is the scattering of the CNI values over a relatively wide range. This circumstance leads directly to two conclusions:

1. The CNI value has a predictive character, absolute levels are overall not really comparable.
2. For simulation tasks it should not be top priority to focus deeply on one cycle, moreover a wider range of different cycles should be considered, to cover possibly fluctuations in the cycle to cycle variation.

Thereby, the highest as well as the lowest CNI over all cycles are picked for cylinder 1 for both operating points. Cylinder 1 is chosen as it is according to Figure 21 closest to the front bracket. The acceleration on the front bracket is evaluated in +Z direction. As on the back side of the engine no microphone position is available, instead of sound power level, mean sound pressure levels are evaluated over all 5 microphone positions.

For IFILE 1 the lowest CNI can be found at cycle 51, the highest at cycle 75. The CNI's for all 4 cylinders and both cycles are stated in Table 4 and Table 5.

Table 4: IFILE 1 - low CNI cycle

Cylinder	CNI [-]
1	91
2	122
3	92
4	113

Table 5: IFILE 1 - high CNI cycle

Cylinder	CNI [-]
1	106
2	122
3	91
4	112

For an inline 4-cylinder engine, the firing order can be stated as 1-3-4-2. In Figure 30 and Figure 31 the ignition of each cylinder is visible. The illustration contains thereby one engine cycle which is 720 degCA. Thus, each cycle contains thereby two crankshaft revolutions, and as it is a 4-stroke engine, one revolution of the camshaft. Excitations are thereby classified by the frequency they are occurring per engine rotation. Thereby, first order excitations are coming from the crankshaft, and 0.5 order excitations are originating from the camshafts. Higher order vibrations are thereby coming from assemblies as the oil pump or the tooth belt with its polygon effect driving the valve train. The change in the vibration time signal for low CNI cycle as well as high CNI cycle is minor according to Figure 30 and Figure 31 for all 4 cylinders. This can be traced back to the fact that the CNI is very sensitive to changes in the cylinder pressure trace. Additionally, no structural damping characteristics are considered in the CNI algorithm. Further information on the CNI can be found in 11.3 CNI Definition.

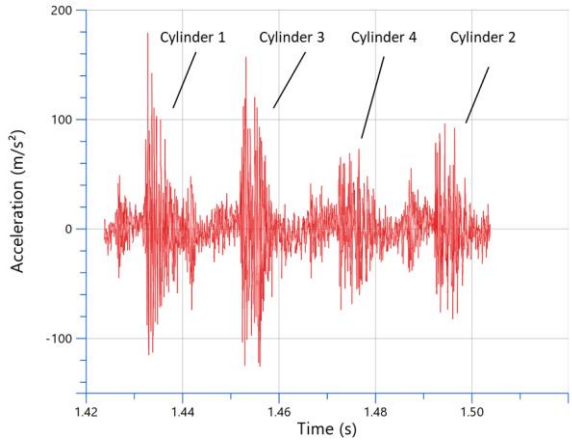

Figure 30: Acceleration +Z direction - IFILE1 low CNI cycle

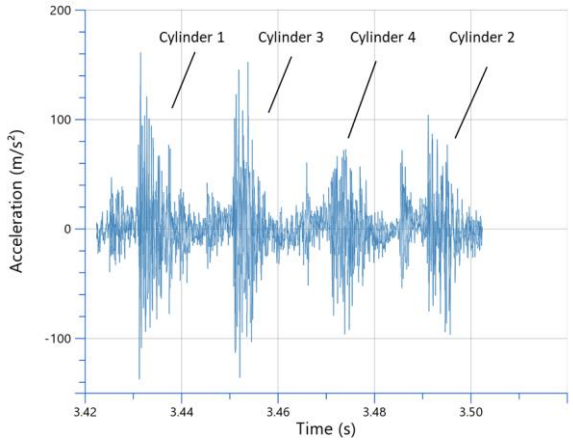

Figure 31: Acceleration +Z direction - IFILE1 high CNI cycle

For the frequency content of the signal, illustrated in Figure 32 and Figure 33, the differences between low and high CNI cycle are minor. The signal is thereby showed for a frequency range between 500 Hz – 4000 Hz. This corresponds according to [25] to the frequency range of most interest for internal combustion engines, as most of the structural resonances are located in that range. The biggest deviation occurs thereby for the 16th octave band, which covers a frequency range between 500 Hz – 562 Hz, with a deviation of 5.39 dB. For the remaining 1/3 octave bands the deviation is small with a maximum of about 2 dB. The difference is also minor at the radiated sound, evaluated as mean sound pressure level over all microphones, stated in Table 6. The mean value of the sound pressures is evaluated to cover certain changes in the sound radiation characteristics for the individual cases.

Table 6: Mean sound pressure - IFILE1

Cycle	Mean Value Sound Pressure [dB]
IFILE1 – low CNI	81,67
IFILE1 – high CNI	81,97

As illustrated in Figure 32, the frequency spectrum is relative constant over the frequency range, this is due to the reason that the combustion takes place in a very short time span. As described in 2.2 Combustion and ROHR, this is especially true for the premixed combustion phase. Therefore, the sudden rise of cylinder pressure acts like an impulse on the structure. Thus, it excites all modes that are capable of spreading for the induced energy level.

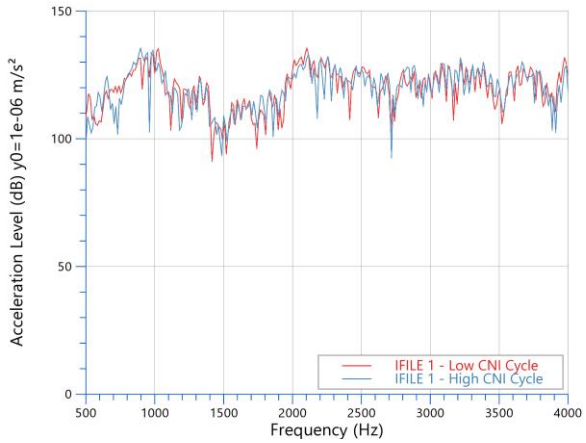

Figure 32: Acceleration level +Z direction - IFILE1 low/high cycle

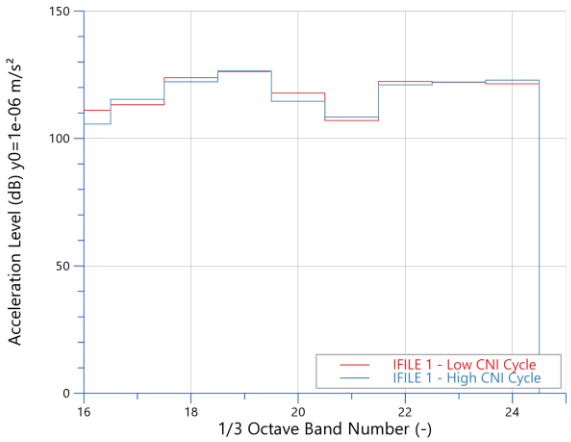

Figure 33: 1/3 Octave band +Z direction - IFILE1 low/high cycle

For the high knock operating point, IFILE 8 is selected. The speed for the engine is set at 1500 rpm for this operating point. The cycle with lowest CNI for cylinder 1 can thereby be found at cycle 39, the one with highest CNI at cycle 128. For all 4 cylinders the CNI levels for the lowest as well as highest CNI cycle for cylinder 1 are stated in Table 7 and Table 8.

Table 7: IFILE 8 - low CNI cycle

Cylinder	CNI [-]
1	212
2	219
3	234
4	231

Table 8: IFILE 8 - high CNI cycle

Cylinder	CNI [-]
1	256
2	242
3	231
4	231

As outlined for operating point IFILE 1, the vibration signal contains low frequency content coming from crankshaft and camshafts rotations, as well as higher frequency content coming from the valve train and other sources, especially the premixed phase of the combustion. The firing order is again stated as 1-3-4-2 and illustrated for the vibration signal of the front bracket in +Z direction in Figure 34 and Figure 35, for low as well as high CNI cycle. The increase in CNI for cylinder 1 is thereby apparent. This can be traced back to the high change of CNI of 44, compared to the change for IFILE 1 of 15. The fluctuation for cylinder 2 in the vibration time signal is small as the fluctuation in CNI is small, but also the transfer path to the front bracket is longer as it is for cylinder 1. Therefore, the signal is more damped by the structure is it is for cylinder 1 which is

located directly at the front bracket. For cylinder 3 and cylinder 4 the time signal is similar as it would be expected regarding the CNI values stated in Table 7 and Table 8.

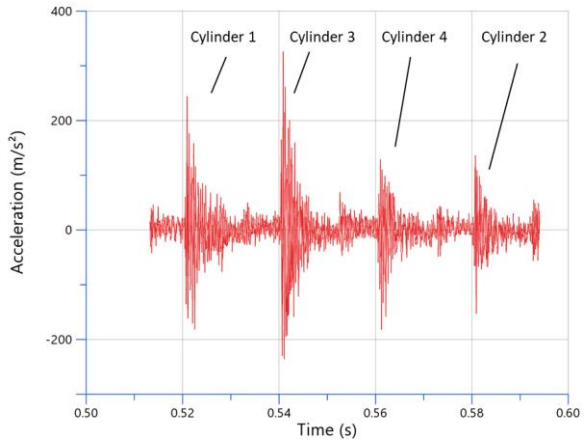

Figure 34: Acceleration +Z direction - IFILE8 low CNI cycle

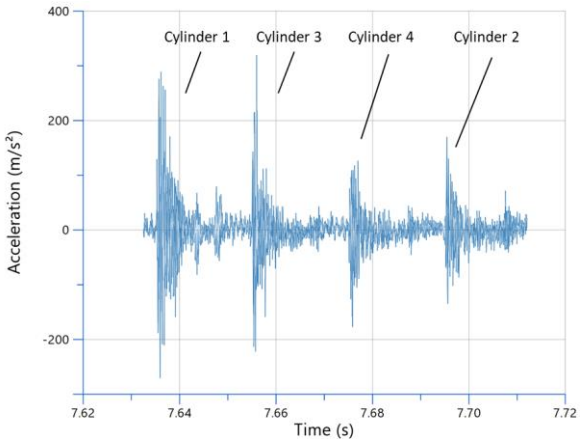

Figure 35: Acceleration +Z direction - IFILE1 high CNI cycle

Again, the change in mean sound pressure level is minor between low CNI and high CNI cycle for cylinder 1.

Table 9: Mean sound pressure - IFILE8

Cycle	Mean Value Sound Pressure [dB]
IFILE8 – low CNI	84,17
IFILE8 – high CNI	83,99

Again, the acceleration levels are relatively constant over the frequency range, for the 1/3 octave bands the highest deviation occurs at the 21st band with a deviation of 3 db. For the remaining 1/3 octave bands the highest deviation is 2 db.

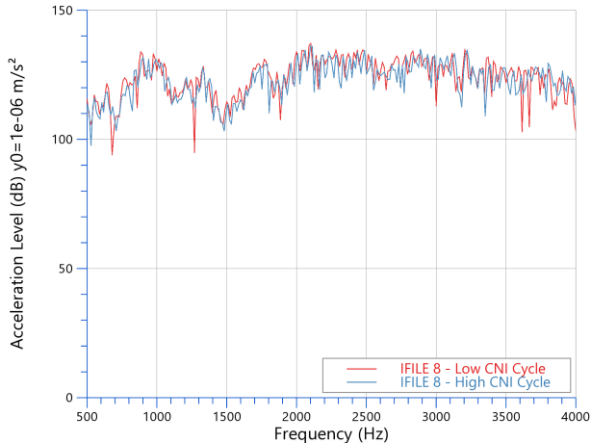

Figure 36: Acceleration level +Z direction - IFILE8 low/high cycle

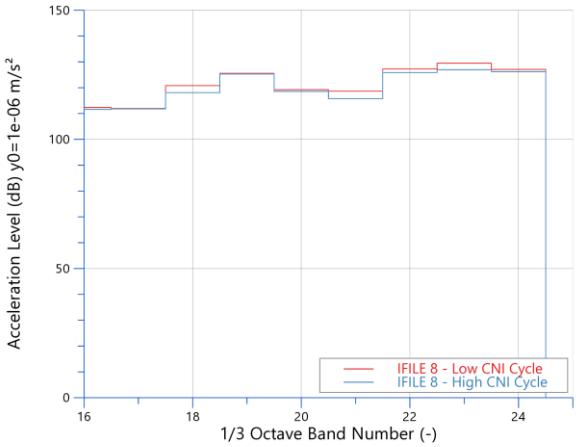

Figure 37: 1/3 Octave band +Z direction - IFILE8 low/high cycle

For low knock operating point IFILE 1 as well as high knock operating point IFILE 8, both cases for high and low CNI cycle at cylinder 1 have only minor impact on the overall acceleration levels measured at the front bracket. Also, the impact on the radiated noise is neglectable. Thus, the CNI is very vulnerable for fluctuation between individual engine cycles, as no damping of the structure is considered which would reduce these fluctuations.

For low, respectively high knock operating point IFILE 1 and IFILE 8 the averaged sound pressure level over all cycles is outlined in Figure 38.

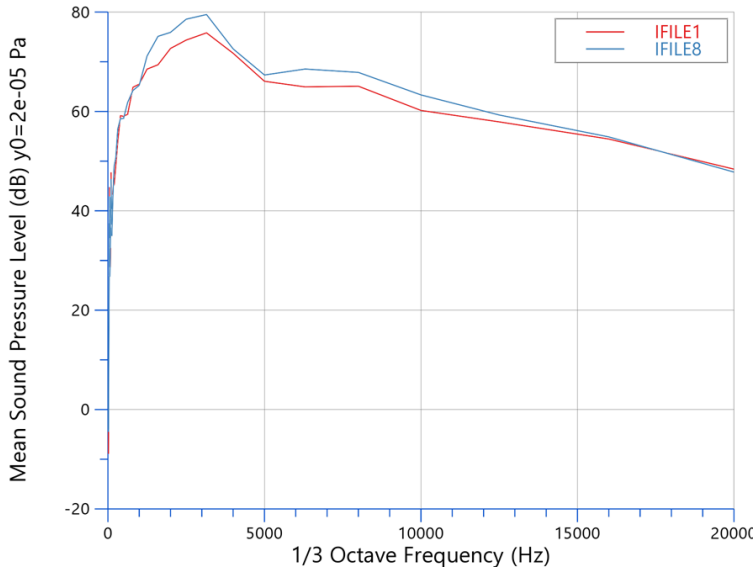

Figure 38: Averaged sound pressure comparison - low/high knock operating points

10.5 Influence of Sampling Rate

At this point a short glimpse is given at the influence of the sampling rate of the measured signal. In Figure 39 and Figure 40 two signals are compared against each other. Both signals are thereby identical. However, one was exported with a resolution of 1 degCA, the other with 0.1 degCA. Around the combustion phase, illustrated in Figure 40, the difference between the traces are evident. Due to the low sampling rate of 1 degCA, higher order combustion effects can not be considered at all.

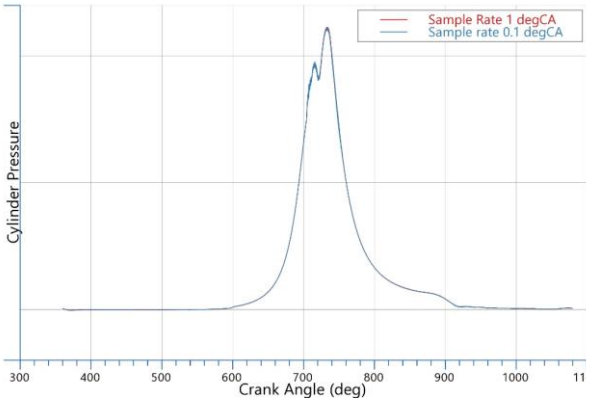

Figure 39: Sensitivity check pressure trace

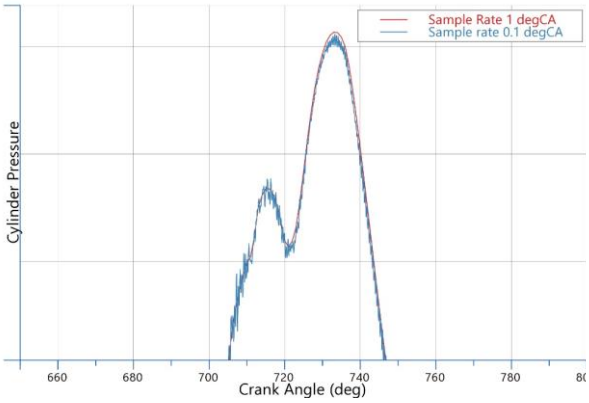

Figure 40: Sensitivity check combustion phase

The influence of the different sampling rates is of course also noticeable in the CNI values. Thereby, the low-resolution variant features a CNI value of 286, and the high resolution one of 303. This difference is as stated above, fully contributed to the lack of higher order combustion dynamics which are completely missing in the 1 degCA sampling rate example.

11 Combustion Noise Assessment

11.1 Model Introduction

The model which is build up and used for the evaluation of the CNI is introduced in this chapter. The model itself is a 0D/1D transient engine model which is shown in Figure 41. The figure represents the individual sub-elements such as combustion chamber, valves, heat transfer connections and injection system.

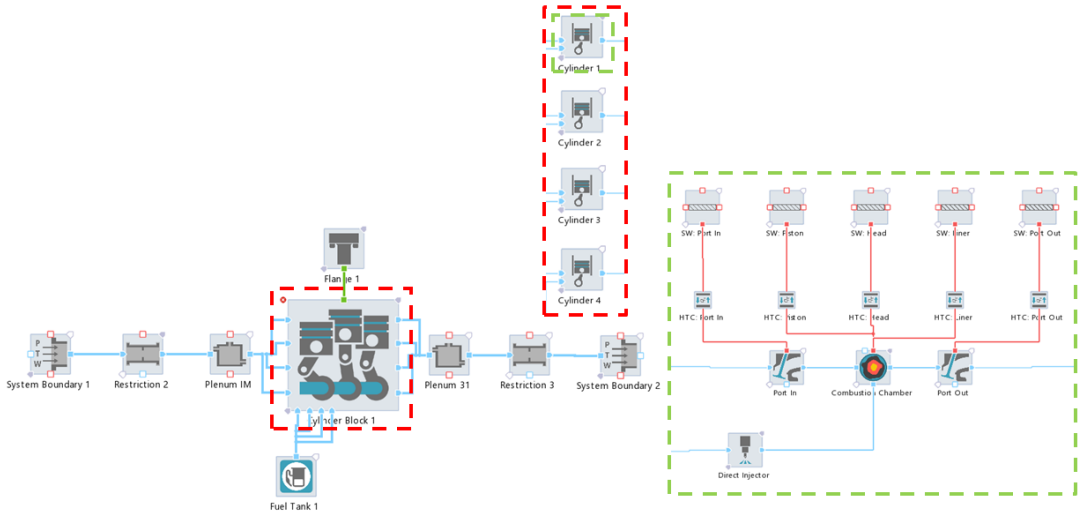

Figure 41: Engine model with individual elements which are build-up of sub-elements

As CNI as well as CKI are setting up on input signals in time domain, it is necessary to generate the cylinder pressure data also in time, respectively crank angle domain. This is particularly true when comparing the effective CNI values with the associated peak cylinder pressure (Figure 75 and Figure 76). Through these illustrations it is evident that peak cylinder pressure and high CNI have no need to correlate. Thus, the complete cylinder pressure for one cycle is necessary. Another reason for a time, respectively crank angle domain, model is the need to cover independent injections for combustion variation. As different injection strategies with pre- and pilot injections have a significant influence on the performance as well as noise, a capable combustion and injection model is required. All the above stated requirements are possible with the model introduced and calibrated in this chapter.

As the measurements for the relevant data needed for the simulation was done directly at the intake and outlet of the engine, the modelling is done without the need of a representation of the entire air path of the engine. Thus, components as e.g. EGR-valve, turbocharger and air cleaner can be left out. The above model contains out of an intake- and outlet port where the measured quantities are set as system boundaries and an engine block that contains out of 4 cylinders. Each cylinder exists thereby out of an intake- and outlet valve, a combustion chamber, a direct injector and artificial walls with heat transfer connections to represent the correct heat loss over the engine walls. Since no air path is modelled, the interaction between each cylinder can be neglected as well. The basic properties of the physical engine are stated in Table 10.

Table 10: Basic physical engine data

Number of Cylinders	4
Compression Ratio	Confidential
Bore	Confidential
Stroke	Confidential
Injection System	Common Rail
Number of Valves/Cyl.	4

Due to confidentiality reasons not all engine data is stated.
Additionally, it is mentioned that the model is build up in Cruise™ M version R2018a.

11.1.1 Parameters for Combustion Variation

To do an assessment of the CNI, different operating points of the engine need to be covered. These operating points distinguish itself mainly by the shape of the combustion pressure trace, by which the CNI is evaluated. Hence, as outlined in chapter 2.1 Injection and Its Main Control Parameters, the primary inputs for the combustion variation are the injection timings as well as the number of injections. This injection signal is directly transferred as input for the direct injector with reference to TDC. From that signal the injector calculates the timing as well as the fuel mass which is injected in the combustion chamber. For detailed information about the mathematical framework of the injector it is referred to 3.2 Injection and High-Pressure Rail Model.

11.1.2 Boundary Conditions

For the model introduced in 11.1, several additional boundary conditions are necessary to define the model completely. Those boundary conditions must be set for all operating conditions. The boundary conditions for pressure and temperature must be set for the inlet as well as the outlet, respectively. By this boundary condition, the air mass flow through the engine is calculated. For the injector the rail pressure is set regarding the current operating condition. For the friction mean effective pressure (FMEP), which is needed as an input parameter for the calculation of the losses as well as the performance delivered by the engine, the break mean effective pressure (BMEP) is required. from the measurements. Thereby, the BMEP is the mean effective pressure calculated from the measured brake torque on the testbed. The IMEP represents the indicated mean pressure over one engine cycle, and the FEMP represents the internal losses of the engine over one cycle as a pressure. By a function which reads out the current cycle averaged indicated mean effective pressure (IMEP), FMEP is calculated simply through subtracting BMEP from IMEP. As shown in Figure 42, BMEP is not extracted for each operating point from the measurements, but rather through an interpolated map to achieve arbitrary operating points.

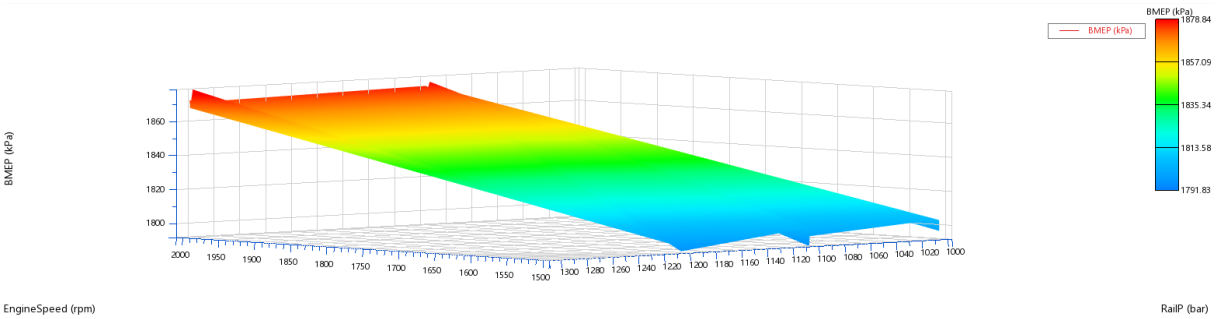

Figure 42: Interpolated map for BMEP

The valve lift is defined over a table both for intake and outlet valves. Since this is an engine without a variable valve train, the valve lift is constant through all operating conditions. The valve lift over the crank angle for intake and outlet valve is illustrated in Figure 43 and Figure 44.

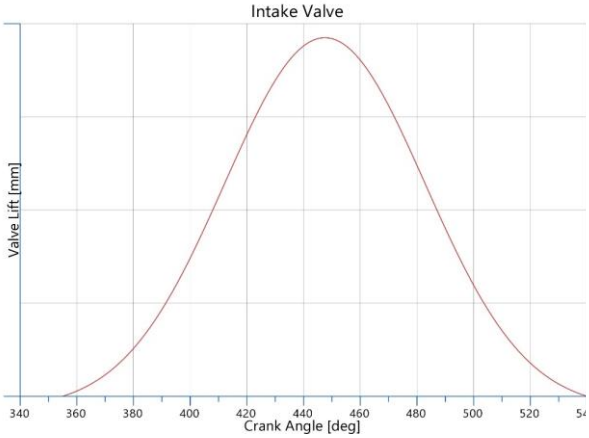

Figure 43: Valve lift table of intake valve

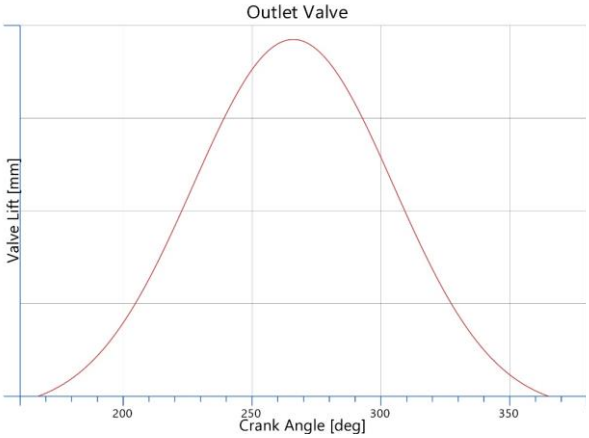

Figure 44: Valve lift table of outlet valve

11.2 Calibration

In this chapter the model is validated, and the calculated data is compared to the experimental data. For this purpose, a sufficient number of different operating points is needed. This is necessary to validate the model in a way that ensures predictability on a high level for different injection strategies.

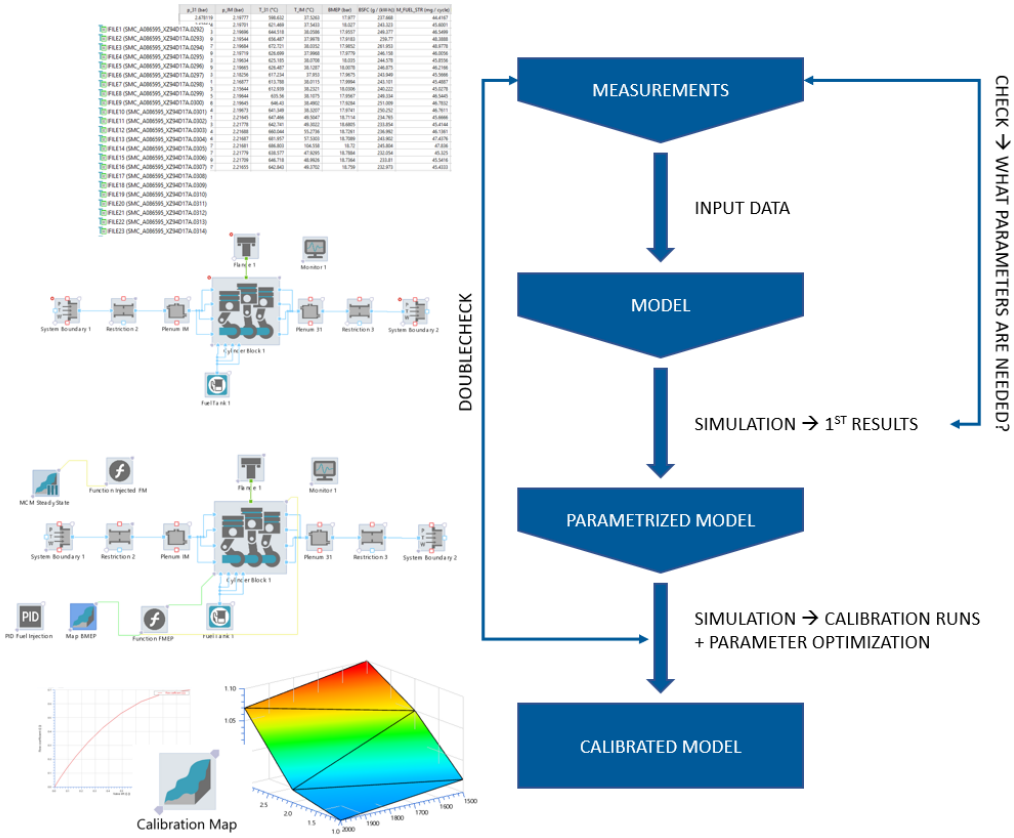

Figure 45: Reverse engineering workflow chart for calibration

Even when all data to build up a model is available it is difficult, often impossible, to establish a model from scratch which delivers satisfying solutions. In the industry it is common practise to reverse engineer simulation models to fulfil defined specifications. In Figure 45 a typical workflow chart for a calibration of a simulation model is shown. Originating from measurement data sets, a model is set up which is capable of fulfilling specified requirements and deliver requested results. When the model is set up and all demanded input data to run the simulation is transferred from the measurements or other sources, first calculations are performed. Those first results are then compared to the measurements to find weaknesses of the model and therefore deviations to the measurements. Through these learnings, parameters are chosen and integrated in the model to compensate those deviations. In the end calculations are performed for each measured operating point to adapt all calibration parameters. That way, a model is achieved which delivers for the measured operating points satisfying results and has a good predictability for arbitrary operating points.

11.2.1 Calibration Workflow

For the validation of the model to fit the physical engine in terms of performance and cylinder pressure trace, different steps are carried out. As a good starting point it is advised to calibrate the model for a correct injected fuel mass. Therefore, the fuel mass multiplier of the injector is connected to a PID controller. Whereby a proportional-integral-derivative (PID) controller pilots a process variable by comparing them to a setpoint variable. The PID controller ensures that through the

fuel mass multiplier the calculated injected fuel mass per stroke fits to the measured injected fuel mass per stroke. After calculation of all operating points, the PID controller is exchanged with a map. In this map all values from all operating points are written in a table from where the fuel multiplier is interpolated against a physical quantity (e.g. rail pressure). Through this map arbitrary operating points are possible. Figure 46 illustrates the flow multiplier, the rail pressure in bar and the number of injections. The diagram shows that with less injections the injected fuel mass has a greater deviation from the measurements. Therefore, the flow multiplier is set to higher values for only one injection, so no pilots are active in these cases.

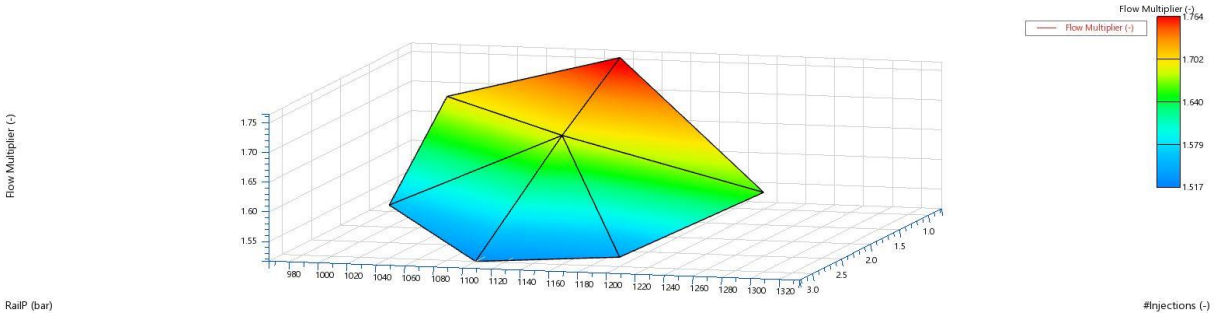

Figure 46: Calibration map for flow multiplier

To achieve an appropriate behaviour of the combustion, the parameter for the hydraulic delay is shifted to smaller values for lower rail pressure. Thus, the main injection is starting earlier and therefore also the combustion. In Figure 47, which shows the opening delay in [ms] and the rail pressure in [bar], the overall trend is visible. For lower speeds and no pilot injections, the rail pressure is also low. Therefore, the opening hydraulic delay needs to be the shortest to achieve a good combustion trace when compared to the measurements. The function of the opening hydraulic delay is described in chapter 3.2.2 Injector and illustrated in Figure 49.

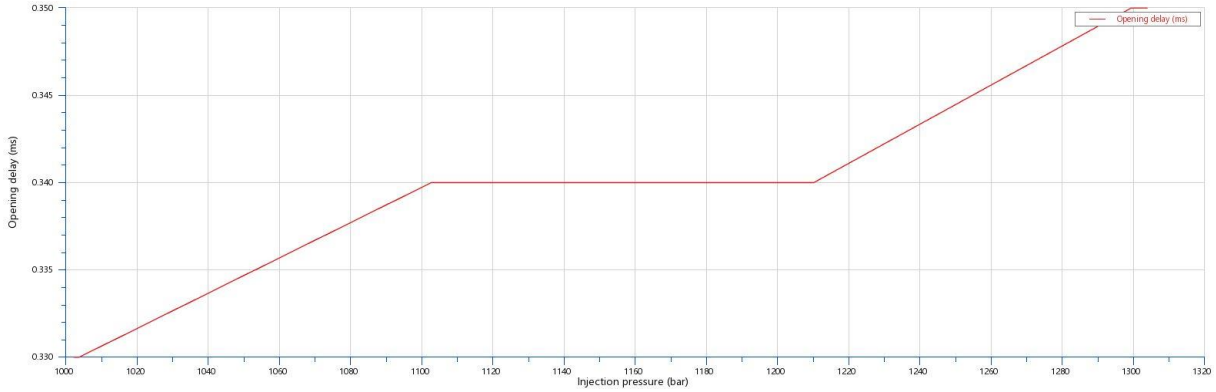

Figure 47: Calibration chart of hydraulic opening delay

To follow the cylinder pressure trace, especially for multiple injections, an additional needle lift opening parameter is introduced. The factor influences the acceleration of the mass-damping system of the injector directly, therefore more fuel is injected for the pilots. The integration of the multiplier in the mathematical framework is outlined in chapter 3.2.2 Injector in equation 3-16. Further on, the factor is illustrated in Figure 49. In Figure 48, the course of the needle lift multiplier for opening

is shown in dependency of the engine speed in [rpm], as well as the number of injections. As for one injection the values are below zero to fit the pressure gradient, the values for multiple injections are above zero to achieve a good correlation regarding the combustion trace.

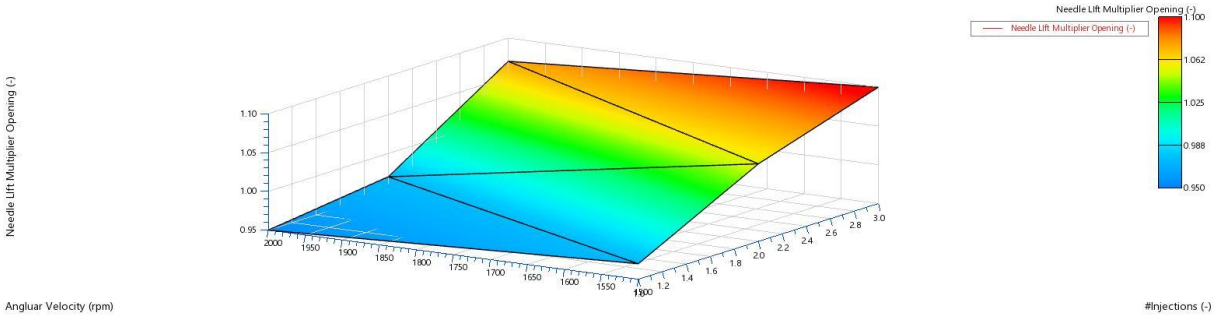

Figure 48: Calibration needle lift multiplier opening

For the combustion itself, no maps are used at all. The combustion parameters are constant across all operating points. This is done to enable a good predictability of the model.

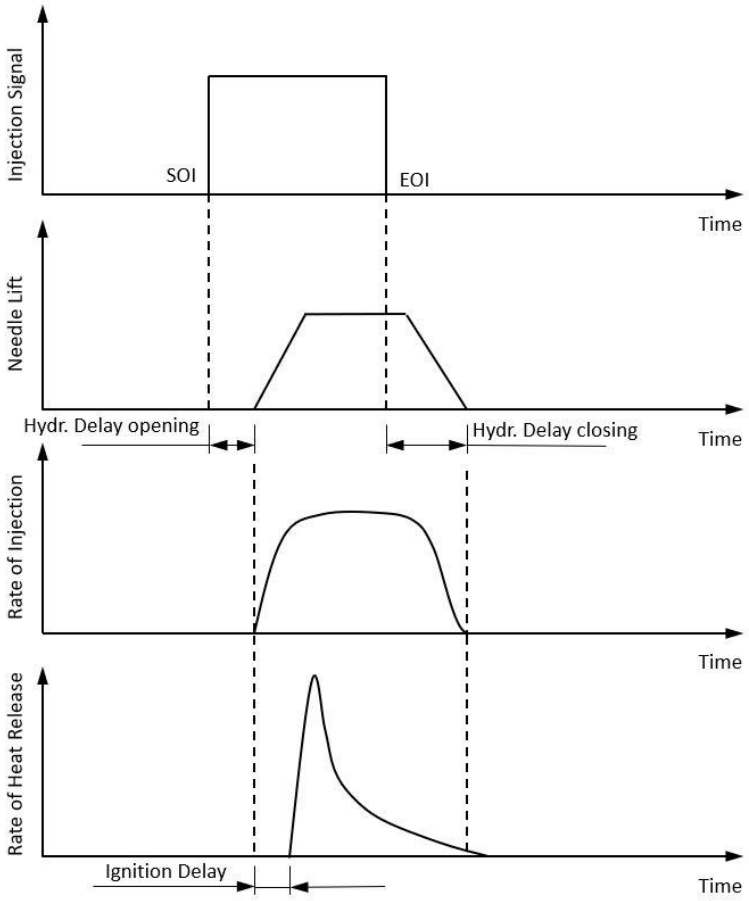

Figure 49: Injection process diagram

11.2.2 Validation with Measurements

For validation task for all operating points the combustion pressure trace is calculated and compared with the measured combustion pressure trace. In the following section details are discussed for the reference operating point IFILE 1. The calibration results for the remaining operating points are attached to 17.1 Combustion Calibration.

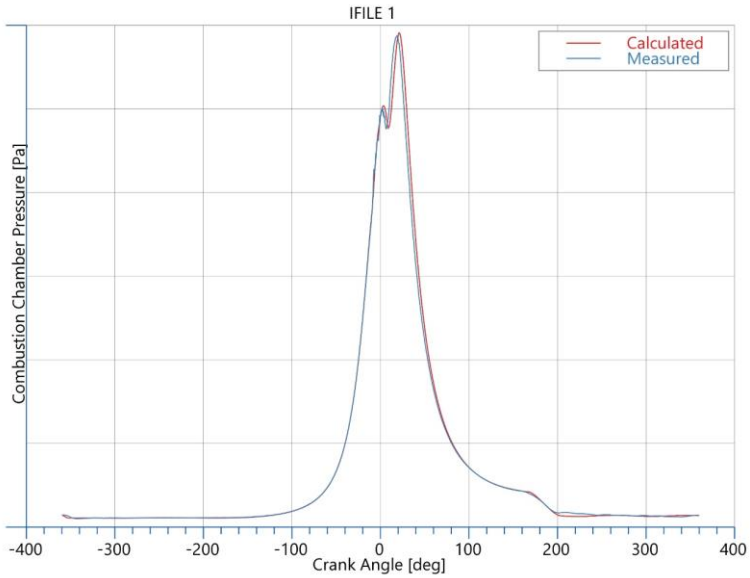

Figure 50: Validation cylinder pressure trace operating point IFILE 1

In Figure 50 the combustion chamber pressure over the crank angle is shown for both measured and calculated data for the operating point IFILE 1. To take a closer look on the pressure trace during compression and expansion phase, both operating conditions are illustrated in charts with a narrower scaling window.

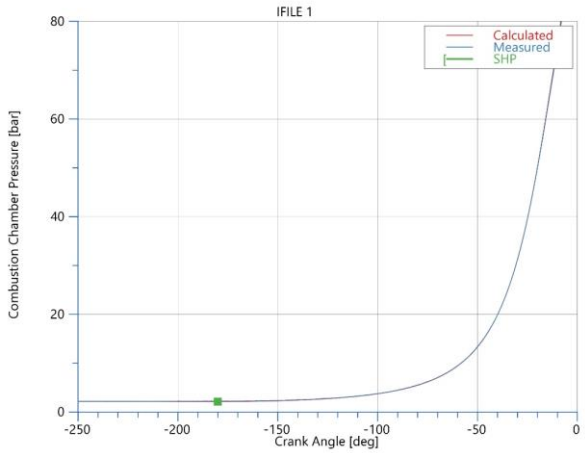

Figure 51: Pressure trace IFILE 1 compression

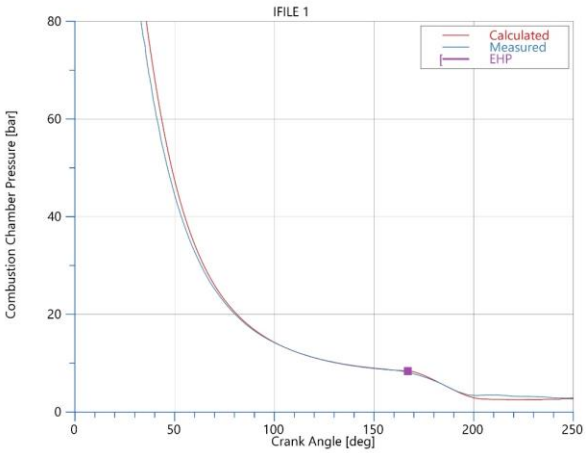

Figure 52: Pressure trace IFILE 1 expansion

As shown in Figure 51, the compression trace from measurement and calculation fit very well. The start of the compression (SHP) is for both traces identical. This point is characterized by the closing of the intake valves and corresponds to -180 degCA for the measured engine. For the expansion phase, the calculated trace is slightly shifted compared to the measured one. However, the end point of the high-pressure phase (EHP) fits again good with the measurements. According to the physical engine, EHP is set with 167 degCA for the expansion phase. The shift in the expansion face is induced by a slightly too late combustion which is pictured in Figure 53.

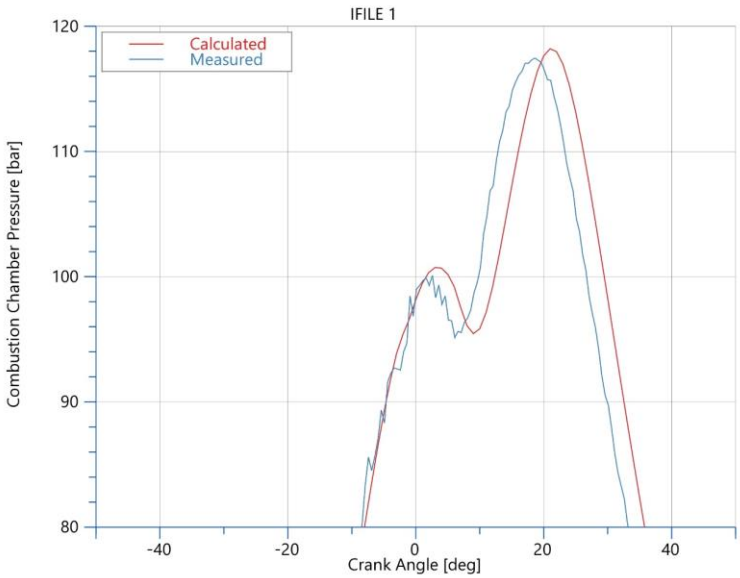

Figure 53: Pressure trace IFILE 1 combustion

As for peak firing pressure and pressure gradient the calculations match with the measurements, the overall combustion is shifted to a later phase. As illustrated the shift of combustion timing is around 2-3 degCA and therefore negligible, especially for CNI evaluation as the pressure gradients are the main reasons for combustion noise.

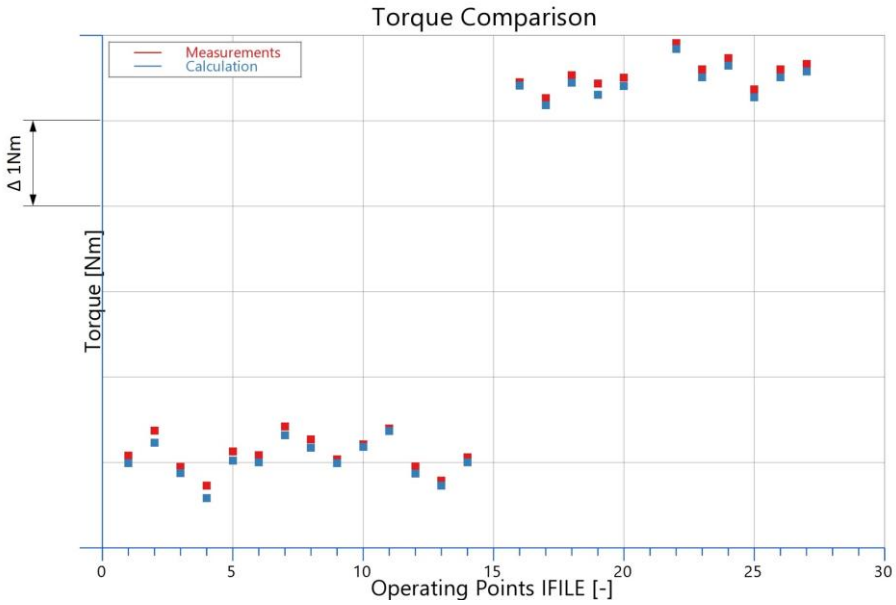

Figure 54: Torque Validation

As a last validation the delivered torque is also doublechecked with the measurements. As illustrated in Figure 54, where the torque values are shown for all measured operating points, the calculated torque is for all cases very close to the measured torque. To clarify the quality of the calibration, it is stated that the scaling for the codomain axis is 1Nm. Thus, this is an important sign that the calibration for the pressure traces as well as the calculation of the FMEP is correct. Since the area under the pressure trace is equivalent to the work which is delivered for one engine cycle. From that work the FMEP is subtracted to achieve the net work.

11.3 CNI Definition

11.3.1 Implementation

This section will cover the overall workflow performed to determine the CNI. As a first step the inputs are generated. For this task the filter points as a frequency response as well as the pressure trace for which the CNI should be calculated are read in. Then the pressure trace is converted from crank angle domain, which is the default output of Cruise™ M, since the kernel computes all cylinder correlated data in crank angle domain, to time domain. To determine the frequency response of the desired filter in the frequency domain, a cycle averaged sample rate is calculated and divided through the order of the filter. Through the obtained frequency steps, the associated amplitude values in [dB] can be linear interpolated between the given filter points. The result for one arbitrary pressure trace is pictured in Figure 55. Due to confidentiality, numerous plots in this chapter have no ordinate scaling values.

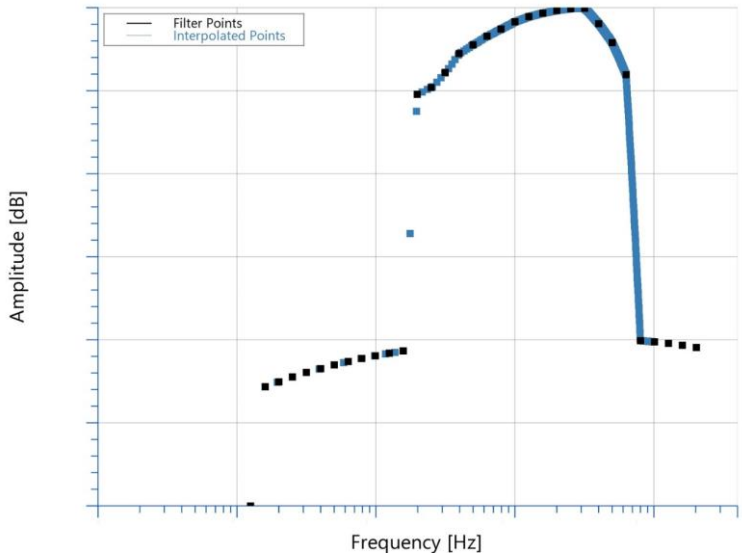

Figure 55: Interpolation points for frequency response

As a next step the pressure trace is transformed from level to amplitude, the reference pressure of the dB levels is thereby 1 Pa. The transformation is done according the law of amplitude ratios and yields when appropriate reshaped to equation 11-1.

$$p = p_{ref} \cdot 10^{\left(\frac{L_p}{20}\right)} \qquad 11\text{-}1$$

Whereas p_{ref} corresponds to the reference pressure and L_p is equal to the interpolated level values. To receive the full spectrum of the frequency response, the interpolated points are mirrored. This leads to the complete frequency spectrum of the frequency response according to Figure 56 for an arbitrary pressure trace as input.

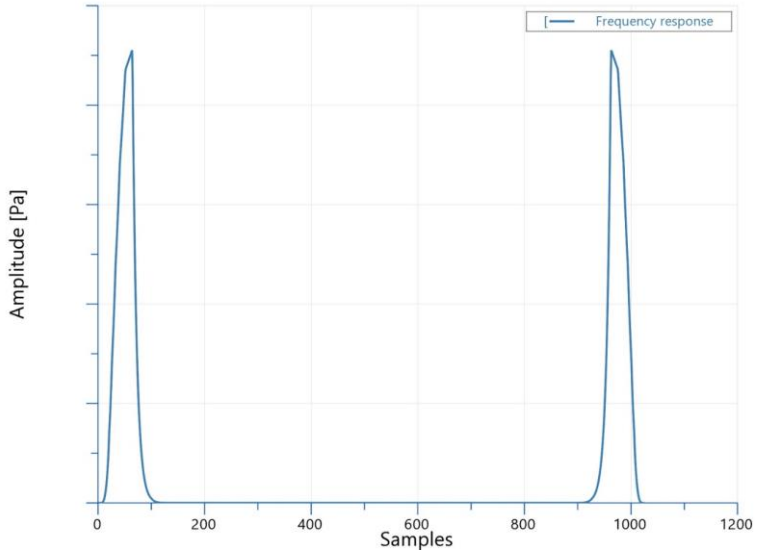

Figure 56: Full spectrum of frequency response

To generate the impulse response, the frequency response must be converted to time domain through an IFFT. As the input for the IFFT is for this method purely real, the algorithm is automatically set to real IFFT. In this case, the output is Hermitian symmetric. This manifests in an output whose negative frequency terms are conjugate complex to the positive frequency terms. After shifting the samples of the output from [513:1025] for the first half of the impulse response and from [0:512] for the other half, the impulse response is computed and illustrated in Figure 57 for a random input.

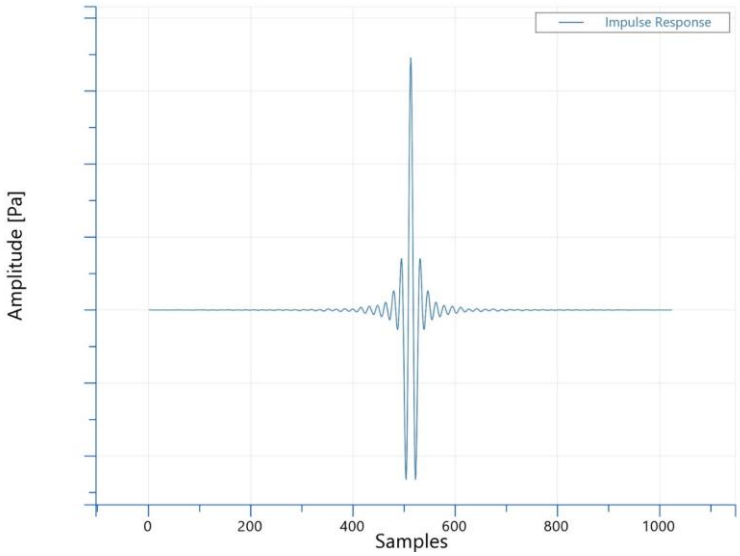

Figure 57: Impulse response

After the impulse response is computed, it is additional multiplied by a hamming window to smooth out possible boundary conditions effects. This is simply done by an appropriate weighting, as plotted in Figure 58.

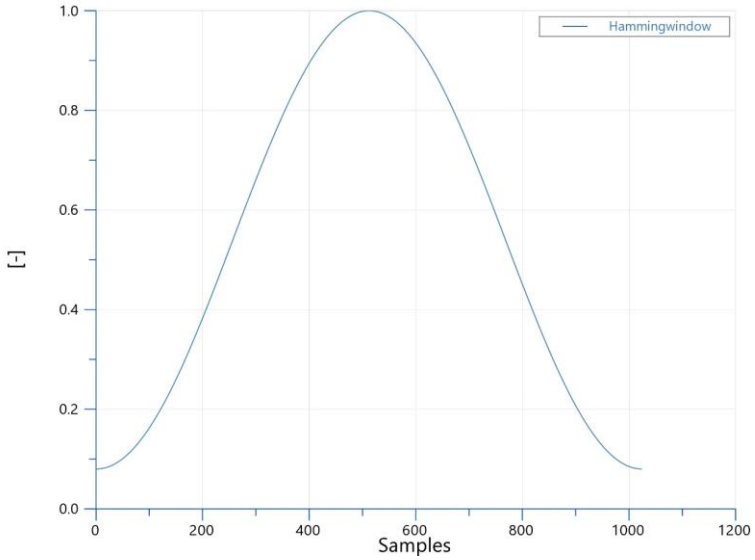

Figure 58: Weight distribution hamming window

Finally, the weighted impulse response is convolved with the input signal to compute the filtered output signal and is exemplary illustrated in Figure 59.

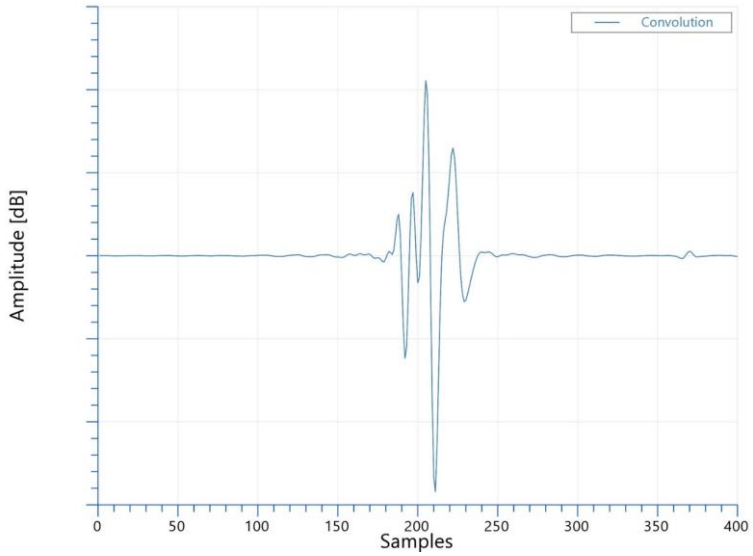

Figure 59: FIR filter output signal

From this convoluted signal finally the maximum and minimum value is determined. The CNI is then calculated through equation 11-2.

$$CNI = 3 \cdot \frac{abs(max - min)}{angvel} \qquad 11\text{-}2$$

Whereby angvel is the angular velocity of the engine in rpm. The definition of the CNI value itself was thereby developed intern. The original definition is stated in equation 11-3.

$$CNI = \frac{abs(max - min)}{angvel} \qquad 11\text{-}3$$

The compensation factor of 3 is thereby introduced due to numerical reasons. As outlined in 2.1 Injection and Its Main Control Parameters, the main cause for combustion noise is given through the change of the in cylinder pressure gradient at SOC during the premixed combustion phase. When comparing the measured pressure trace (left) and simulated pressure trace (right) in Figure 60, both represent the same operating point, it is visible that the measured pressure trace has an overall much greater change of the pressure gradient as the simulated pressure trace. The reason for this deviation is given through the formulation of the combustion algorithm described in 3.3.2 Combustion Model. As the model is not capable of covering such fluctuations or high frequency combustion dynamics, the compensation factor is introduced. The overall trends of the index are not influenced by the factor. The main purpose is to bring the simulated CNI to similar levels when compared to the measured CNI, but no direct comparison should be done between the different CNI's.

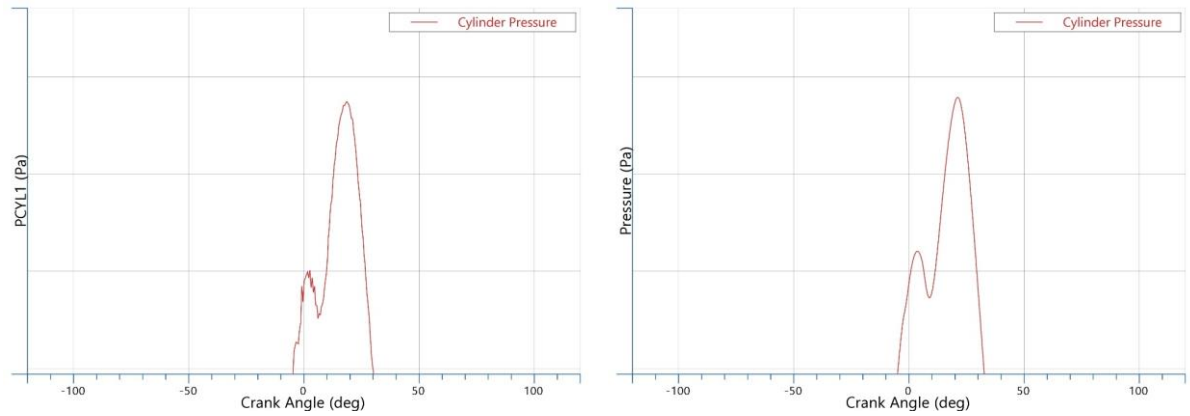

Figure 60: Comparison premixed combustion phase

11.4 CNI Evaluation on Calibrated Cylinder Pressure Traces

As first tests with above introduced CNI, the operating points with highest and lowest CNI coming from the measurements and introduced to Cruise™ M are evaluated. Therefore, the calibrated pressure traces resulting from Cruise™ M are used. For 1500 rpm lowest CNI is given at operating point IFILE1, highest at IFILE8. For 2000 rpm lowest CNI results at operating point IFILE22 and highest at IFILE25. Furthermore, low CNI engine conditions feature 3 injections, whereas high CNI engine conditions feature only 1 main injection.

Table 11: Calibrated pressure traces - CNI Levels

Case Name	CNI [-]
IFILE1	82
IFILE8	87
IFILE22	140
IFILE25	183

As higher order combustion phenomena are not considered the overall CNI levels are lower in the simulation results than in the measurements. Furthermore, as stated in 10.4 CNI Sensitivity in Measurements, the CNI reacts very sensitive to changes in the pressure gradient. Therefore, it should be used more to analyse trends as to compare fixed values of different operating points.

11.5 Assessment of Different Injection Strategies

In this chapter, various operating conditions such as injection timings, number of injections or injection pressure are investigated with respect to noise, performance and torque. For those tasks, the Cruise™ M model which was calibrated before in chapter 11.2 Calibration is used. In Table 12 the test plan for the CNI assessment is outlined. Thereby, each variable is tested separately to gain a better understanding on how each parameter influences the combustion. Whereas, Case I and Case II feature the variation of one injection parameter, Case III contains two parameter sets where for each set the variation of two parameters is investigated.

Table 12: CNI Assessment Test Plan

Case Name	Task	Operating Point	Parameter Range
Case I	Variation of Rail Pressure	IFILE 1	1000 bar - 1300 bar
Case II	Variation of SOI Pilot Injection	IFILE 7	-10 degCA – 0 degCA
Case III	Parameter Set I + II	-	-

11.5.1 Case I – Variation of Rail Pressure

For Case I the rail pressure of the injection system is varied between a range of 1000 bar to 1300 bar. The other engine parameters are thereby used from operating point IFILE 1. The operating point contains out of 3 injections at 100% load at a speed of 1500 rpm. Detailed injection timings are listed in Table 3: Injection variation timings for combustion calibration.

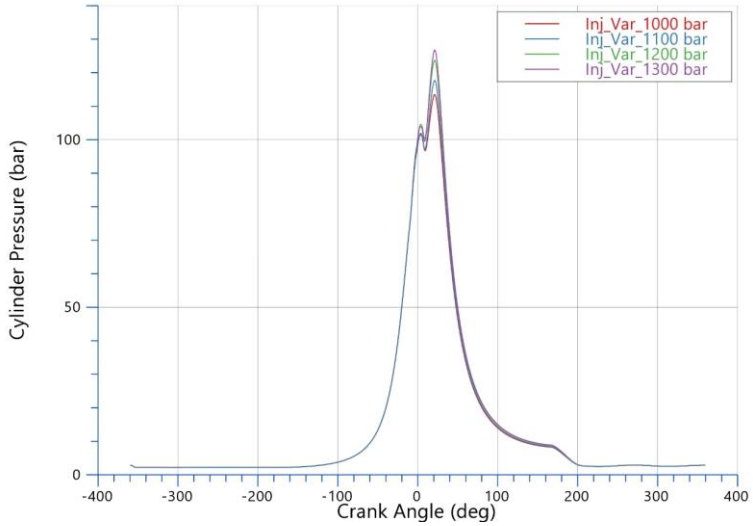

Figure 61: Case I - combustion chamber pressure

With increasing rail pressure, the combustion chamber peak pressure reaches higher levels. Also, the rate of pressure rise is affected. As the change of gradient of the combustion chamber pressure is the dominant source of CNI, the trace of pressure rise is illustrated in Figure 62. Which is basically the derivation of the pressure trace after the crank angle. Thereby, it is evident, that a higher overall pressure rise is achieved, both for positive and negative turnover, for higher injection pressures. The physical background for this behaviour is described by Khaira et al. [3], stating an increase of fuel atomization by the injection system with increasing injection pressures. Thus, the premixed combustion flame is enhanced, resulting in higher combustion chamber peak pressure and a higher pressure raise. In the simulation task, the pipe pressure is influencing the injection model at two points. First one is through the fuel mass flow, which is stated by equation 3-15. Second one occurs through the opening velocity of the needle, which is a physically correct approach, as the injector needle is in real life application also controlled by the pipe pressure. The mathematical context is thereby described by equation 3-16. Hence, an increase in rail pressure leads to an enhanced fuel mass flow by the injection system, increasing the spray cone.

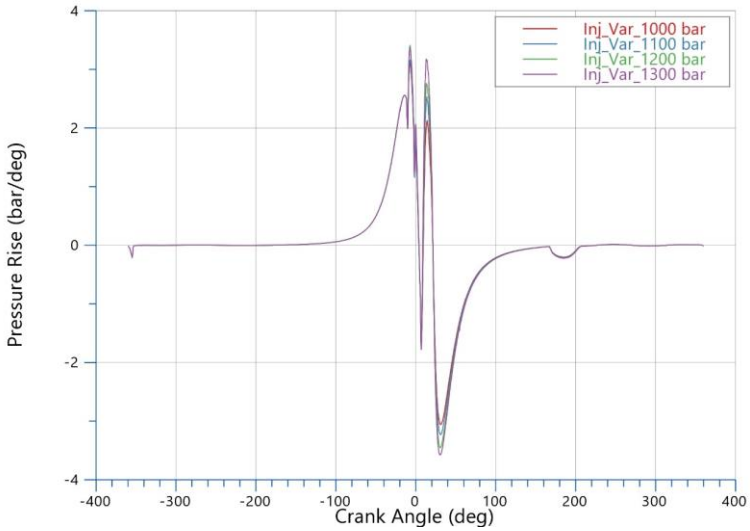

Figure 62: Case I - combustion chamber pressure rise

In the combustion model the increased rail pressure (with an increase in fuel mass flow) has an impact on the determination of the heat realized in the premixed combustion phase. Thereby, the calculation for heat released in the premixed combustion phase of equation 3-42, is mainly influenced by the amount of fuel available at start of combustion (SOC) which has ignition temperature. As stated before, for higher rail pressures, the injection system delivers more fuel. Thus, more fuel is also available at ignition temperature at SOC. In Figure 63 the fuel mass burned in the premixed combustion phase is shown. The increase of fuel burned in the premixed combustion phase is thereby directly linked to the rise of rail pressure in the injection system.

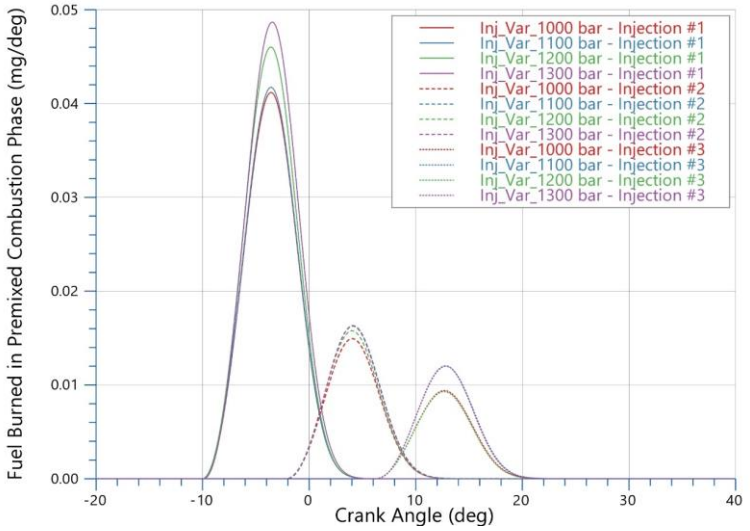

Figure 63: Case I - fuel burned in premixed combustion phase

The mathematic context for the determination of the heat released in the premixed combustion phase is thereby given by equation 3-43. The output of equation 3-43 is depicted in Figure 64 as ROHR over degree crank angle.

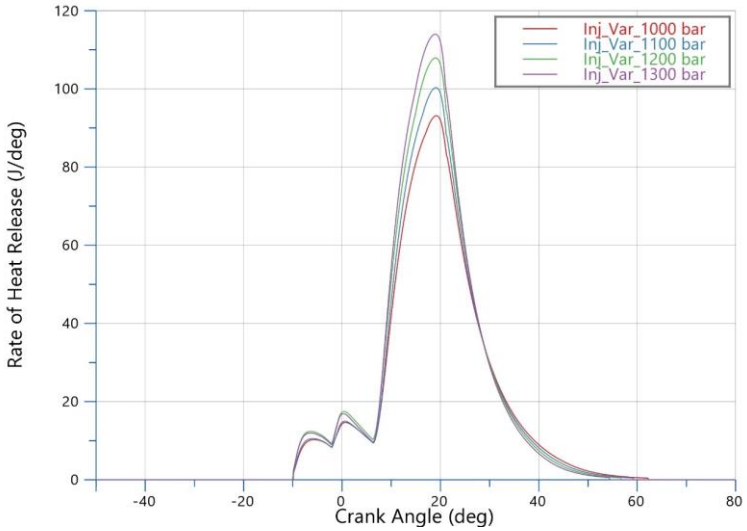

Figure 64: Case I - ROHR

As more fuel is available at ignition temperature for SOC, the ROHR delivers higher levels for each injection.
Those effects have of course an impact on the determined CNI levels which are evaluated for each run and listed in Table 13. As the lowest rail pressure leads to the smallest premixed combustion flame, the associated CNI level has also its minimum at the run Var1.

Table 13: Case I - CNI Levels

Run Name	Injection Pressure [bar]	CNI – Level [-]
Var1	1000	83
Var2	1100	91
Var3	1200	104
Var4	1300	110

In Figure 65, the cylinder pressure is illustrated over the piston displacement volume. As outlined in the section above, higher rail pressures results in higher pressures in the cylinder. This is evident in Figure 65, where the indicated cylinder pressure rises also. From the indicator diagram the indicated medium pressure can be extracted, which corresponds to the medium height of the area created by the pressure trace. This parameter is called medium indicated pressure, which can be understood as a constant pressure over one engine work cycle. The area of the indicator diagram correlates thereby to the work which is either delivered by the crank train (work cycle) or consumed by the crank train (gas exchanged), when friction is neglected.

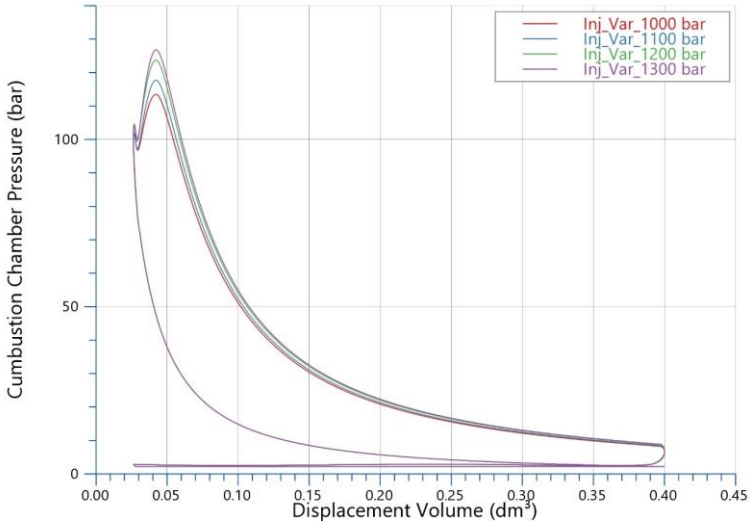

Figure 65: Case I - indicator diagram

In Figure 66, the indicated torque over on engine cycle is shown. Thereby, the area under the trace of the indicated torque can be split into a positive as well as a negative sum. The negative sum correlates to the torque necessary to aspirate the engine, whereas the positive torque corresponds to the torque delivered by the engine over one cycle. Those areas correlate thereby to the correlations outlined in Figure 65. Thus, the negative sum of the torque is equal to the negative work in the load change loop, and the positive torque equals to the positive work loop. Thus, the work delivered by the engine corresponds to the size of the area restricted by the cylinder pressure in the indicator diagram. For higher pressures the torque given off by the engine correlates thereby linear to the size of the area.

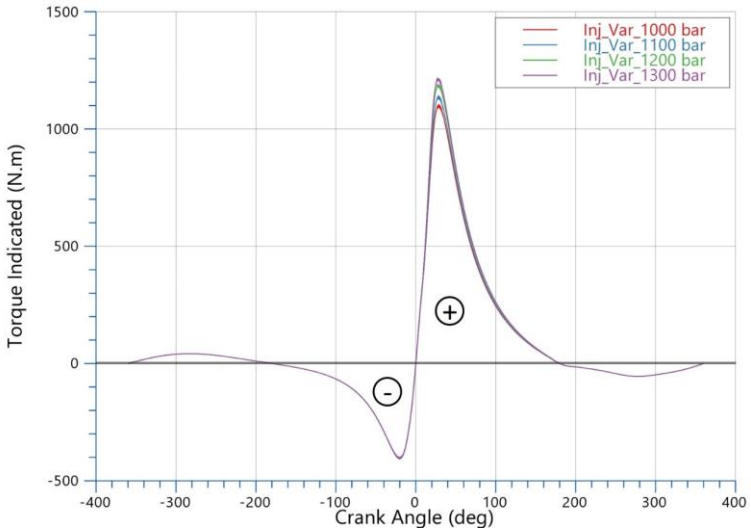

Figure 66: Case I - indicated torque

11.5.2 Case II – Variation of SOI of Pilot Injection

In Case II one pilot injection is introduced to the main injection. Thereby, the amount of injected fuel is small compared to the amount injected during the main injection. Four cases are simulated, covering a range of -10 degCA to 0 degCA for the pilot injection. The last case functions thereby as a reference case where no pilot injection is applied at all. Additional injection data is listed in Table 14. The remaining engine conditions are thereby obtained from operating point IFILE 7 at 1500rpm and 100% load.

Table 14: Case II - injection data

Case Name	SOI Main [degCA]	Duration Main [degCA]	SOI Pilot [degCA]	Duration Pilot [degCA]
Inj˙Var˙SP˙-10degCA	2.5	8.5	-10	1.5
Inj˙Var˙SP˙-5degCA	2.5	8.5	-5	1.5
Inj˙Var˙SP˙0degCA	2.5	8.5	0	1.5
Inj˙Var˙SP˙woPilot	2.5	8.5	-	-

In Figure 67 the pressure traces for the injection sweep listed in Table 14 is pictured. Thereby, it is evident that the injection timing of the pilot influences the overall shape of the pressure trace heavily. Whereby an early pilot, leads to a dominant peak before the main combustion. Whereas a late pilot which is set close the main injection, damps the sudden rise of pressure and temperature initiated by the main injection.

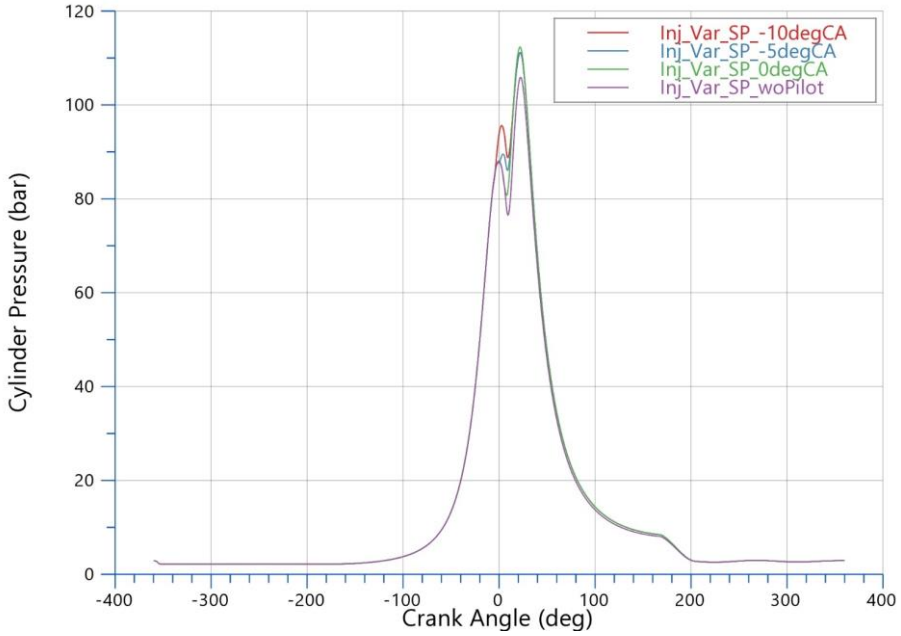

Figure 67: Case II - combustion chamber pressure

This is clear for cases where the pilot is set for -10 degCA, respecitivley-5 degCA, as additional turning points are introduced in the pressure trace. For further analysis between case 0 degCA and without pilot injection, Figure 68 is introduced. Thereby a cut out of the pressure trace between -

6 degCA and 30 degCA is illustrated. For the case without pilot (dotted line), and the case with one pilot very close to the main injection (dashed line), the tangents on the pressure trace besides the turning points are marked. The angle α is thereby with 75 deg smaller than the angle β with 87 deg. Thus, the pressure trace for the case 0 degCA manifests in a smaller pressure gradient and therefore in lower CNI compared to the case without a pilot injection.

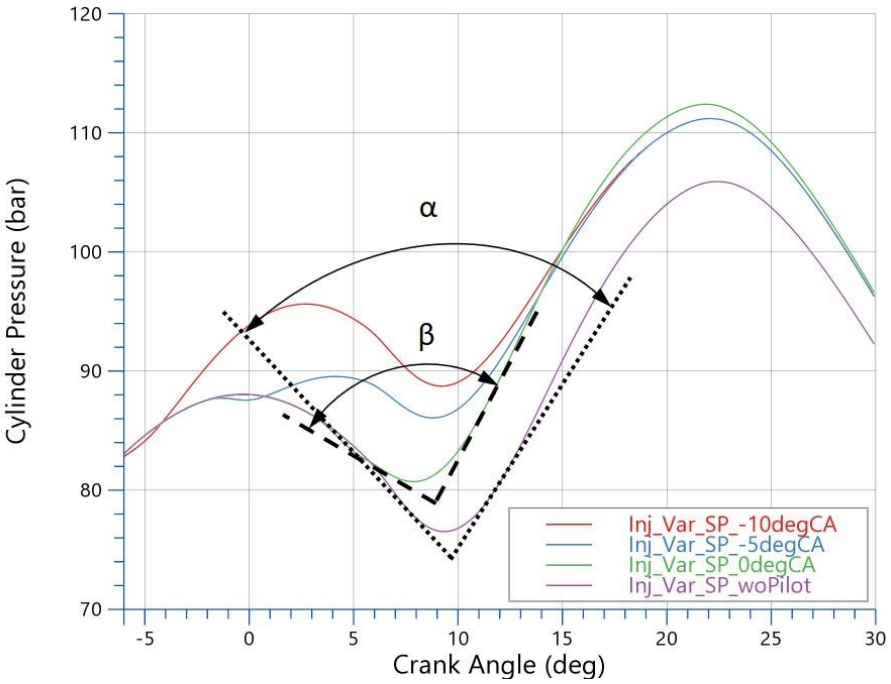

Figure 68: Case II - combustion chamber pressure cut out

This behaviour is clearer when looking at the pressure rise of the combustion chamber, illustrated in Figure 69, and the temperature trace of the combustion, depicted in Figure 70. As for early pilot injection timings, the pressure rise trace shows distinct bends, the pilot injection close to the main injection features just one bend which reduces the change of pressure gradient of the main injection significantly. The same situation can also be seen when looking at the temperature trace in Figure 70. Through the temperature rise of the pilot injection, the sudden temperature increase of the main injection can be reduced.

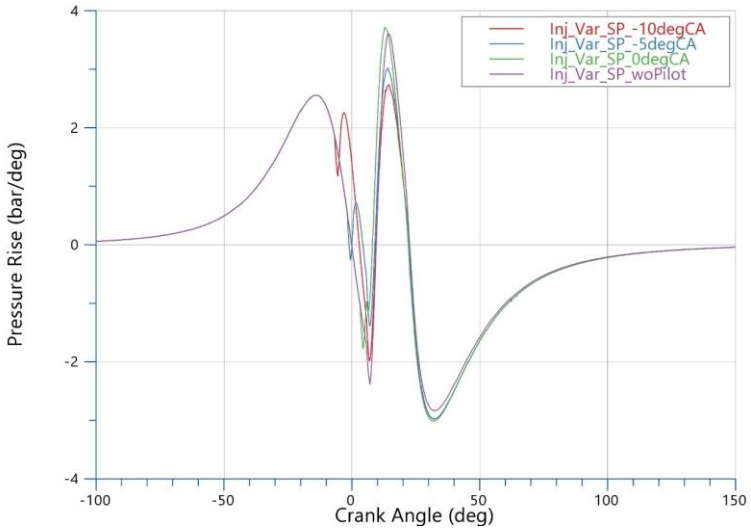

Figure 69: Case II - combustion chamber pressure rise

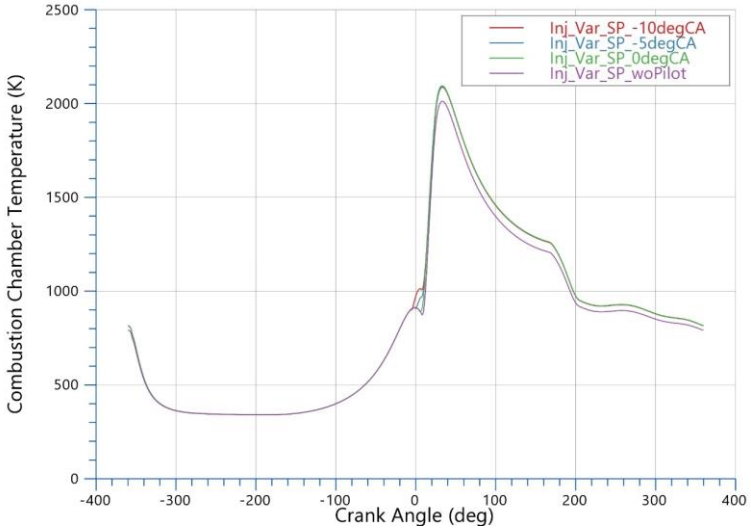

Figure 70: Case II - combustion chamber temperature

The impact of the different injection strategies is shown in Table 15. The lowest CNI level can thereby be found at 0 degCA for the pilot injection. As described before, according to Thiam et al. [26] and Shin et al. [1], due to a rise of pressure and temperature introduced by the pilot combustion right before start of combustion of the main injection, the impact of the premixed combustion flame triggered by the main injection is damped. Thus, the change of pressure gradient is lower and the CNI level can be reduced to a much lower level compared to the reference case without a pilot injection. Vice versa, the CNI level can also be much worse when compared to the reference case. As shown for -5 degCA for the pilot injection, an additional peak is introduced in the cylinder pressure trace between TDC and main combustion. Through the additional bends in the pressure trace and pressure rise, a much higher noise is thereby emitted by the combustion. As combustion noise is according to Khaira et al. [3] at a frequency range between 200 Hz and 6000 Hz, the overall structure gets excited through sudden changes of the pressure in the combustion chamber.

Table 15: Case II - CNI Levels

Case Name	SOI Pilot [degCA]	CNI Level [-]
Inj_Var_SP_-10degCA	-10	87
Inj_Var_SP_-5degCA	-5	96
Inj_Var_SP_0degCA	0	59
Inj_Var_SP_woPilot	-	82

For the very early injection at -10 degCA the pressure rise is very strong due to a higher premixed combustion flame. This is verified through the amount of fuel burned in the premixed combustion phase, pictured in Figure 71. -5 degCA as well as 0 degCA have only a minor difference in the fuel amount burned in the premixed combustion phase. The reason for this is an overall lower change of pressure and temperature in the combustion chamber around TDC.

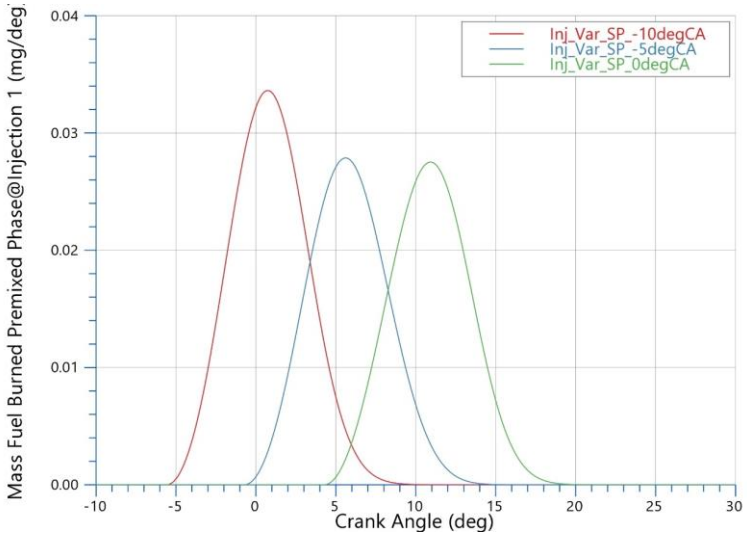

Figure 71: Case II - fuel burned in premixed combustion phase

In Figure 72 the impact of the injection strategy on the ROHR is illustrated. As for the early case at -10 degCA the pilot combustion starts also very early compared to the main combustion, the trace of ROHR includes a sharp bend between pilot and main combustion. The smoothest transition between pilot and main combustion is given by the 0 degCA pilot injection.

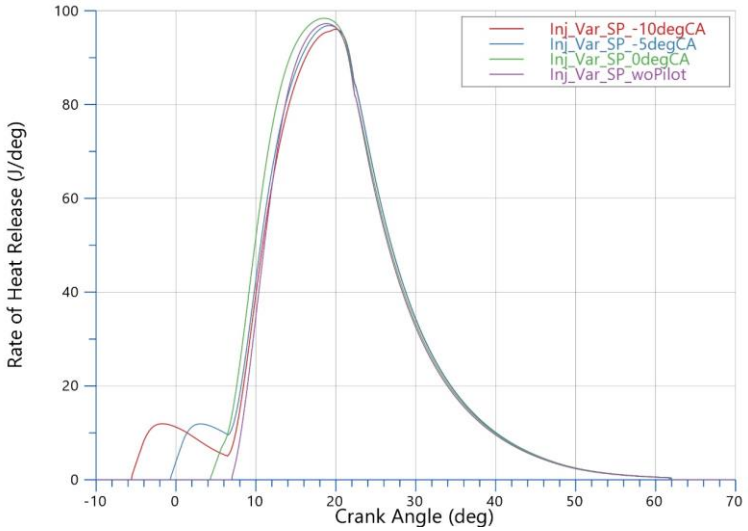

Figure 72: Case II - ROHR

In terms of indicated work and torque over one cycle, the differences between the cases with pilot injection are rather small, as the most fuel amount is injected through the main injection after TDC. The difference between cases with pilot and the reference case is thereby obtained through the additional amount of fuel injected by the pilot. Results for indicated work and torque are shown in Figure 73 and Figure 74.

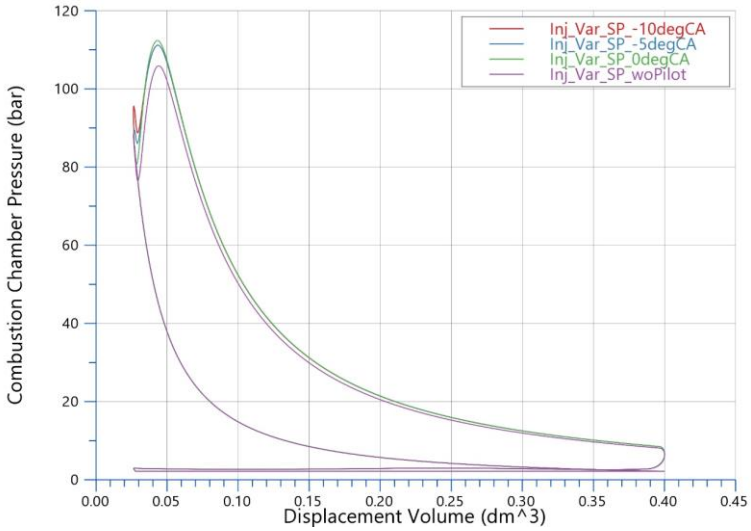

Figure 73: Case II - indicator diagram

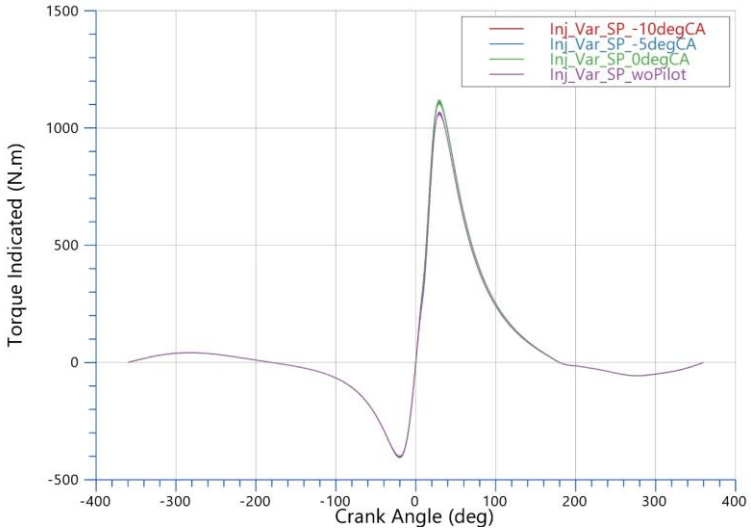

Figure 74: Case II - indicated torque

11.5.3 Case III – Variation of Parameter Sets

As for case I and case II, only one parameter at a time is varied, for case III parameter sets are created, to achieve a better understanding for the interaction between individual parameters. Thereby, two individual parameters at once are selected and varied against each other to find optimal operating conditions as a trade-off relation relating to CNI, fuel consumption, efficiency and performance. Both parameter sets are building up on operating point IFILE 7.

Table 16: Parameter Set I

Parameter	Range
SOI Pilot	-10 degCA – 0 degCA
Duration Pilot	1 degCA – 5 degCA

Table 17: Parameter Set II

Parameter	Range
SOI Pilot	-10 degCA – 0 degCA
Rail Pressure	1000 bar – 1700 bar

Parameter Set I

For this set operating point IFILE 7 is selected. The injection timing of the pilot is thereby modified to cover a range between -10 and 0 degCA for start of injection (SOI), as well as 1 degCA -5 degCA variation regarding the injection duration. The main injection is thereby kept at 2.5 degCA for SOI and 8.5 degCA for duration. To constitute the trade-off relationship between the above-mentioned parameters, surface plots are used.

In Figure 75, the CNI levels over the parameter range are plotted. The highest CNI level of 153 is thereby located at -5 degCA and a duration of 3 degCA for the pilot injection. The lowest CNI of 68 is obtained for a pilot injection at 0 degCA with a duration of 2 degCA. As outlined in 11.5.2 Case II – Variation of SOI of Pilot Injection, a small pilot injection close to the main, can rise the temperature level in the cylinder in a way, that the premixed combustion of the main injection is weakened down to lower levels. With such strategy the overall engine noise behaviour can be lowered significantly.

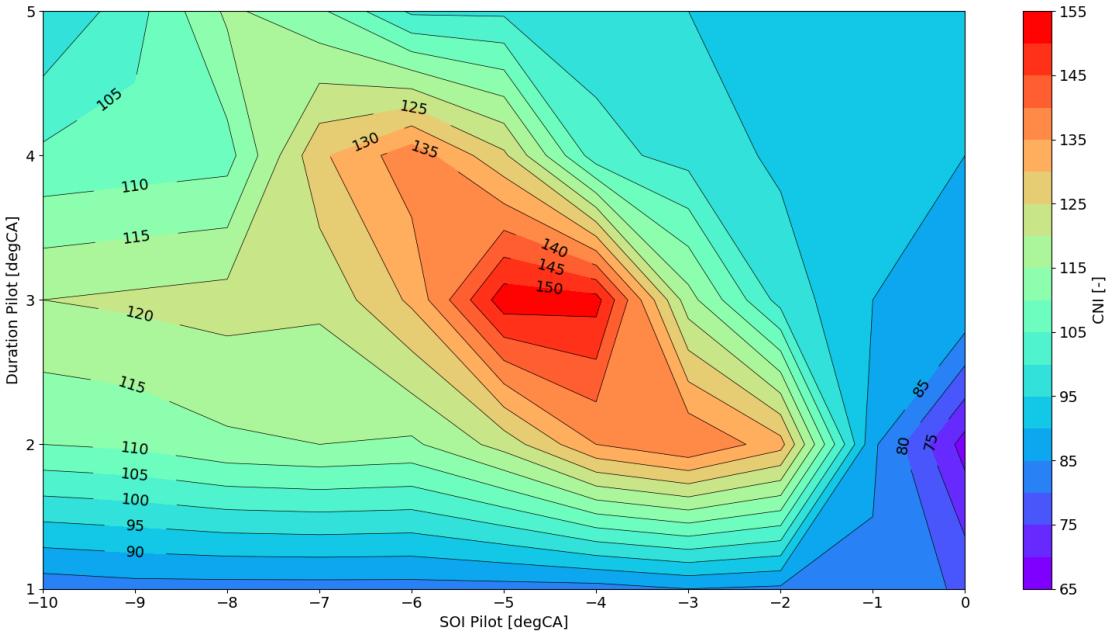

Figure 75: Parameter Set I - CNI

The approach of CNI can be clarified when evaluate the peak cylinder pressure for the parameter set I. The results are outlined in Figure 76.

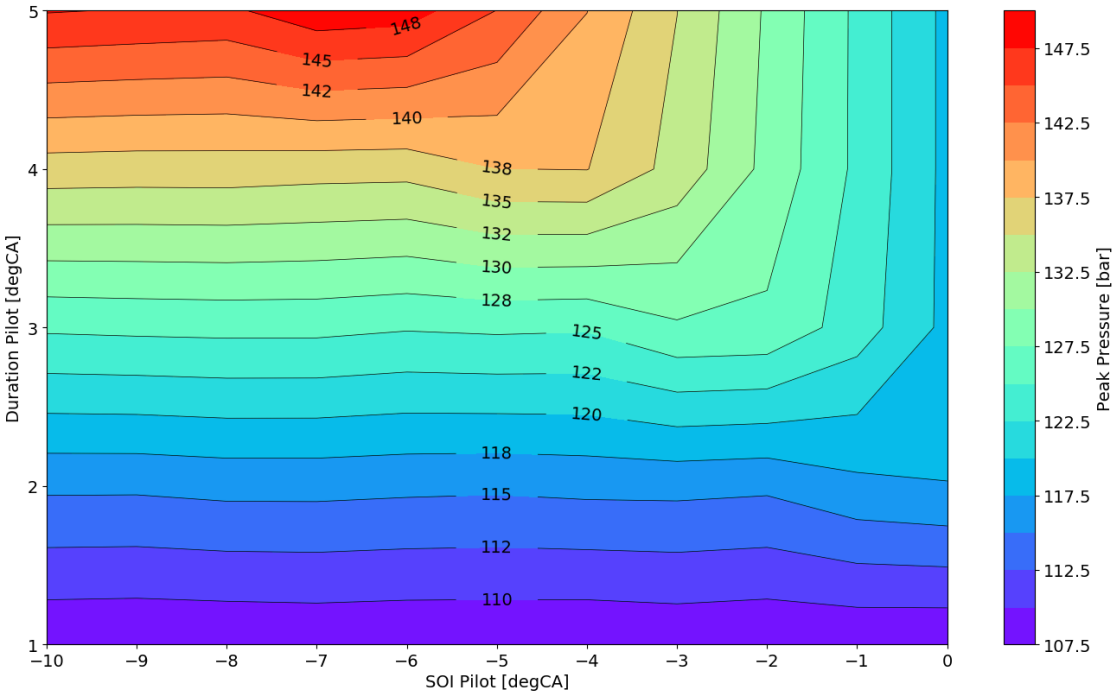

Figure 76: Parameter Set I - peak cylinder pressure

When comparing Figure 75 and Figure 76, it is evident that areas with high CNI don't correlate with areas of high cylinder peak pressure. This is induced due to the reason the CNI index rates the frequencies induced by combustion according to the human sense of hearing. Instead, it is decisive how the rate of pressure gradient is realized. As the rate of gradient excites the frequency bands responsible for combustion. This circumstance is outlined when comparing the pressure trace for the minimum as well as maximum CNI in Figure 77.

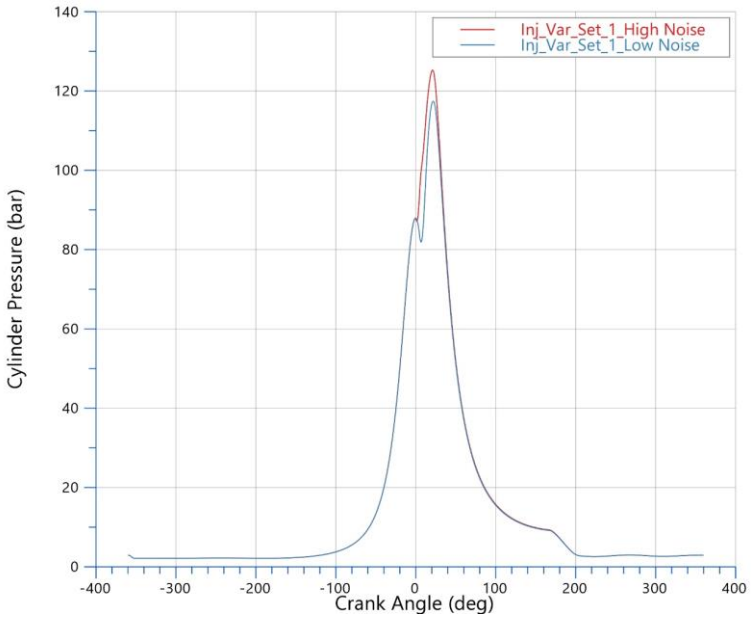

Figure 77: Parameter Set I - high/low CNI pressure trace

As the difference in peak pressure is small with around 117 bar respectively 125 bar, when comparing to the entire range of the parameter variation, which is evaluated from 107 bar to 149 bar. However, the noise is not entirely defined by the peak pressure, but rather by the pressure levels in the relevant frequency bands between 200 Hz – 6000 Hz, which is illustrated in Figure 78.

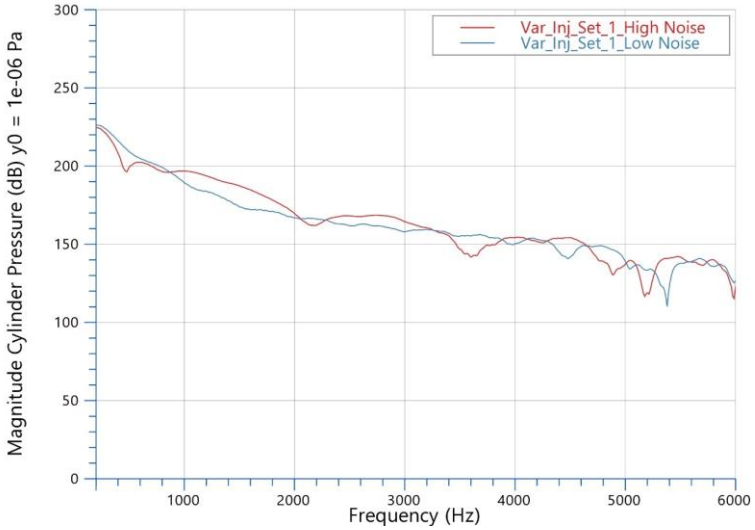

Figure 78: Parameter Set I - FFT high/low CNI pressure trace

The evaluation for indicated mean effective pressure (IMEP) and fuel consumption is plotted in Figure 79 and Figure 80. For both parameters are same trends evident. As fuel consumption relates directly to the duration of the pilot, high values for fuel consumption are located at the area responsible for longer injection timings in the surface plot.

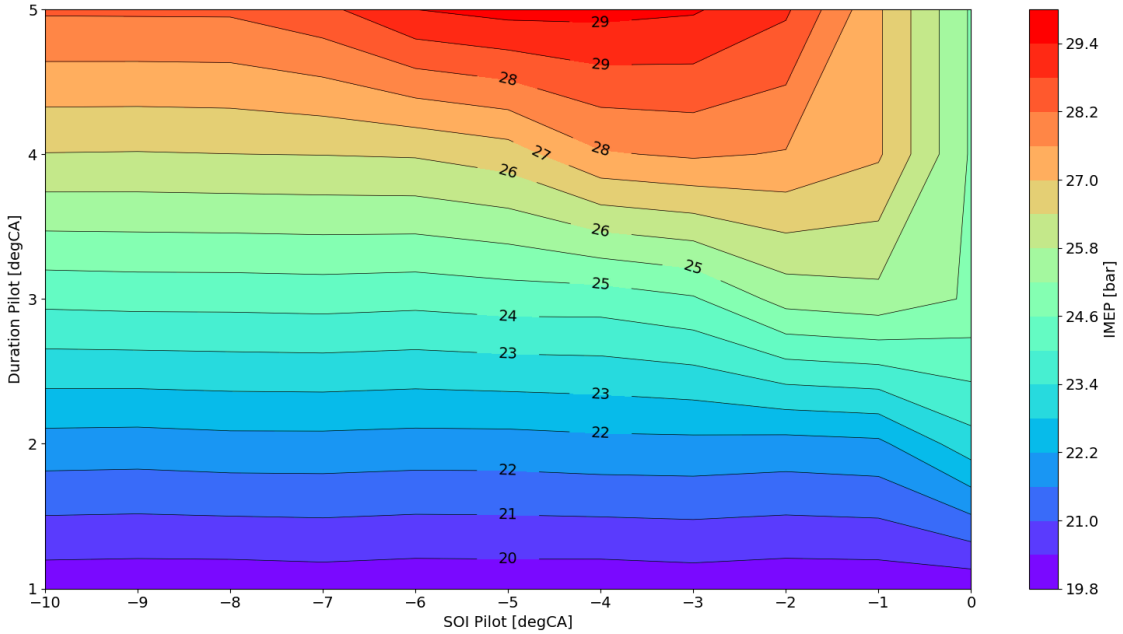

Figure 79: Parameter Set I - IMEP

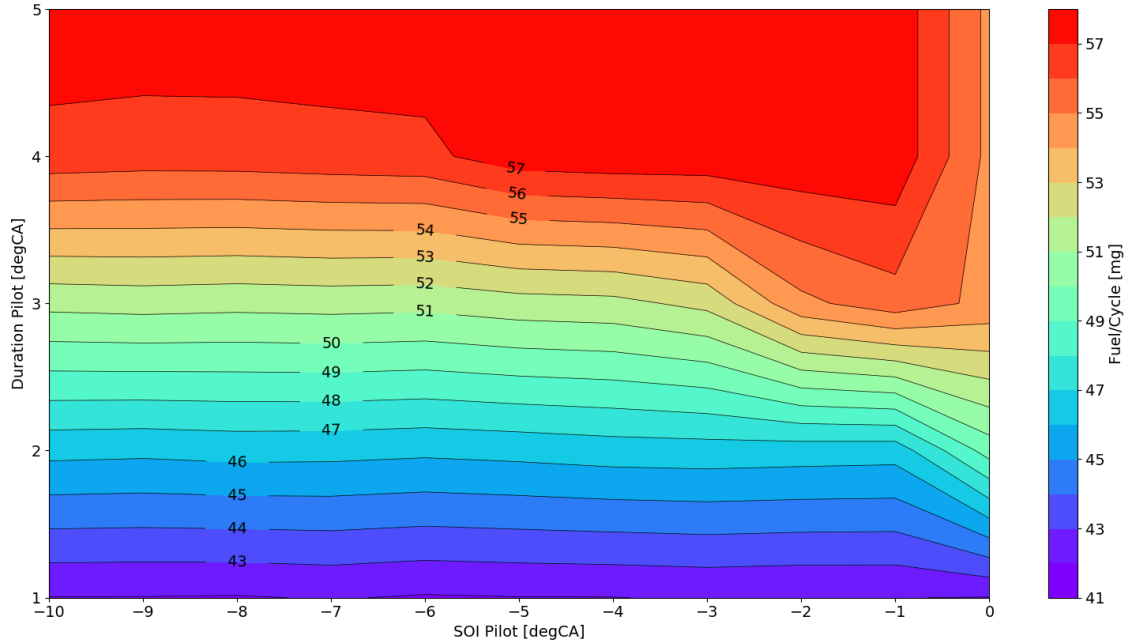

Figure 80: Parameter Set I - fuel/cycle

For IMEP the value range varies from 19.9 bar to 29.6 bar. The range of values for fuel consumption extends thereby from 41.9 mg/cycle to 57.7 mg/cycle. Which means, for an increase of fuel

consumption by 37.7 %, an increase in IMEP by 48,4 % can be achieved. However, for this operating point CNI levels are worse compared to CNI optimized operating points. But with an evaluated CNI value of 97 still on the lower side of the range. This operating point covers also the area of maximum indicated efficiency for the selected parameter range. For the entire parameter range, the indicated efficiency is evaluated and illustrated in Figure 81. Lowest indicated efficiency can be found for medium and higher injection durations shortly before the main injection at -1 degCA to 0 degCA.

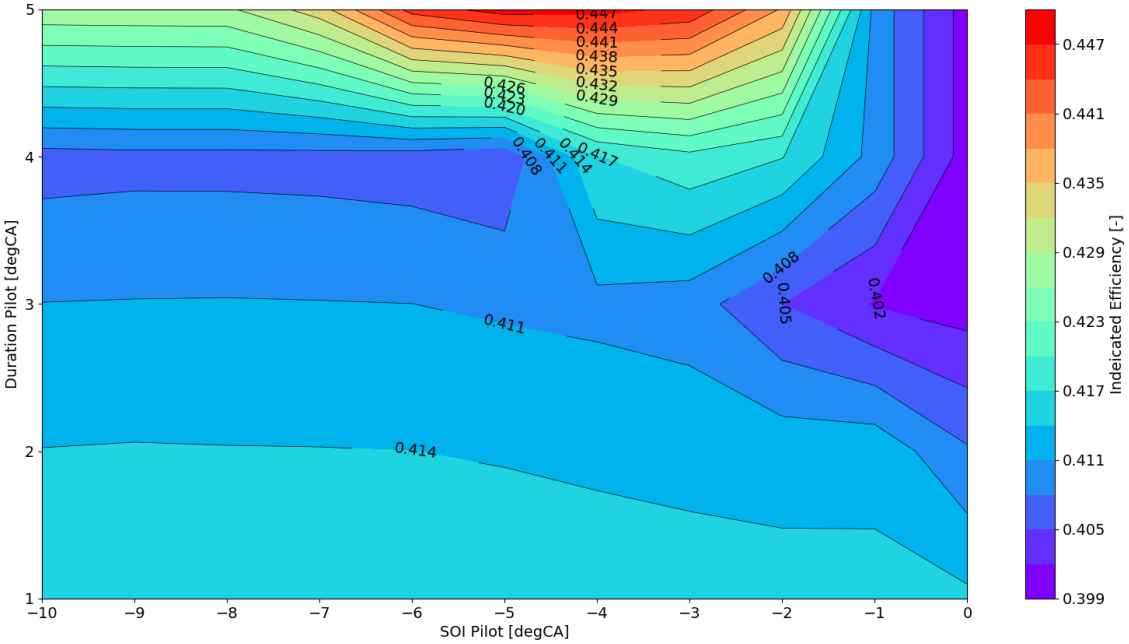

Figure 81: Parameter Set I - indicated efficiency

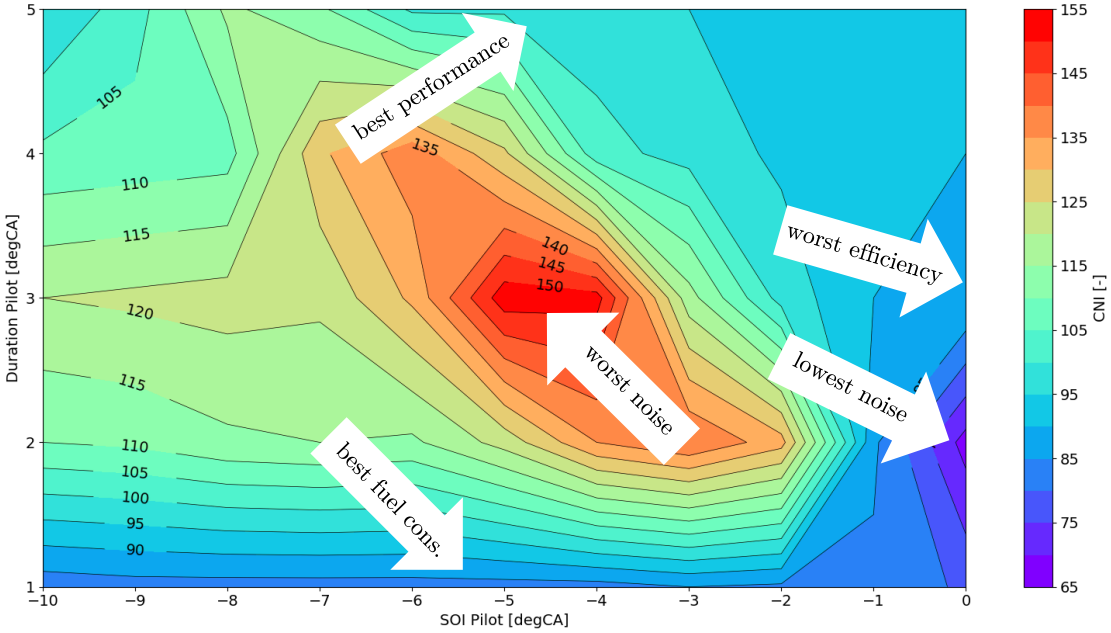

Figure 82: Parameter Set I - evaluation of distinctive parameters over CNI

In Figure 82 the overall trade-off relationship between one parameter set is illustrated. As a general conclusion can be said, that for certain engine operation conditions one distinctive injection strategy has to be set. Thus, high performance compared with low noise and minimum fuel consumption cannot be realized at once.

Parameter Set II

For parameter set II, the optimal pilot duration for minimum noise, particularly 3 degCA, evaluated in parameter set I, is set. For parameter variation the SOI for pilot is set between -10 degCA and 0 degCA according to parameter set I. Further, the rail pressure is varied between 1000 bar and 1700 bar. The other operating parameters are thereby selected from operating point IFILE 7.

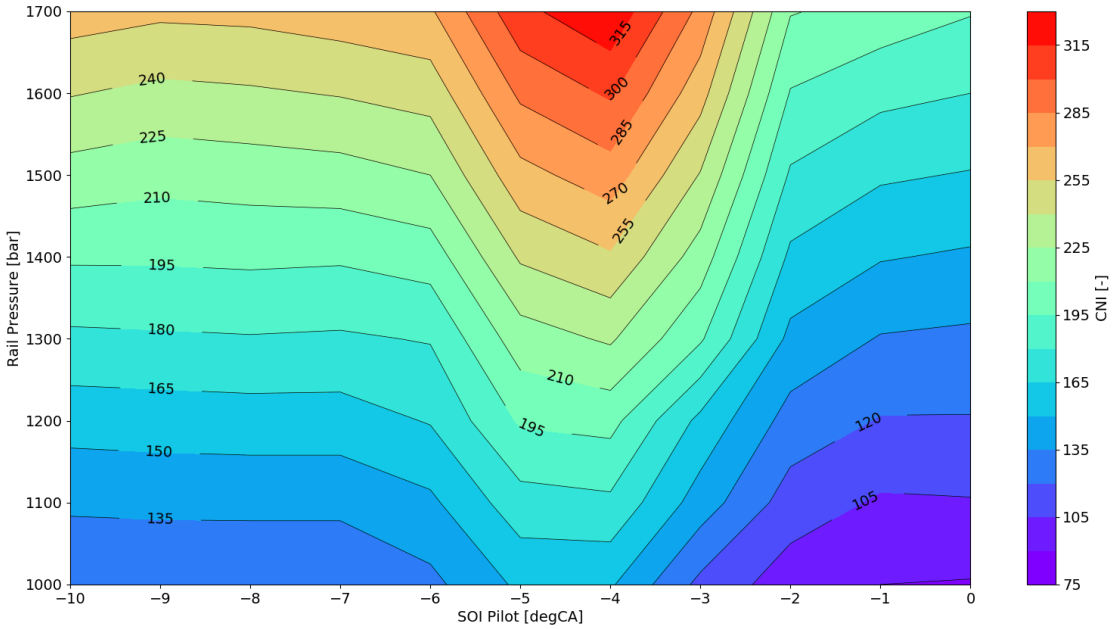

Figure 83: Parameter Set II - CNI

In Figure 83 the CNI for parameter set II is plotted. The lowest CNI area is thereby located at 0 degCA for 1000 bar, which covers with the area investigated in Figure 75. For higher rail pressure levels, CNI increases as well. Highest CNI levels are located between -4 degCA and -5 degCA for maximum rail pressure. Whereby SOI of pilot is investigated in parameter set I. For IMEP, illustrated in Figure 84, the value range reaches from 24.1 bar to 32.1 bar. This corresponds to an increase of 33.1 %. On the other hand, fuel consumption reaches from 51.2 mg/cycle up to 57.7 mg/cycle, which is equal to a rise of only 12.8 %. The evaluation for fuel consumption is presented in Figure 85. Hence, an improvement in performance of 33.1 %, is with increasing rail pressures achieved, by an increase of fuel consumption by only 12.8 %. Thus, the trade-off relationship between noise, performance and fuel consumption is always present, and for multiple engine operating objectives compromises are indispensable.

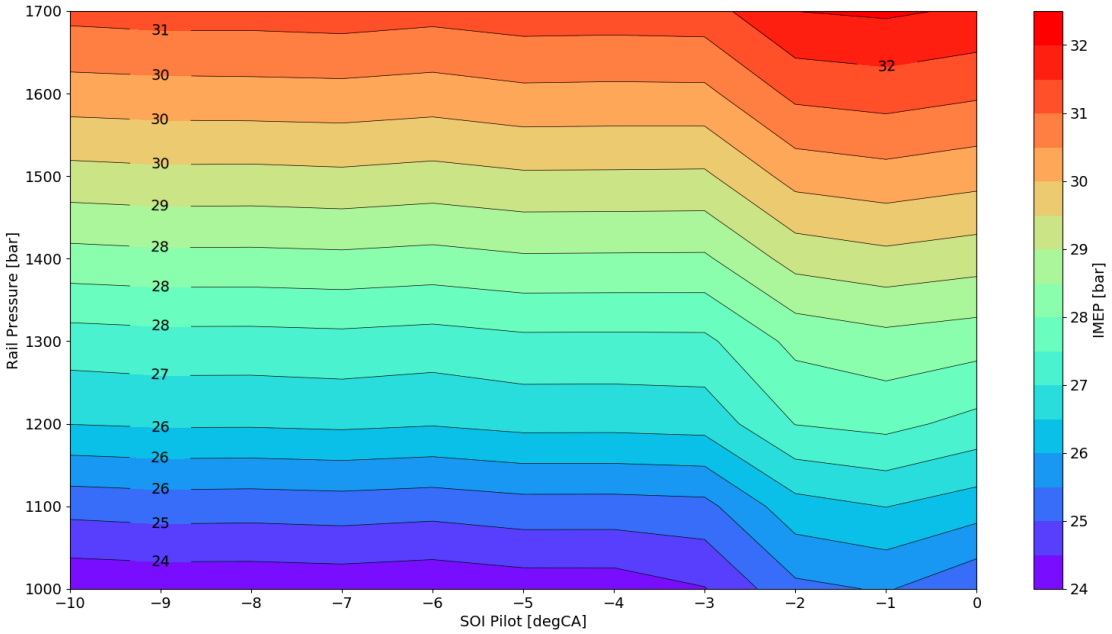

Figure 84: Parameter Set II - IMEP

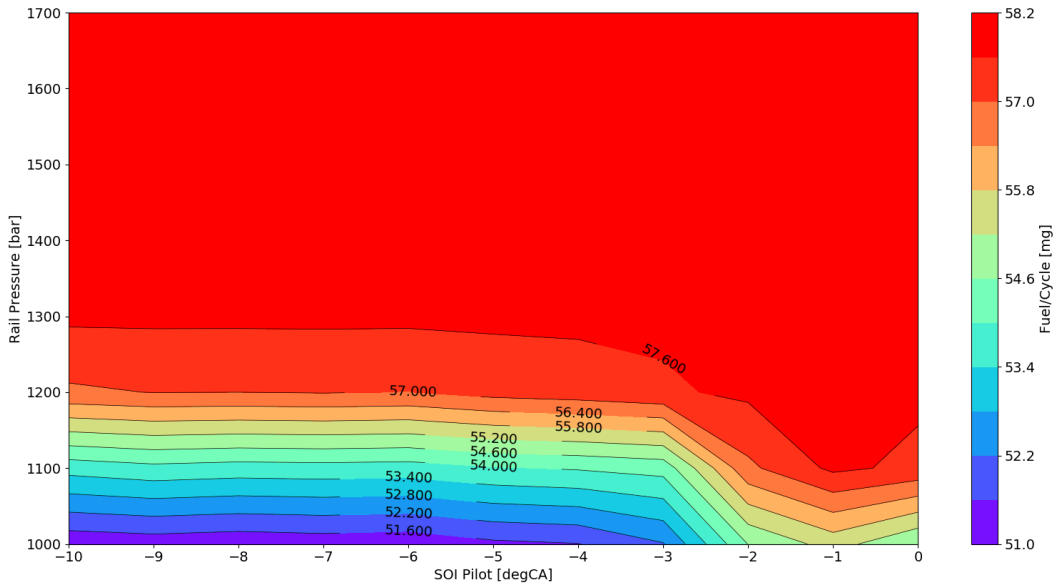

Figure 85: Parameter Set II - fuel/cycle

12 Combustion Knocking Assessment

The first section of this chapter covers the introduction of the full flexible multi body dynamic (MBD) model, with a comparison between different modelling techniques in terms of cylinder gas load application, as well as a comparison with measurements with a focus on cycle to cycle variation. The second section contains the assessment of structure borne noise (SBN) on the MBD model. In the last section finally, the air borne noise (ABN) CKI is assessed on the acoustic model of the engine.

12.1 Multi Body Dynamic Model Introduction

The MBD model used for CKI assessment, therefore the evaluation of structural accelerations as well as air borne noise, is build up in Excite™ PowerUnit. It contains dynamic reduced condensed flexible bodies. A schematic picture of the model is given in Figure 86.

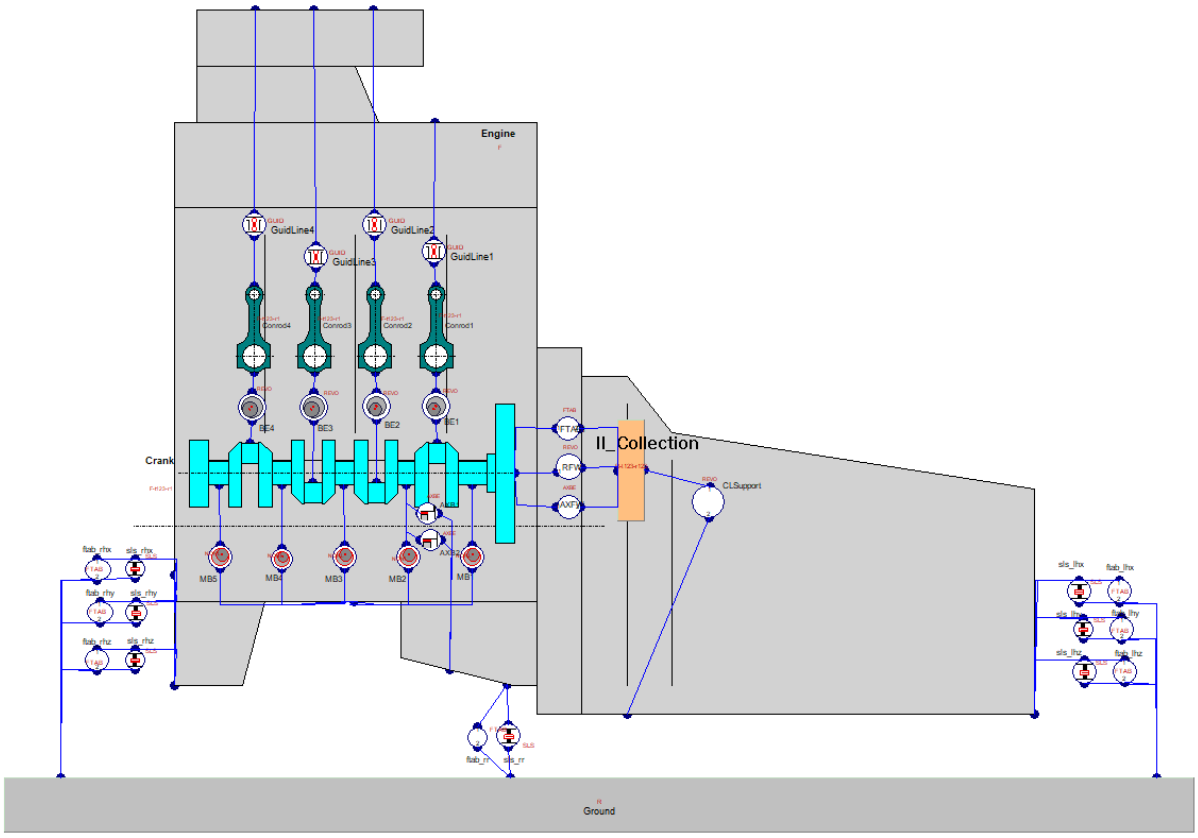

Figure 86: Scheme of flexible MBD model

It consists out of an engine block, four conrods, a crankshaft and a flywheel. The pistons are not expressed by bodies in this model. Their influence in terms of mass and inertia is added by a force applied on the conrods additional to the gas force. As the following evaluation will be done between 500Hz – 4000Hz, the bodies are condensed to frequencies up to 4500Hz. This will ensure a sufficient dynamical behaviour of the investigated bodies. This frequency range is chosen in a way to cover most of the relevant eigenfrequencies of the engine structure. A similar range with 500Hz – 3000Hz

is thereby also suggested by [25]. The mounting of the engine is realized through non-linear spring damper and velocity displacement joints coupled with a rigid body containing appropriate nodes at the engine mount positions. The contact between conrods and liner is achieved by a linear spring damper approach coupling the conrods small end nodes with a set of nodes on the liners thrust- respectively anti thrust side. The conrods big end is constraints through a nonlinear center to center coupling to the crankshaft pins. Through nonlinear spring damper couplings, the flywheel is bounded to the crankshaft. The crankshaft itself is connected by nonlinear spring damper surface to center couplings with the power unit.
As above described, almost all joints are nonlinear and coupled with full flexible bodies. Thus, the system itself is highly nonlinear and must be solved in time domain.

12.2 Modelling Comparison Gas Force Application.

To evaluate the influence of the gas force acting on the housing, three models with different gas load application are build up.

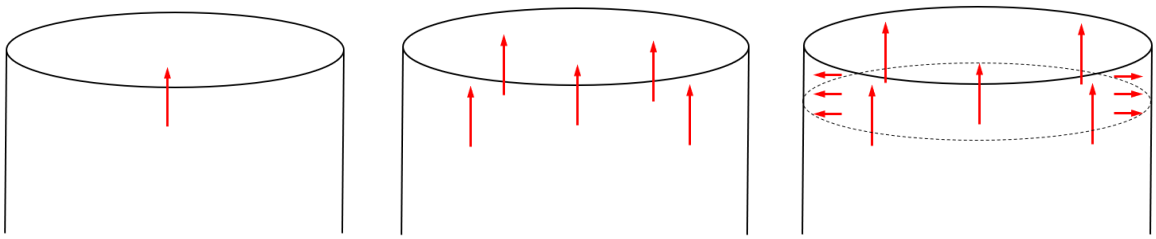

Figure 87: Gas force application illustration

As illustrated in Figure 87, three different gas load application types are introduced. The first one, or subsequently called model I, features one center force, acting on a retained node coupled by a distributed coupling (RBE3) to body nodes in the combustion chamber. The middle model of Figure 87, or model II, contains five retained center nodes uniform distributed in the combustion chamber, also coupled by a kinematic coupling to selected combustion chamber nodes. For model II one sub force is thereby one fifth of the total gas force. For the rightest model in Figure 87, or model III, five retained nodes as introduced in model II, plus a pressure acting on the cylinder jacket is used. The cylinder jacket represents thereby the surface remaining, when the piston reaches its TDC. For model three, the pressure distribution is thereby considered during condensation task with a uniform pressure of 1. As the FE-model is in the unit system N-mm-s, a pressure of 1 corresponds to 1 MPa. When performing the actual simulation, the gas pressure acting in the combustion chamber scales the uniform pressure according to the actual pressure trace. This is possible as the model is of course linear elastic.

12.2.1 Model Comparison Results

For further investigations on the behaviour of the different models, the MBD model introduced in Figure 86, is equipped with the three different FE-bodies introduced in Figure 87. As operating points for comparison for 1500rpm IFILE 1 (low knock) and IFILE 8 (high knock) is selected. For 2000rpm IFILE 22 (low knock) and IFILE 25 (high knock) are picked. As evaluation nodes, one at

the valve cover, one at the front bracket and one at the housing are selected. Their location is illustrated in Figure 88.

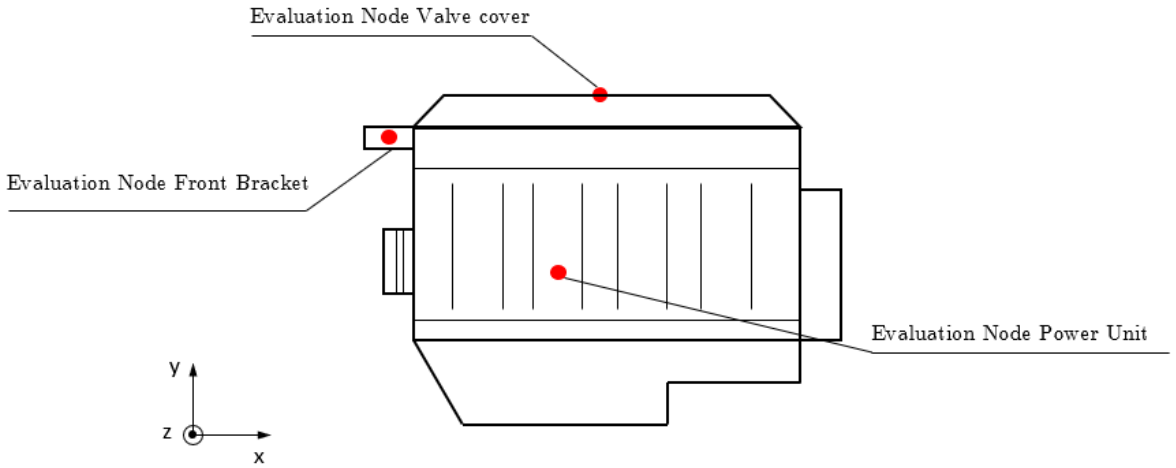

Figure 88: Illustration evaluation nodes for simulation

Evaluated is the acceleration in frequency domain as a third octave band on the previous introduced virtual accelerometer positions. The acceleration signals in time domain can be found in appendix 17.2 MBD Model Comparison Acceleration Signal Time Domain.

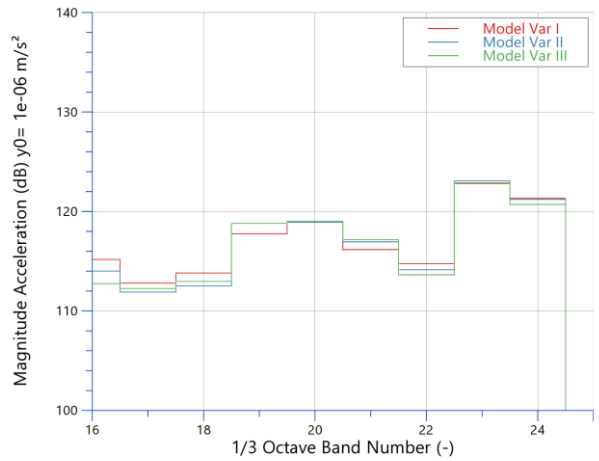

Figure 89: Valvecover node 3809299 DOF 2 - IFILE 1 1500rpm

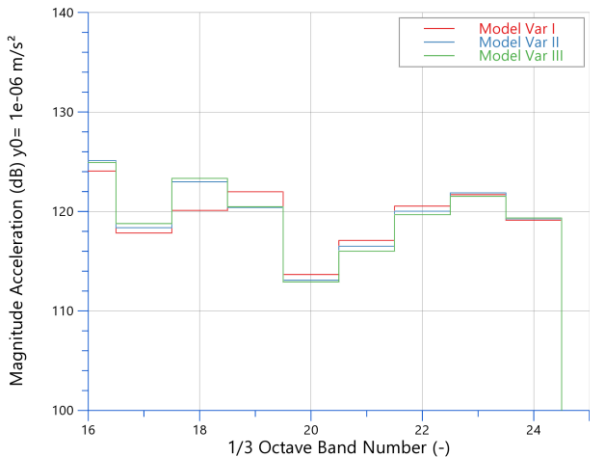

Figure 90: Valvecover node 3809299 DOF 3 - IFILE 1 1500rpm

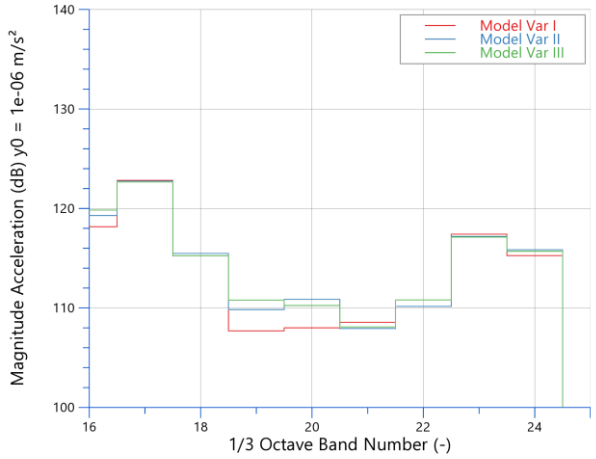

Figure 91: Power unit node 1527335 DOF 3 - IFILE 1 1500rpm

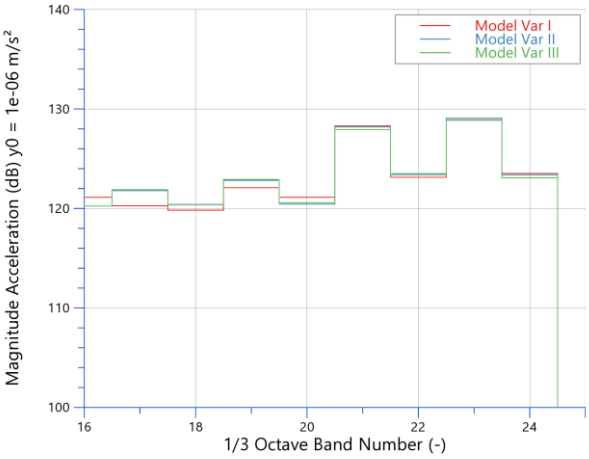

Figure 92: Front bracket node 4127437 DOF 2 - IFILE 1 1500rpm

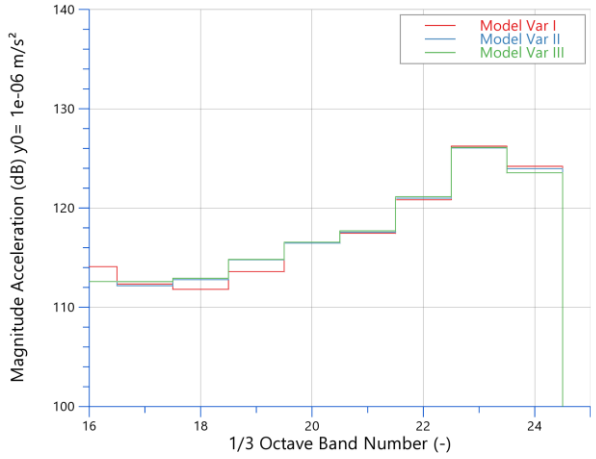

Figure 93: Valvecover node 3809299 DOF 2 - IFILE 8 1500rpm

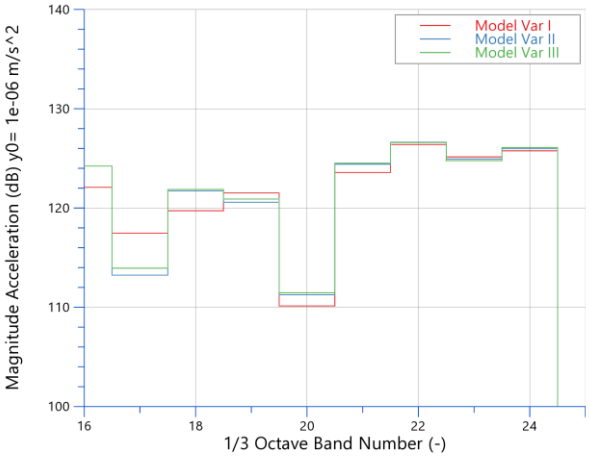

Figure 94: Valvecover node 3809299 DOF 3 - IFILE 8 1500rpm

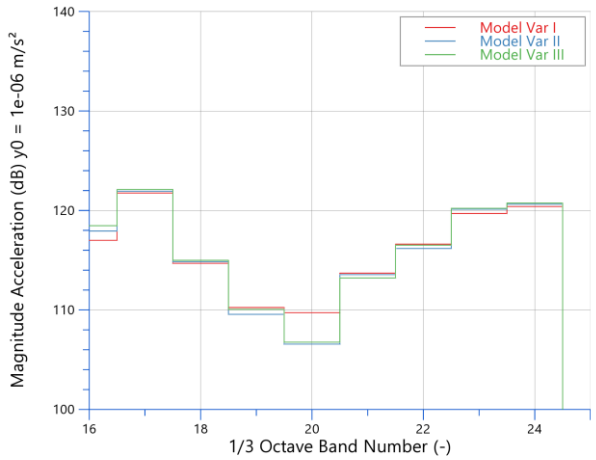

Figure 95: Power unit node 1527335 DOF 3 - IFILE 8 1500rpm

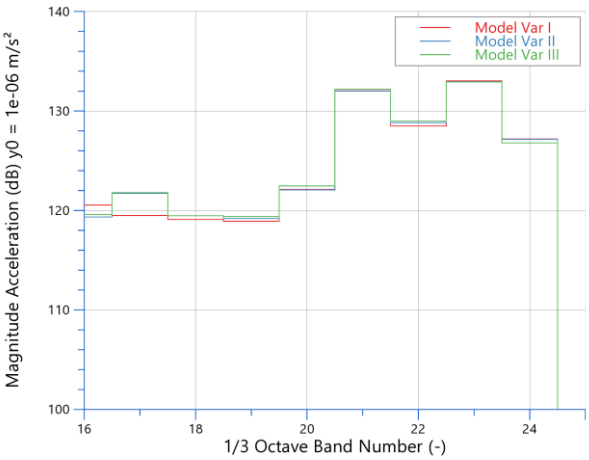

Figure 96: Front bracket node 4127437 DOF 2 - IFILE 8 1500rpm

As quality criteria functions again the 3dB limit as already introduced in 10.3 Cycle Variation During Steady State Operation. When investigating the frequency bands starting from third octave #17 and above, no deviation higher than 3db occurs. For higher frequency range the deviation falls even below 1db acceleration level. To eliminate the influence of excitation frequencies on the eigenfrequencies of the bodies, the acceleration levels for 2000rpm for the same retained nodes are investigated.

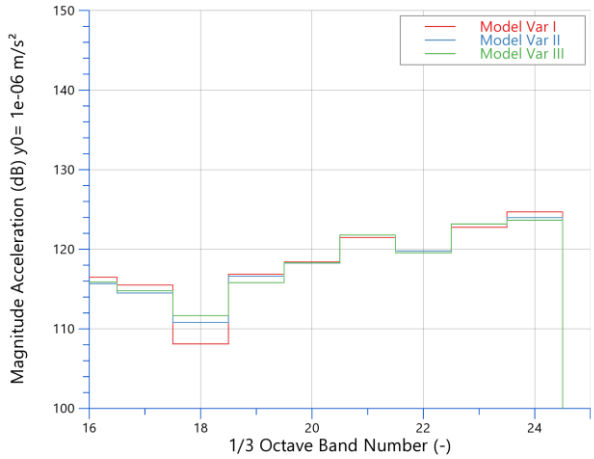

Figure 97: Valvecover node 3809299 DOF 2 - IFILE 22 2000rpm

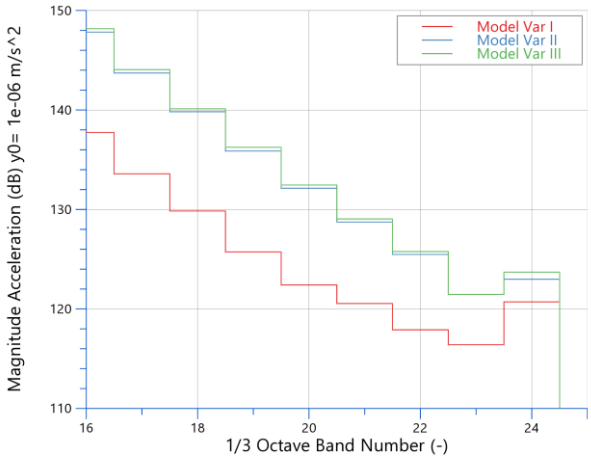

Figure 98: Valvecover node 3809299 DOF 3 - IFILE 22 2000rpm

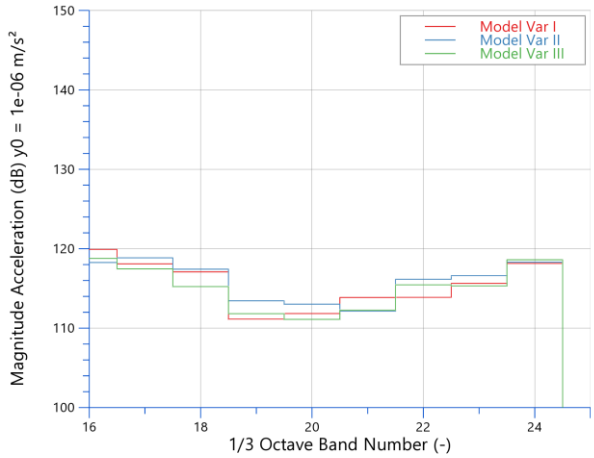

Figure 99: Power unit node 1527335 DOF 3 - IFILE 22 2000rpm

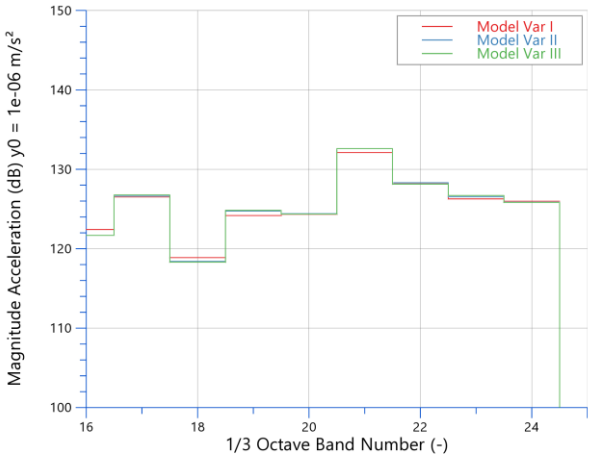

Figure 100: Front bracket node 4127437 DOF 2 - IFILE 22 2000rpm

For 2000rpm and low knock, the deviation in acceleration level exceeds the limit of 3 dB by 5 dB for the 17th octave band, and over 10 dB for the 15th octave band at the liner surface (Figure 99). Also, for the valve cover in DOF 3 (direction in which load change between thrust side (TS) and anti-thrust side (ATS) of the piston takes place) a deviation over 10dB occurs in the lower to mid frequency range (Figure 98), which can be addressed to numerical reasons leading to an offset.

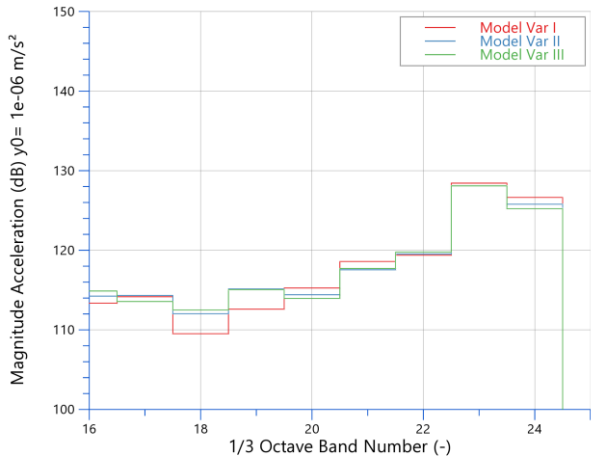

Figure 101: : Valvecover node 3809299 DOF 2 - IFILE 25 2000rpm

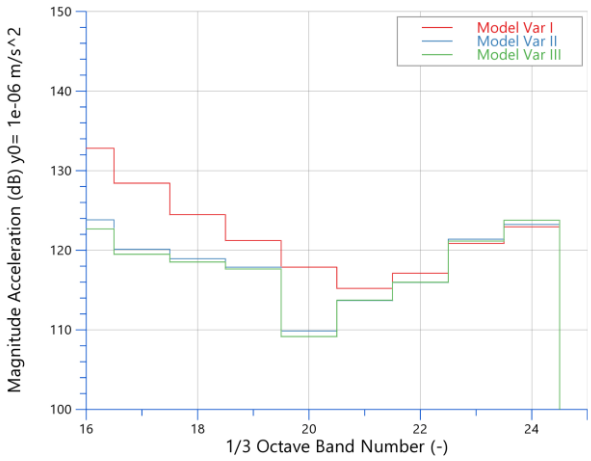

Figure 102: Valvecover node 3809299 DOF 3 - IFILE 25 2000rpm

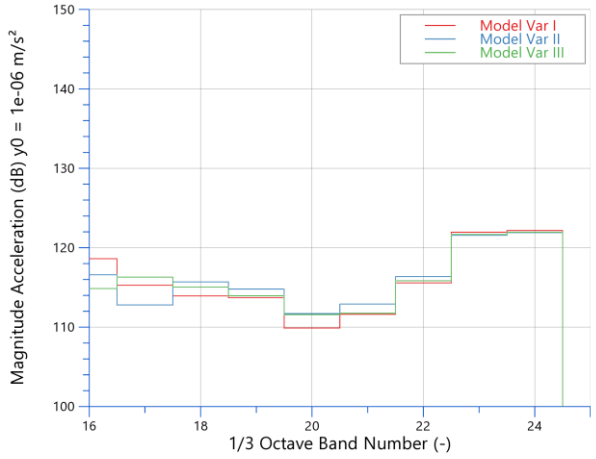

Figure 103: Power unit node 1527335 DOF 3 - IFILE 25 2000rpm

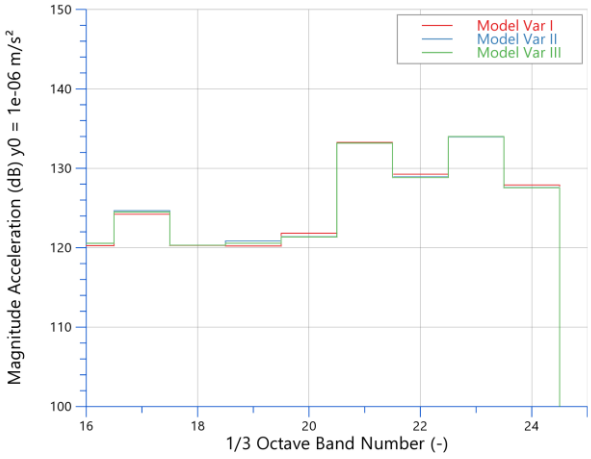

Figure 104: Front bracket node 4127437 DOF 2 - IFILE 25 2000rpm

For 2000rpm and high knock, the limit of 3dB is again not reached at the liner surface in DOF 3 direction. For the remaining virtual accelerometer positions the limit is reached though.

As a conclusion of this comparison can be stated that for investigations at the engine brackets the modelling detail level is satisfied with the simple approach of one retained center node and kinematic coupling. This is especially the case in transfer path analyses where the transfer of vibration from the engine to the engine mounts and further on to the vehicle structure is investigated. This is mainly for passenger NVH investigations of importance. But when it comes to airborne noise radiated from the surfaces of the engine, the excitation mechanisms have to be understood well in order to cover the relevant effects. For these cases a deeper modelling level for the exciting gas force can be of advantage.

12.3 Acoustic Model Introduction

For the calculation of the airborne noise radiated from the engine structure a separate acoustic model based on the multi body dynamic (MBD) model is build up. Therefore, a so-called data recovery is first performed on the MBD model. The data recovery transfers the results generated with the condensed model to the uncondensed model (displacements of condensed nodes are recalculated to displacements of uncondensed nodes). For this task a recovery-matrix was separately created during the condensation task of the reduced model. The recovery matrix links the mass and stiffness matrices of the condensed model, to the ones of the uncondensed model. The data-recovery itself is performed in terms of surface velocity levels, as they are required as an input for the airborne noise calculation. The velocity levels are calculated in frequency domain for a range of 500Hz-4000Hz.

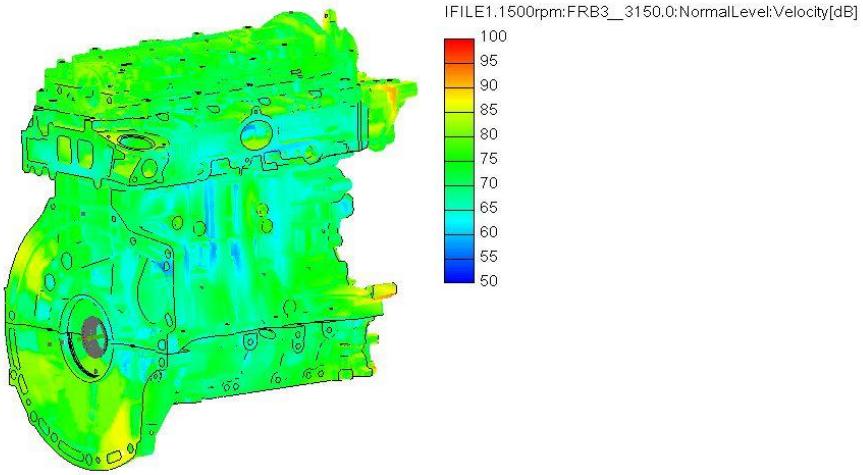

Figure 105: Normal Surface Velocity Levels [dB] – IFILE1 3150 Hz

In Figure 105 the surface velocity levels normal on the structure are illustrated for case IFILE1 and a frequency of 3150 Hz.
When generating the acoustic mesh for the simulation, a cuboid room is defined that fits right over the structure and is defined by the structure's biggest dimensions. An illustration of the mesh discretising the cuboid room around the engine block is given by Figure 106.
In a next step the mesh is automatically divided in cuboids defined as inside and outside elements. The inside elements are containing Gauß-points which are used for mapping the velocity of individual surface nodes on the closest surfaces of the inside acoustic mesh elements. Through this approach it is ensured that results are accurate even when the element size itself is rough. For the engine block used in this thesis, the inner acoustic mesh is illustrated in Figure 107. The outer elements pictured in Figure 108 are than automatically merged by the tool in bigger elements to further reduce simulation time, the merged mesh can be seen in Figure 109.

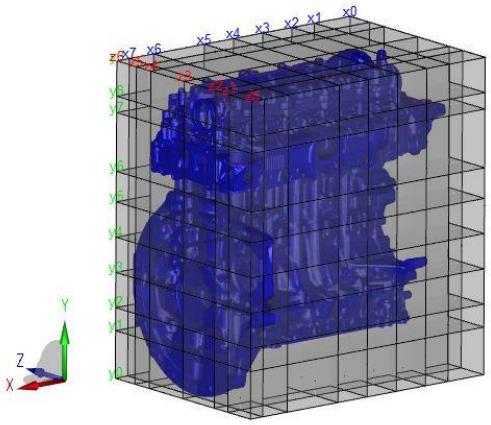

Figure 106: Acoustic mesh - discretization

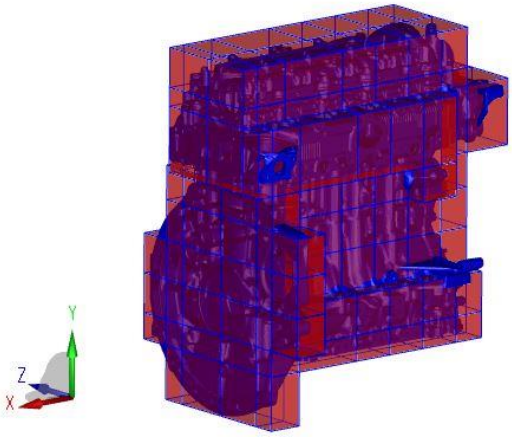

Figure 107: Acoustic mesh - inner elements

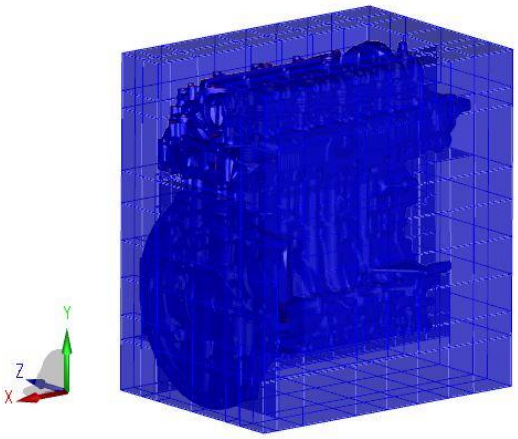

Figure 108: Acoustic mesh - outer elements

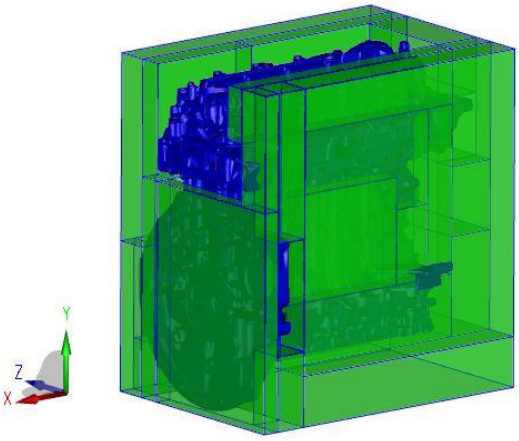

Figure 109: Acoustic mesh - merged outer elements

12.4 Injection Strategies Influencing Structural Vibrations and Radiated Noise

Pressure traces received from injection variations performed in 11.5 as well as calibrated pressure traces resulting from measurements are used as input data for above introduced MBD model to achieve vibrations on the engine surface used to calculate the radiated noise in order to evaluate the CKI. Due to high computational effort and large amount of data generated for each simulation run, the CKI assessment is performed for low and high CNI at 1500 rpm and 2000 rpm as well as 11.5.1 Case I – Variation of Rail Pressure and 11.5.2 Case II – Variation of SOI of Pilot Injection only.
For all below stated cases, the CKI is evaluated with the time signal at microphone position 5, which refers to the top position above the engine. Therefore, the results for amplitude and phase are transferred from frequency domain to time domain through an IFFT. The position of microphone 5 in illustrated in Figure 110.

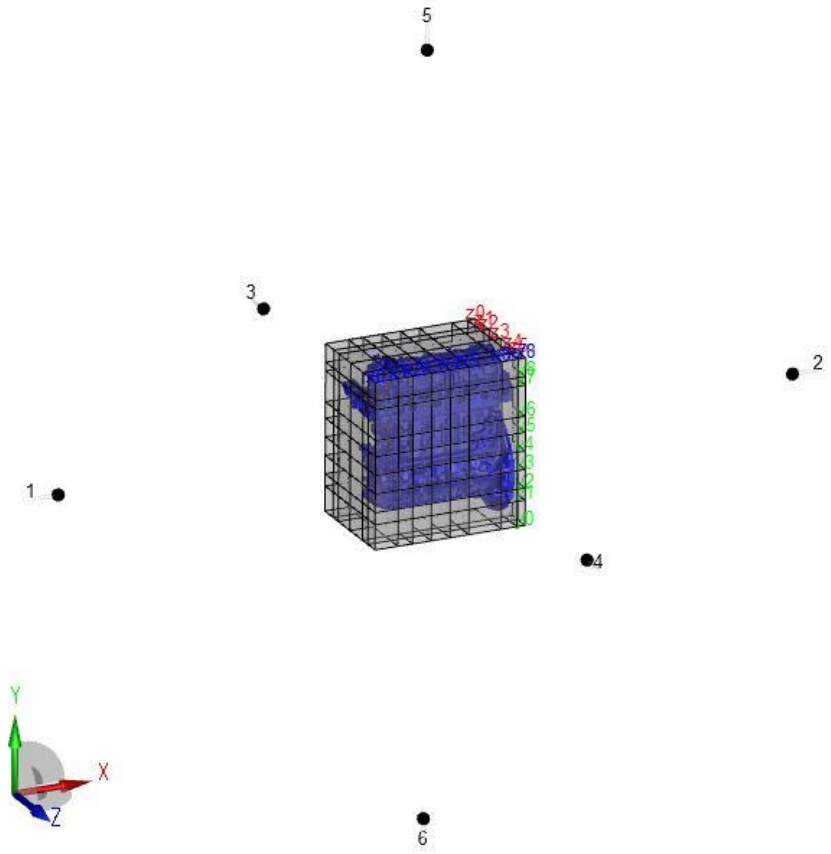

Figure 110: Microphone positions for ABN evaluation

12.4.1 Calibrated Cylinder Pressure Traces

For the calibrated cylinder pressure traces resulting from the measurements, again the cases IFILE1 and IFILE8 featuring low- as well as high knock at 1500 rpm and IFILE22 and IFILE25 featuring low- and high knock at 2000 rpm are selected. To compare the evaluated CKI from the associated sound pressure responses in time domain, the surface integral levels of the engine are additionally analysed for each case.

Table 18: Calibrated cylinder pressure traces 1500rpm - knocking indices

Case	CNI [-]	CKI [-]
IFILE1	82	155
IFILE8	87	165

As stated in Table 18 the CNI as well as the CKI for low knock (IFILE1) and high knock (IFILE8) have a good correlation between each other. This is also visible when evaluating the integral over the normal surface velocity level for the engine structure, illustrated in Figure 111.

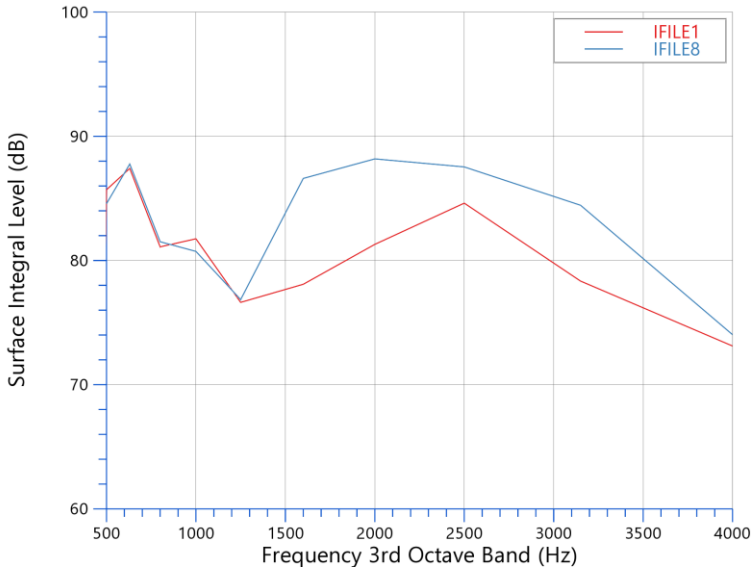

Figure 111: Surface velocity integral - low/high knock 1500rpm

As the CKI is only calculated by the time domain signal of one microphone located at the top position (above the engine), additionally the mean value of the sound pressure of every microphone position (Figure 110) is evaluated in frequency domain. For IFILE1 and IFILE8 they are illustrated in Figure 112. As for different excitations the sound radiation characteristic can change, it is necessary to evaluate the sound pressure at multiple positions around the engine. This is in Figure 112 done with mean values of the radiated sound pressure for all six microphone positions in frequency domain. Thereby it is apparent that also the radiated noise is higher for the high knock case compared to the case featuring low knocking.

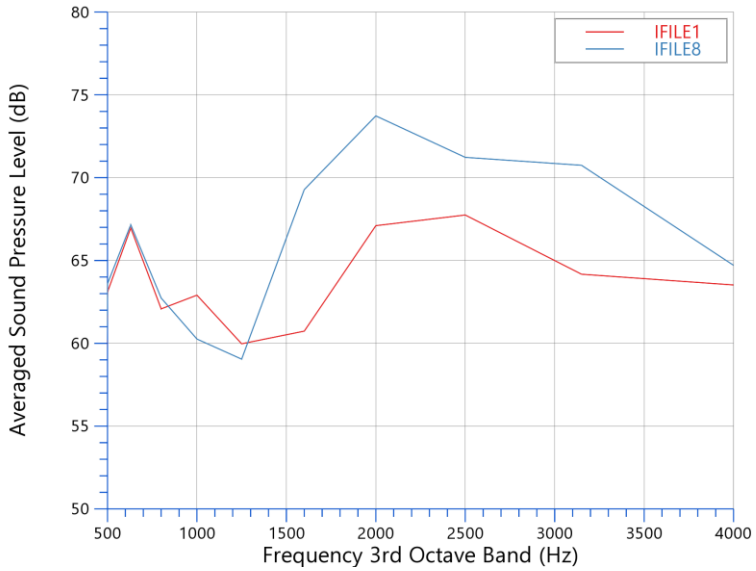

Figure 112: Averaged microphone sound pressures - low/high knock 1500rpm

In Figure 113 to Figure 116 surface velocities with their associated sound pressures on the field point mesh for 1500rpm are illustrated. The field point mesh containing the sound pressures is thereby cut open to receive a view on the radiating surface in the inside. Two distinct frequencies are thereby selected. One at medium frequencies with approximately 1203 Hz and one at higher frequencies at approximately 2994 Hz. As the integral surface velocity level for IFILE1 and IFILE8 is nearly identical, we get the same picture when looking at the sound pressure levels as well as their distribution in Figure 113 and Figure 114. A different case is thereby given on the higher frequency range. As integral surface velocity levels differ for 5.3 dB, the sound pressure levels are also significantly higher in Figure 115 and Figure 116. It is also clearly to see that the highest sound pressure levels occur at the top and bottom of the structure. As a reason to this microphone position 5 is selected as evaluation position for all cases. This behaviour occurs from the reason that especially the valve cover features a large surface with lower stiffness when directly compared to the engine block.

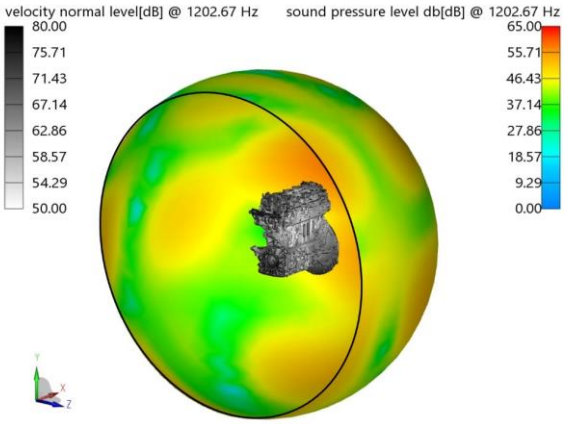

Figure 113: Radiated noise and surface velocity levels - IFILE1 1202.67Hz

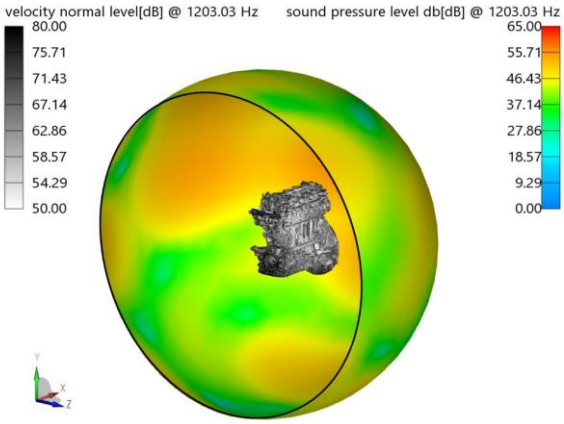

Figure 114: Radiated noise and surface velocity levels - IFILE8 1202.67Hz

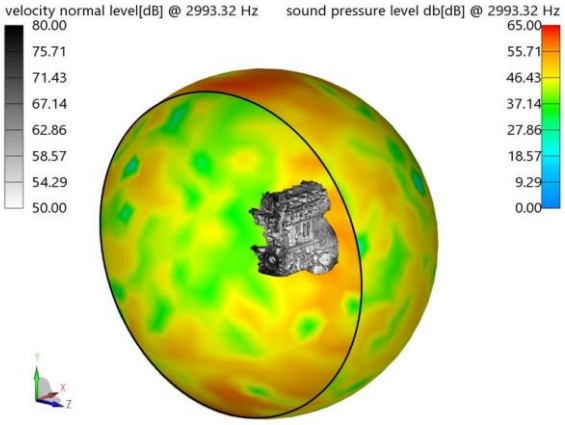

Figure 115: Radiated noise and surface velocity levels - IFILE1 2993.32Hz

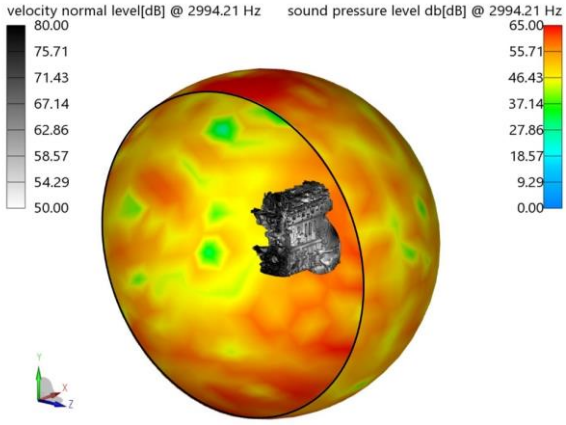

Figure 116: Radiated noise and surface velocity levels - IFILE8 2994.21Hz

For Figure 113 to Figure 116 it is also clearly visibly that the sound radiation characteristic does not change drastically between the individual cases at same frequency levels, especially for the top microphone position where the CKI is evaluated.

For 2000rpm represented through cases IFILE22 (low knock) and IFILE25 (high knock) the CNI's and CKI's are stated in Table 19.

Table 19: Calibrated cylinder pressure traces 2000rpm - knocking indices

Case	CNI [-]	CKI [-]
IFILE22	140	131
IFILE25	183	148

Compared to the surface velocity integral levels in Figure 111, the surface velocity integral levels for 2000 rpm illustrated in Figure 117 are lower, in particular for the higher frequency range. Although the CNI levels for 2000 rpm are much higher compared to the CNI levels for 1500 rpm. This circumstance can be traced back to the high sensivity of the CNI, which was already stated in 10.4 CNI Sensitivity in Measurements. Thus, short but rapid changes in the pressure gradient can push up the CNI easily, but the overall surface velocity levels stay still low as furthermore the radiated noise does. Thereby it is understandable that those short changes in the pressure gradient are damped away through the mass and stiffness of the engine structure. As the structure of the engine block gets excited by the gas inside the combustion chamber, different damping mechanisms are of relevance. According to [25], the cut-off frequency for crank case wall parts out of cast iron material, is located around approximately 2500Hz. Below the cut-off frequency, the structure is considered as bending weak, the sound reduction is driven by the mass of the structure. Above the cut-off frequency, the structure is considered as bending stiff, thereby the sound reduction is driven by the stiffness of the structure. For executed crank case designs, the cut-off frequency is selected rather high, as the sound radiation is poor below the cut-off frequency and high above it [25]. As the CKI sets up directly on the radiated noise those effects are already considered, which can be seen by comparing the CKI levels for the 1500rpm cases with those from the 2000 rpm cases. Thus, the CKI levels for 2000 rpm are also lower as the integral level of the surface velocity is.

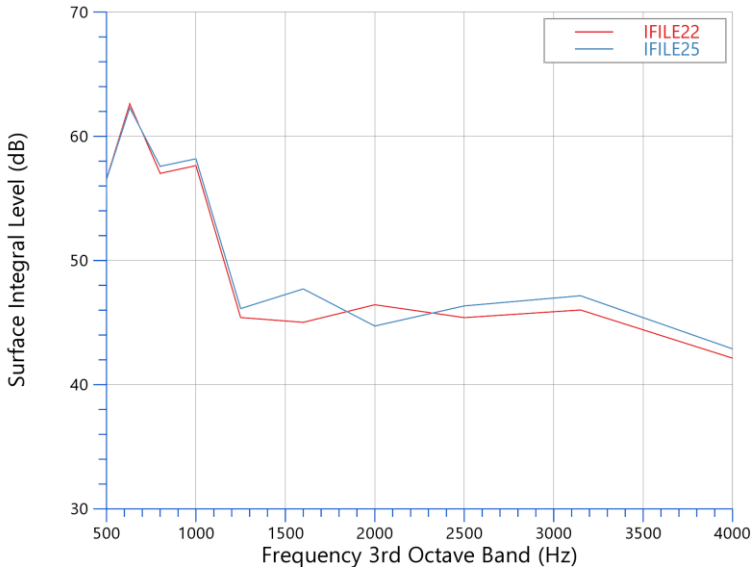

Figure 117: Surface velocity integral - low/high knock 2000rpm

In terms of averaged sound pressures over all microphone positions, illustrated in Figure 118, the trend is again evident for 2000rpm. Case IFILE25, featuring high knocking, delivers above around 2000Hz a clearly higher sound pressure level up to 4000Hz.

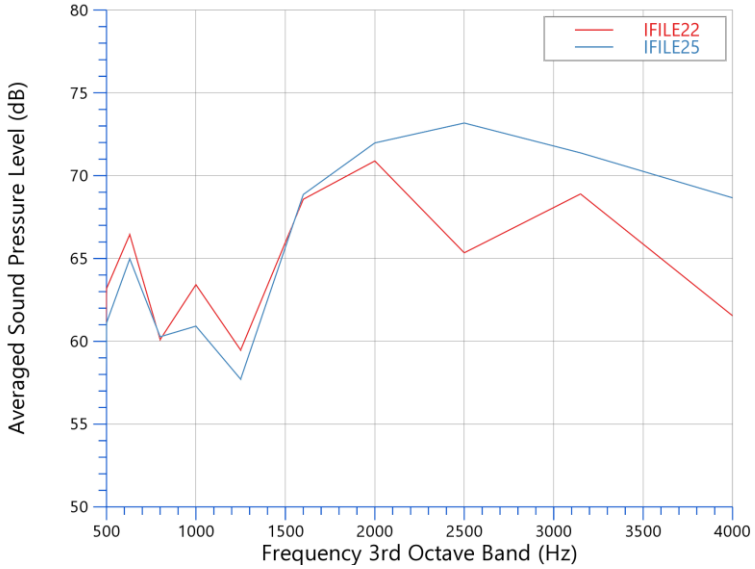

Figure 118: Averaged microphone sound pressures - low/high knock 2000rpm

For lower frequency range the difference in surface velocity as well as radiated noise is again minor, and the noise distribution is similar as illustrated in Figure 119 and Figure 120 for low- and high knock injection strategy. This similar distribution in sound pressure can again be interpreted as a small change in the sound radiation characteristic.

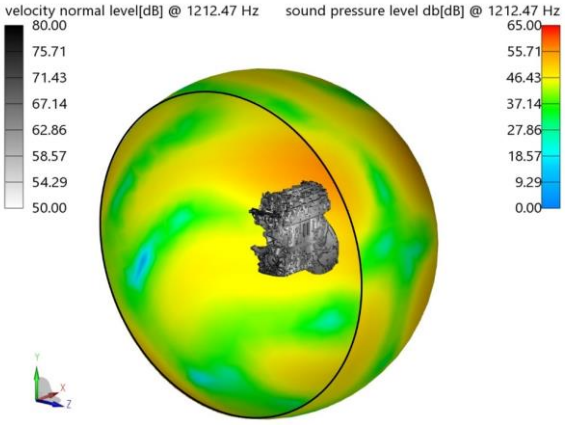

Figure 119: Radiated noise and surface velocity levels - IFILE22 1212.47Hz

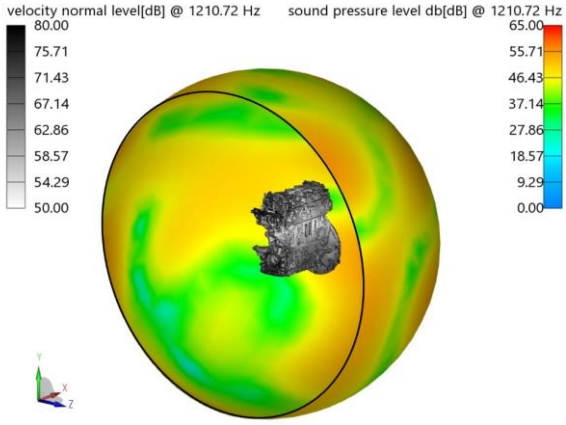

Figure 120: Radiated noise and surface velocity levels - IFILE25 1210.72Hz

For higher frequency range, especially starting from approximately 1250Hz and above, the variation in surface velocity level and sound pressure level is more distinct.

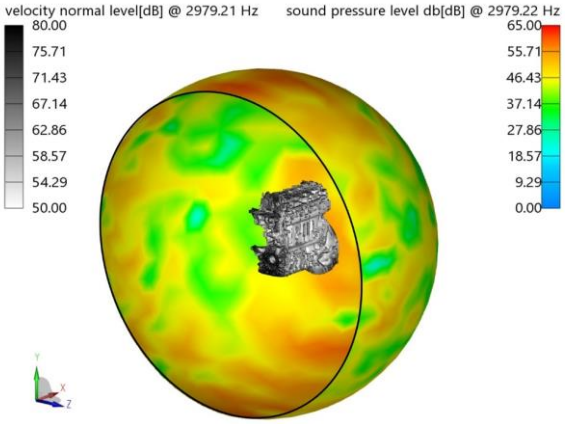

Figure 121: Radiated noise and surface velocity levels - IFILE22 2979.22Hz

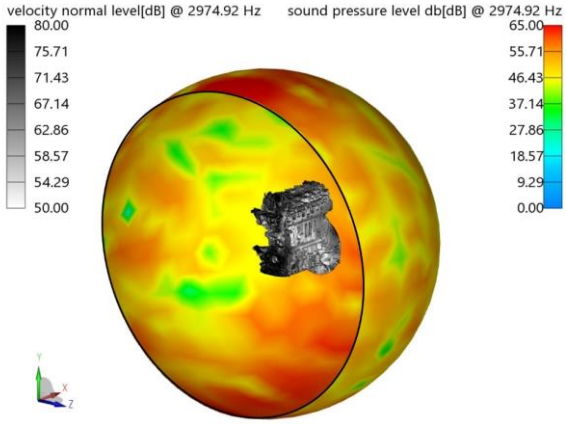

Figure 122: Radiated noise and surface velocity levels - IFILE25 2974.92Hz

12.4.2 Case I – Variation of Rail Pressure

For the injection variation of the parameter rail pressure, conducted in 11.5.1 Case I – Variation of Rail Pressure, the results are now evaluated in relation to CKI and related noise.

Table 20: Injection variation rail pressure 1500rpm - knocking indices

Case	CNI [-]	CKI [-]
InjVarPress 1000bar	83	114
InjVarPress1100bar	91	116
InjVarPress 1200bar	104	116
InjVarPress 1300bar	110	118

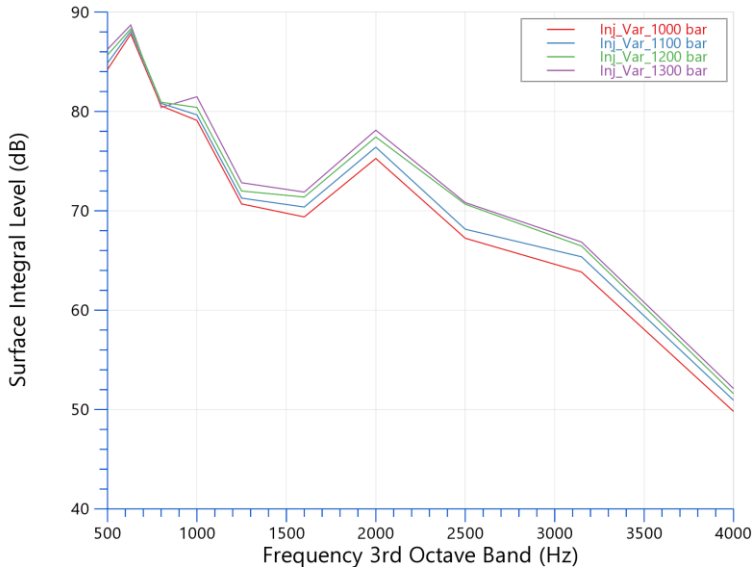

Figure 123: Surface velocity integral - injection variation rail pressure 1500rpm

The distribution of the averaged sound pressures outlined in Figure 124 shows the same trends as the integrals of the surface velocity levels illustrated in Figure 123.

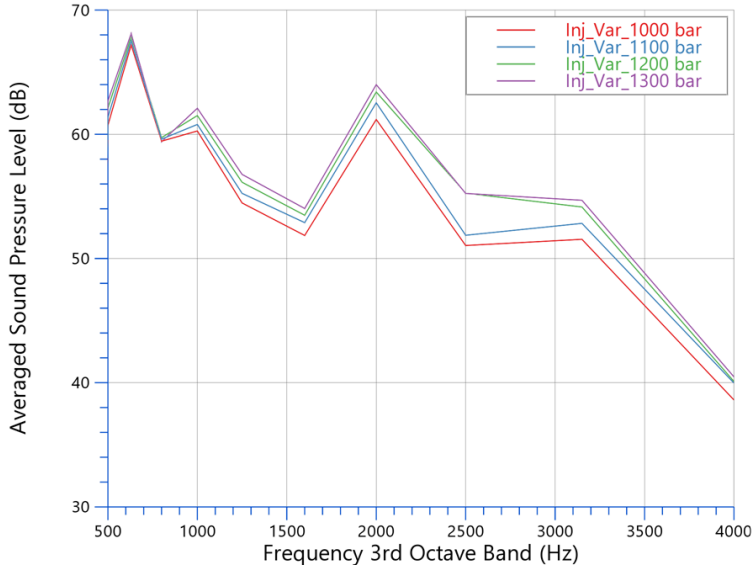

Figure 124: Averaged microphone sound pressures - injection variation rail pressure 1500rpm

When comparing Figure 125 to Figure 128 in terms of radiated sound pressure characteristics, the distribution illustrated for approximately 2010Hz to 2030Hz is very similar for the individual operating conditions. Again, the CKI is evaluated at the top microphone position.

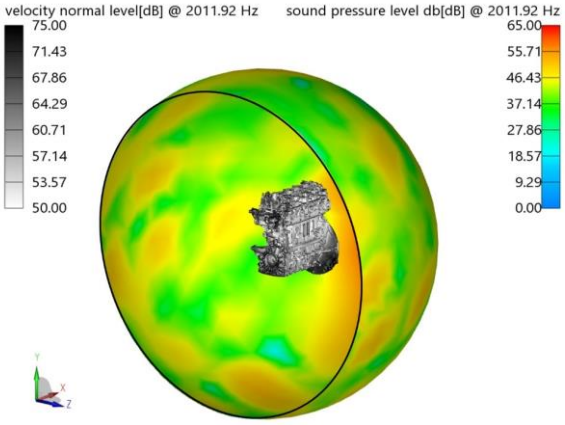

Figure 125: Radiated noise and surface velocity levels – InjVarPress - 1000bar 2011.92Hz

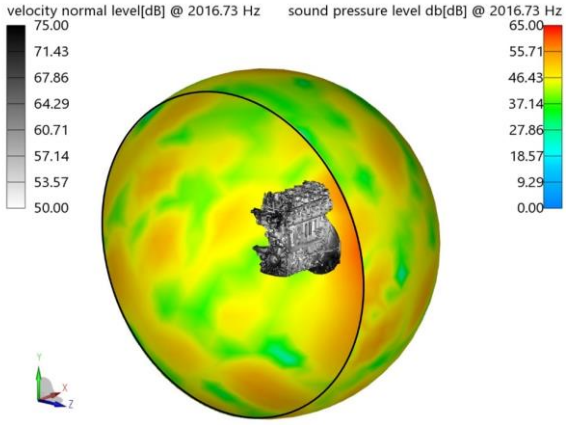

Figure 126: Radiated noise and surface velocity levels – InjVarPress - 1100bar 2016.73Hz

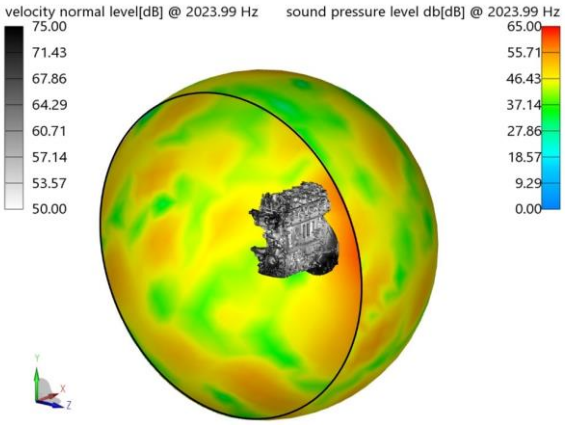

Figure 127: Radiated noise and surface velocity levels – InjVarPress - 1200bar 2023.99Hz

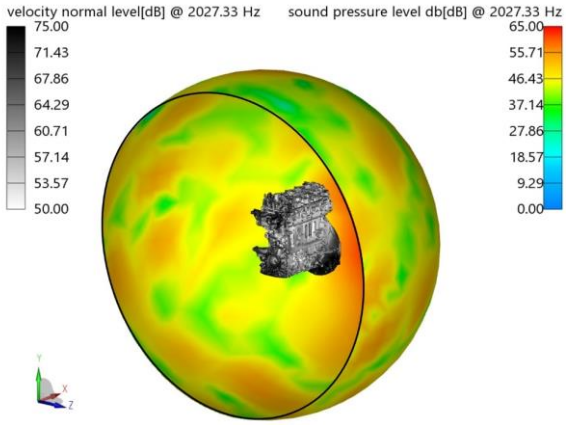

Figure 128: Radiated noise and surface velocity levels – InjVarPress - 1300bar 2027.33Hz

By comparison of the CNI levels with the associated CKI levels stated in Table 20, it is again notable that the CNI is more sensitive than the CKI when it comes to changes in the cylinder pressure. When comparing the CNI to the appropriate cylinder pressure traces (Figure 61), respectively the pressure rise traces (Figure 62) the response of the CNI is overall reasonable. Through the damping of the structure, the effective change of the surface velocity which is illustrated in Figure 123 is with 2.8 dB at 2000 Hz accordingly low. Thus, also the deviation in radiated noise is only minor for the individual cases (Figure 125 - Figure 128). The evaluation at slightly different frequency levels origins of the numerical error between the individual cases. First in time domain by calculating vibrations of the condensed nodes, second in frequency domain by calculating the vibrations of the nodes at the uncondensed mesh as well as through calculation of the radiated noise itself.

12.4.3 Case II – Variation of SOI of Pilot Injection

For the cylinder pressure traces generated in 11.5.2 Case II – Variation of SOI of Pilot Injection, the evaluation regarding to structure borne noise as well as airborne noise is performed in this section. In Table 21 the combustion noise indices over the individual cases are stated.

Table 21: Injection variation SOI PI 1500rpm - knocking indices

Case	CNI [-]	CKI [-]
InjVarSOIPI -10degCA	87	117
InjVarSOIPI -5degCA	96	117
InjVarSOIPI 0degCA	59	113

The correlation between CNI and CKI is also for variable pilot injection satisfied, especially for the pilot injection very close to the main injection at 0 degCA. The deviation in correlation between CNI and CKI for the cases -10 degCA and -5 degCA are clearer when looking at the associated pressure traces depicted in Figure 67 as well as the pressure rise illustrated in Figure 69. Thereby it is apparent that small pressure fluctuations, especially at -5degCA are responsible for pushing up the CNI value, even if those fluctuations can not necessarily be seen when evaluating the structure borne noise (Figure 129) respectively the air borne noise (Figure 131 - Figure 133) and CKI.

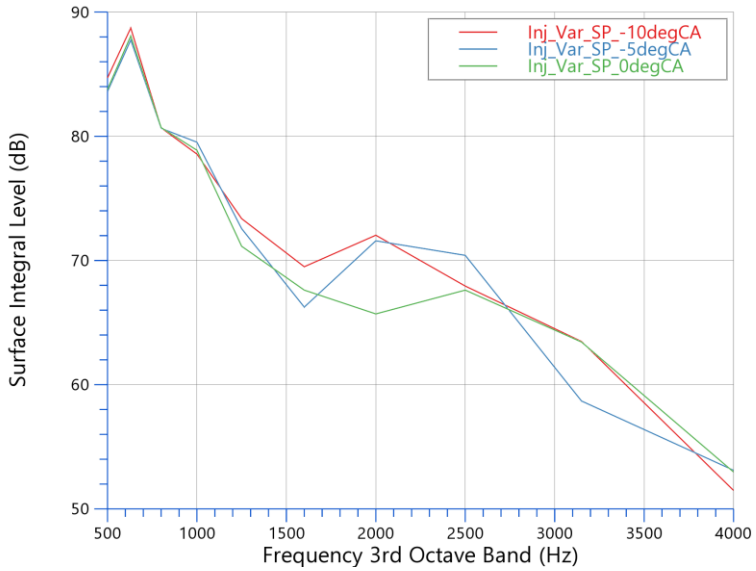

Figure 129: Surface velocity integral - injection variation SOI pilot injection 1500rpm

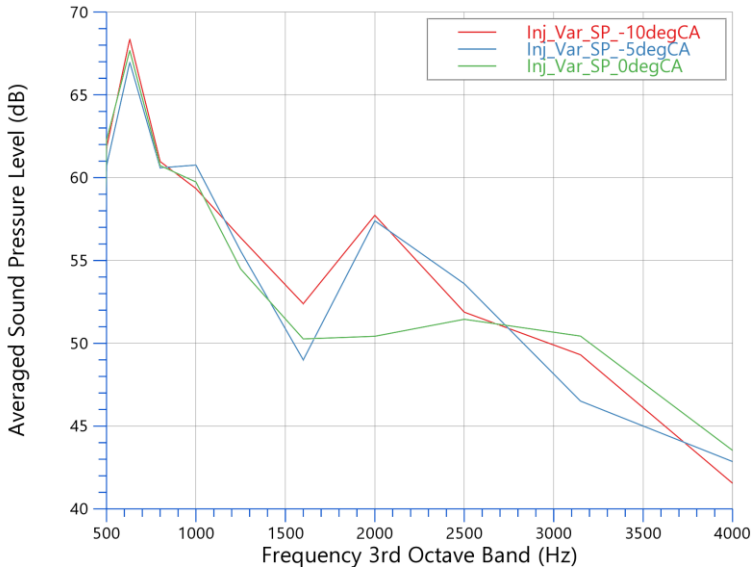

Figure 130: Averaged microphone sound pressures - injection variation SOI pilot injection 1500rpm

For Figure 130 the averaged sound pressure levels in frequency domain are illustrated for the different operating conditions of Case II. When directly comparing to the integral of the surface velocity levels, illustrated in Figure 129, same trends are apparent. Regarding the sound radiation characteristic, especially for the area above the engine where the CKI is evaluated, same distributions are visible when comparing the different operating conditions in Figure 131 - Figure 133.

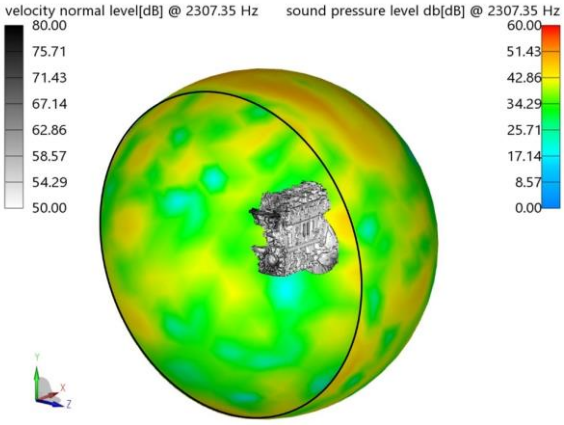

Figure 131: Radiated noise and surface velocity levels – InjVarSOIPI - -10degCA 2307.35Hz

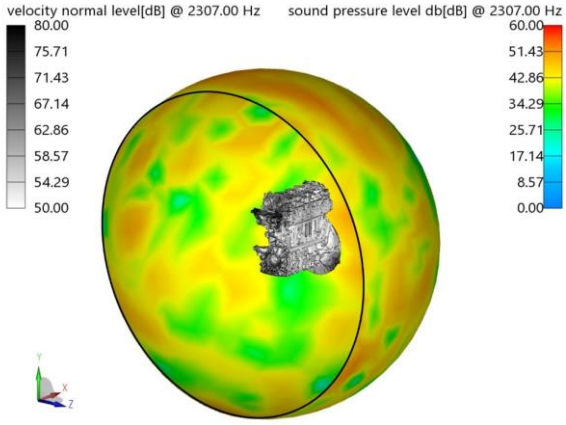

Figure 132: Radiated noise and surface velocity levels - InjVarSOIPI - -5degCA 2307.00Hz

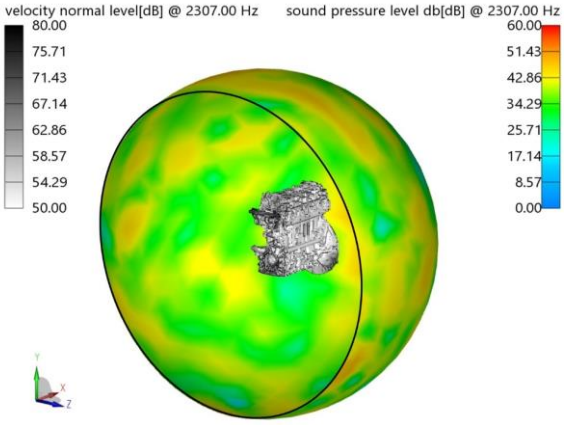

Figure 133: Radiated noise and surface velocity levels - InjVarSOIPI - 0degCA 2307.00Hz

13 Conclusion

Through the development of a simulation-based methodology to assess combustion noise during the design process, it could be shown that a linkage of a combustion index based on the cylinder pressure for system simulation (CNI) as well as based on radiated noise (CKI) for component simulation with certain combustion parameters such as injection timing and pressure is possible.
As the combustion noise index (CNI) sets up directly on the cylinder pressure, no damping characteristics of the engine structure as well as radiation efficiency are considered. Therefore, CNI is very sensitive to variations of combustion parameters affecting mainly the premixed combustion phase and therefore the gradient of the cylinder pressure trace. However, the overall trends between injections variations within one operating point, but also between different individual operating points are satisfying. Direct comparison of absolute values within simulated operating points, but also with measurements is at this stage not possible. This is a reason as for simulation only one cycle is generated and evaluated for each case. Thus, no cycle variation is considered. Fluctuations occurring during induvial cycles are therefore not covered in simulation. For measurements, outlined in 10.3 Cycle Variation During Steady State Operation, CNI values for many cycles are calculated and averaged to one CNI value for a specific operating point.
For the combustion knocking index (CKI), a good correlation with combustion parameters could be shown also. As it sets up on radiated noise, damping characteristics of the structure are considered as well as influences on the transfer path and the radiation efficiency. Therefore, it reacts much less sensitive on variations of injection parameters as CNI does.
Also, the cycle to cycle variation in measurements is not neglectable and has to be considered when using measurement data as input for combustion simulation models or when performing comparisons between measurements and simulations.
With both indices combined predictive statements on combustion noise during the simulation process can be stated.

13.1 Summary

Through the course of the present work, a consistent workflow including models, interfaces and indices was developed to demonstrate the influence of different injection strategies for direct injection diesel engines in terms of structure borne noise (SBN) and air borne noise (ABN). Furthermore, measurements on a 1.6L diesel engine were evaluated with respect to fluctuations in CNI and cycle to cycle variations. Additionally, an investigation on gas force application in multi body dynamic (MBD) simulation was carried out, to get a better understanding on the influence of different gas load application approaches. In the end a complete picture regarding diesel knocking starting from the influence of combustion parameters to its impacts on the structure as well as on the radiated noise could be established.
Regarding to measurements was shown that overall cycle to cycle variations are for steady state testbed operations satisfying in terms of vibrations, for combustion was shown that the variation which is apparent primary in the CNI is overall quite high. Therefore, should the CNI be mainly an index for pointing out certain trends in combustion variation, rather than be a comparable index for different injection strategies among one another.
For CNI in thermodynamic combustion simulation could be stated that the index is sensitive to changes in injection strategy which are influencing the sudden burn of the air/fuel mixture in the cylinder, resulting in a sharp change of the cylinder pressure trace. Although trends can be revealed

well. Especially for evaluating combustion strategies regarding to fuel economy, performance and noise.
As CNI alone is not a satisfying criterion for radiated combustion noise, the importance of ABN and SBN evaluation was demonstrated. Mainly driven through mass and damping properties of the structure, in the end radiated noise can be different as what is expected by the cylinder pressure trace and therefore CNI. Normal surface velocity levels integrated over the power unit and sound pressure evaluations in combination with CKI showed thereby good correlation with expected results.

13.2 Outlook

Although the developed process is a sufficient approach for investigations on diesel knocking, the development of a CKI setting up on SBN would complement the topic simulation wise. Further on, the development of comparable, absolute values for CNI and CKI for simulation tasks as well as calibration factors for comparison of CNI and CKI with measurements are topics which need to be addressed in the future. In addition, emissions are a subject which were not discussed in this thesis. As emission regulations are on a global rise, the investigation on diesel knocking regarding to emissions is a top priority and should be further investigated.

14 List of Figures

Figure 1: Combustion noise assessment - workflow....1
Figure 2: Injection and combustion trace of a diesel engine [4]....4
Figure 3: Injection and combustion trace for early (left) and late (right) combustion [4]....5
Figure 4: System combustion chamber [4]....6
Figure 5: Illustration of the injection system: rail, pipe and injector with pressure positions [6]....10
Figure 6: Schematic model of the injector flow determination [6]....12
Figure 7: Illustration of the spray model [10]....17
Figure 8: Problem definition of free field with boundary conditions [16]....32
Figure 9: Auditory sensation area [20]....36
Figure 10: A-, B-, C-, and D-weighting filter traces [20]....36
Figure 11: Masking effects [21]....37
Figure 12: Convolution of a Dirac impulse with a Signal [22]....38
Figure 13: Grid points for filter definition....39
Figure 14: Linear time invariant Systems - Signals....40
Figure 15: CKI algorithm – structure [24]....41
Figure 16: CKI algorithm - evaluation of loudness levels [24]....43
Figure 17: CKI algorithm - calculation of modulation [24]....44
Figure 18: CKI algorithm - calculation of simultaneous masking [24]....46
Figure 19: Acceleration sensor and microphone positions - side view....49
Figure 20: Acceleration sensor and microphone positions - front view....49
Figure 21: Engine nomenclature measurements....50
Figure 22: Cycle variation front bracket DOF 2 - IFILE 1 - 1500rpm....52
Figure 23: Cycle variation front bracket DOF 2 - IFILE 8 - 1500rpm....52
Figure 24: Cycle variation torque arm DOF 2 - IFILE 1 - 1500rpm....53
Figure 25: Cycle variation torque arm DOF 2 - IFILE 8 - 1500rpm....53
Figure 26: Cycle variation front bracket DOF 2 - IFILE 22 - 2000rpm....53
Figure 27: Cycle variation front bracket DOF 2 - IFILE 25 - 2000rpm....53
Figure 28: Distribution CNI IFILE 1....54
Figure 29: Distribution CNI IFILE 8....54
Figure 30: Acceleration +Z direction - IFILE1 low CNI cycle....55
Figure 31: Acceleration +Z direction - IFILE1 high CNI cycle....55
Figure 32: Acceleration level +Z direction - IFILE1 low/high cycle....56
Figure 33: 1/3 Octave band +Z direction - IFILE1 low/high cycle....56
Figure 34: Acceleration +Z direction - IFILE8 low CNI cycle....57
Figure 35: Acceleration +Z direction - IFILE1 high CNI cycle....57
Figure 36: Acceleration level +Z direction - IFILE8 low/high cycle....57
Figure 37: 1/3 Octave band +Z direction - IFILE8 low/high cycle....57
Figure 38: Averaged sound pressure comparison - low/high knock operating points....58
Figure 39: Sensitivity check pressure trace....58
Figure 40: Sensitivity check combustion phase....58
Figure 41: Engine model with individual elements which are build-up of sub-elements....59
Figure 42: Interpolated map for BMEP....61
Figure 43: Valve lift table of intake valve....61
Figure 44: Valve lift table of outlet valve....61

Figure 45: Reverse engineering workflow chart for calibration 62
Figure 46: Calibration map for flow multiplier 63
Figure 47: Calibration chart of hydraulic opening delay 63
Figure 48: Calibration needle lift multiplier opening 64
Figure 49: Injection process diagram 64
Figure 50: Validation cylinder pressure trace operating point IFILE 1 65
Figure 51: Pressure trace IFILE 1 compression 65
Figure 52: Pressure trace IFILE 1 expansion 65
Figure 53: Pressure trace IFILE 1 combustion 66
Figure 54: Torque Validation 67
Figure 55: Interpolation points for frequency response 68
Figure 56: Full spectrum of frequency response 68
Figure 57: Impulse response 69
Figure 58: Weight distribution hamming window 69
Figure 59: FIR filter output signal 70
Figure 60: Comparison premixed combustion phase 71
Figure 61: Case I - combustion chamber pressure 72
Figure 62: Case I - combustion chamber pressure rise 73
Figure 63: Case I - fuel burned in premixed combustion phase 73
Figure 64: Case I - ROHR 74
Figure 65: Case I - indicator diagram 75
Figure 66: Case I - indicated torque 75
Figure 67: Case II - combustion chamber pressure 76
Figure 68: Case II - combustion chamber pressure cut out 77
Figure 69: Case II - combustion chamber pressure rise 78
Figure 70: Case II - combustion chamber temperature 78
Figure 71: Case II - fuel burned in premixed combustion phase 79
Figure 72: Case II - ROHR 80
Figure 73: Case II - indicator diagram 80
Figure 74: Case II - indicated torque 81
Figure 75: Parameter Set I - CNI 82
Figure 76: Parameter Set I - peak cylinder pressure 82
Figure 77: Parameter Set I - high/low CNI pressure trace 83
Figure 78: Parameter Set I - FFT high/low CNI pressure trace 83
Figure 79: Parameter Set I - IMEP 84
Figure 80: Parameter Set I - fuel/cycle 84
Figure 81: Parameter Set I - indicated efficiency 85
Figure 82: Parameter Set I - evaluation of distinctive parameters over CNI 85
Figure 83: Parameter Set II - CNI 86
Figure 84: Parameter Set II - IMEP 87
Figure 85: Parameter Set II - fuel/cycle 87
Figure 86: Scheme of flexible MBD model 88
Figure 87: Gas force application illustration 89
Figure 88: Illustration evaluation nodes for simulation 90
Figure 89: Valvecover node 3809299 DOF 2 - IFILE 1 1500rpm 90
Figure 90: Valvecover node 3809299 DOF 3 - IFILE 1 1500rpm 90
Figure 91: Power unit node 1527335 DOF 3 - IFILE 1 1500rpm 91

Figure 92: Front bracket node 4127437 DOF 2 - IFILE 1 1500rpm 91
Figure 93: Valvecover node 3809299 DOF 2 - IFILE 8 1500rpm 91
Figure 94: Valvecover node 3809299 DOF 3 - IFILE 8 1500rpm 91
Figure 95: Power unit node 1527335 DOF 3 - IFILE 8 1500rpm 91
Figure 96: Front bracket node 4127437 DOF 2 - IFILE 8 1500rpm 91
Figure 97: Valvecover node 3809299 DOF 2 - IFILE 22 2000rpm 92
Figure 98: Valvecover node 3809299 DOF 3 - IFILE 22 2000rpm 92
Figure 99: Power unit node 1527335 DOF 3 - IFILE 22 2000rpm 92
Figure 100: Front bracket node 4127437 DOF 2 - IFILE 22 2000rpm 92
Figure 101: : Valvecover node 3809299 DOF 2 - IFILE 25 2000rpm 93
Figure 102: Valvecover node 3809299 DOF 3 - IFILE 25 2000rpm 93
Figure 103: Power unit node 1527335 DOF 3 - IFILE 25 2000rpm 93
Figure 104: Front bracket node 4127437 DOF 2 - IFILE 25 2000rpm 93
Figure 105: Normal Surface Velocity Levels [dB] – IFILE1 3150 Hz 94
Figure 106: Acoustic mesh - discretization 95
Figure 107: Acoustic mesh - inner elements 95
Figure 108: Acoustic mesh - outer elements 95
Figure 109: Acoustic mesh - merged outer elements 95
Figure 110: Microphone positions for ABN evaluation 96
Figure 111: Surface velocity integral - low/high knock 1500rpm 97
Figure 112: Averaged microphone sound pressures - low/high knock 1500rpm 98
Figure 113: Radiated noise and surface velocity levels - IFILE1 1202.67Hz 98
Figure 114: Radiated noise and surface velocity levels - IFILE8 1202.67Hz 98
Figure 115: Radiated noise and surface velocity levels - IFILE1 2993.32Hz 99
Figure 116: Radiated noise and surface velocity levels - IFILE8 2994.21Hz 99
Figure 117: Surface velocity integral - low/high knock 2000rpm 100
Figure 118: Averaged microphone sound pressures - low/high knock 2000rpm 100
Figure 119: Radiated noise and surface velocity levels - IFILE22 1212.47Hz 101
Figure 120: Radiated noise and surface velocity levels - IFILE25 1210.72Hz 101
Figure 121: Radiated noise and surface velocity levels - IFILE22 2979.22Hz 101
Figure 122: Radiated noise and surface velocity levels - IFILE25 2974.92Hz 101
Figure 123: Surface velocity integral - injection variation rail pressure 1500rpm 102
Figure 124: Averaged microphone sound pressures - injection variation rail pressure 1500rpm 102
Figure 125: Radiated noise and surface velocity levels – InjVarPress - 1000bar 2011.92Hz 103
Figure 126: Radiated noise and surface velocity levels – InjVarPress - 1100bar 2016.73Hz 103
Figure 127: Radiated noise and surface velocity levels – InjVarPress - 1200bar 2023.99Hz 103
Figure 128: Radiated noise and surface velocity levels – InjVarPress - 1300bar 2027.33Hz 103
Figure 129: Surface velocity integral - injection variation SOI pilot injection 1500rpm 104
Figure 130: Averaged microphone sound pressures - injection variation SOI pilot injection 1500rpm 105
Figure 131: Radiated noise and surface velocity levels – InjVarSOIPI - -10degCA 2307.35Hz 106
Figure 132: Radiated noise and surface velocity levels - InjVarSOIPI - -5degCA 2307.00Hz 106
Figure 133: Radiated noise and surface velocity levels - InjVarSOIPI - 0degCA 2307.00Hz 106
Figure 134: Calibration pressure trace IFILE 1 116
Figure 135: Calibration pressure trace IFILE 2 116

Figure 136: Calibration pressure trace IFILE 3 116
Figure 137: Calibration pressure trace IFILE 4 116
Figure 138: Calibration pressure trace IFILE 5 117
Figure 139: Calibration pressure trace IFILE 6 117
Figure 140: Calibration pressure trace IFILE 7 117
Figure 141: Calibration pressure trace IFILE 8 117
Figure 142: Calibration pressure trace IFILE 9 117
Figure 143: Calibration pressure trace IFILE 10 117
Figure 144: Calibration pressure trace IFILE 11 118
Figure 145: Calibration pressure trace IFILE 12 118
Figure 146: Calibration pressure trace IFILE 13 118
Figure 147: Calibration pressure trace IFILE 14 118
Figure 148: Calibration pressure trace IFILE 16 118
Figure 149: Calibration pressure trace IFILE 17 118
Figure 150: Calibration pressure trace IFILE 18 119
Figure 151: Calibration pressure trace IFILE 19 119
Figure 152: Calibration pressure trace IFILE 20 119
Figure 153: Calibration pressure trace IFILE 22 119
Figure 154: Calibration pressure trace IFILE 23 119
Figure 155: Calibration pressure trace IFILE 24 119
Figure 156: Calibration pressure trace IFILE 25 120
Figure 157: Calibration pressure trace IFILE 26 120
Figure 158: Calibration pressure trace IFILE 27 120
Figure 159: Valvecover node 3809299 DOF 2 - IFILE 1 1500rpm 121
Figure 160: Valvecover node 3809299 DOF 3 - IFILE 1 1500rpm 121
Figure 161: Power unit node 1527335 DOF 3 - IFILE 1 1500rpm 121
Figure 162: Front bracket node 4127437 DOF 2 - IFILE 1 1500rprm 121
Figure 163: Valvecover node 3809299 DOF 2 - IFILE 8 1500rpm 122
Figure 164: Valvecover node 3809299 DOF 3 - IFILE 8 1500rpm 122
Figure 165: Power unit node 1527335 DOF 3 - IFILE 8 1500rpm 122
Figure 166: Front bracket node 4127437 DOF 2 - IFILE 8 1500rprm 122
Figure 167: Valvecover node 3809299 DOF 2 - IFILE 22 2000rpm 122
Figure 168: Valvecover node 3809299 DOF 3 - IFILE 22 2000rpm 122
Figure 169: Power unit node 1527335 DOF 3 - IFILE 22 2000rpm 123
Figure 170: Front bracket node 4127437 DOF 2 - IFILE 22 2000rprm 123
Figure 171: Valvecover node 3809299 DOF 2 - IFILE 25 2000rpm 123
Figure 172: Valvecover node 3809299 DOF 3 - IFILE 25 2000rpm 123
Figure 173: Power unit node 1527335 DOF 3 - IFILE 25 2000rpm 123
Figure 174: Front bracket node 4127437 DOF 2 - IFILE 25 2000rprm 123

15 List of Tables

Table 1: Bark Scala [19] 35
Table 2: Speeds and number of injections for the measured engine 50
Table 3: Injection variation timings for combustion calibration 51
Table 4: IFILE 1 - low CNI cycle 55
Table 5: IFILE 1 - high CNI cycle 55
Table 6: Mean sound pressure - IFILE1 56
Table 7: IFILE 8 - low CNI cycle 56
Table 8: IFILE 8 - high CNI cycle 56
Table 9: Mean sound pressure - IFILE8 57
Table 10: Basic physical engine data 60
Table 11: Calibrated pressure traces - CNI Levels 71
Table 12: CNI Assessment Test Plan 72
Table 13: Case I - CNI Levels 74
Table 14: Case II - injection data 76
Table 15: Case II - CNI Levels 79
Table 16: Parameter Set I 81
Table 17: Parameter Set II 81
Table 18: Calibrated cylinder pressure traces 1500rpm - knocking indices 97
Table 19: Calibrated cylinder pressure traces 2000rpm - knocking indices 99
Table 20: Injection variation rail pressure 1500rpm - knocking indices 101
Table 21: Injection variation SOI PI 1500rpm - knocking indices 104
Table 22: 1/3 Octave frequency bands [27] 124

16 References

[1] B. Shin, I. Jung, S. Pyo and Y. Chi, "A Study of Combustion Control Parameter Optimization in a Diesel Engine Using Cylinder Pressure," SAE Technical Paper 2014-01-1352, 2014.

[2] M. Russel and R. Haworth, "Combusiton Noise from High Speed Direct Injeciton Diesel Engines," SAE Technical Paper 850973, 1985.

[3] S. S. Khaira, A. Singh and M. Jansons, "Effect on Injection Parameters and Strategy on the Noise from a Single Cylinder Direct Injection Diesel Engine," ASME, Detroit, 2011.

[4] G. P. Merker and R. Teichmann, Grundlagen Verbrennungsmotoren, Springer Vieweg, 2014.

[5] R. Pischinger, M. Klell and T. Sams , Thermodynamik der Verbrennungskraftmaschine, Springer, 2009.

[6] C. Poetsch, "Crank-Angle Resolved Modeling of Fuel Injection and Mixing Controlled Combustion for Real-Time Application In Steady-State and Transient Operation," SAE Technical Paper 2014-01-1095, 2014.

[7] P. Kožuch , "Ein phänomenologisches Modell zur kombinierten Stickoxid- und Rußberechnung bei direkteinspritzenden Dieselmotoren," Dissertatioin, Universität Stuttgart, 2004.

[8] H. W. Notz, "Beitrag zur experimentellen Ermittlung des Einspritzverlaufs am schnelllaufenden Dieselmotor," Dissertation, Technische Universität München, 1986.

[9] AVL List GmbH, "CruiseM Theory Guide," Graz, 2018.

[10] C. Poetsch and T. Katrasnik, "Crank-Angle Resolved Modeling of Fuel Injection, Combustion and Emission Formation for Engine Optimization and Calibration on Real-Time Systems," SAE Technical Paper 2016-01-0558, 2016.

[11] J. Pastor, J. Lopez, J. Garcia and J. Pastor, "A 1D model of the description of mixing-controlled inert diesel sprays," Fuel 87 2871-2885, 2008.

[12] G. Pirker, F. Chmela and A. Wimmer, "ROHR Simulation for DI Diesel Engines Based on Sequential Combustion Mechanisms," SAE Technical Paper 2006-01-0654, 2006.

[13] T. Katrašnik, "An innovative 0D transient momentum based spray model for real-time simulations of CI Engines under review in Energy".

[14] T. Katrašnik, "An advanced real-time capable mixture controlled combusiton model.," Energy, 2016.

[15] AVL List GmbH, "Excite Power Unit Theory Guide," Graz, 2018.

[16] AVL List GmbH, "Excite Acoustics Theory Guide," Graz, 2018.

[17] T. Mocsai, F. Diwoky and H. H. Priebsch, "The application of the Wave Based Technique for 3D free-field radiation calculation using a residual error controlled adaptive strategy," ISMA, 2010.

[18] J. Rejlek, T. Mocasai, P. Silar, A. Hepberger and H. -H. Priebsch, "Wave Based Prediction Technique for Sound Radiation Analysis," NAGDAGA, 2009.

[19] R. Lerch, G. Sessler and D. Wolf, Technische Akustik, Springer, 2009.

[20] M. Möser, Technische Akustik, Springer, 2015.

[21] E. Zwicker, Psychoakustik, Berlin, Heidelberg, New York: Springer, 1982.

[22] A. Brandt, Noise and Vibration Analysis: Signal Analysis and Experimental Procesures, Wiley, 2011.

[23] S. W. Smith, The Scientist and Engineer's Guide to Digital Signal Processing, Bertrams, 1997.

[24] P. Langjahr, "Optimierung und Echtzeit-Realisierung eines Berechnungsmodells zur Bestimmung des Nagelgeräusches von Dieselmotoren," Masterarbeit, Universität für Musik und darstellende Kunst, Graz, 2014.

[25] M. Pflüger, F. Brandl, U. Bernhard and K. Feitzelmayer, Fahrzeugakustik, Springer.

[26] O. Thiam, S. Wang, F. Levy and J.-B. Blaisot, "Investigation of the Influence of Engine Parameters on the Diesel Combustion Noise," EAEC, 2011.

[27] AVL List GmbH, "Impress Chart Users Guide," Graz, 2019.

[28] AVL List GmbH, "CruiseM Theory Guide Version 2018.1," Graz.

[29] I. Jung, J. Jin, H. So, C. Nam and K. Won, "An Advanced Methond for Developing cpombustion Noise through the Analysis of Diesel Combustion," SAE International, 2013.

[30] S. Brandl and T. Resch, "Diesel Combustion Noise," in *AVL NVH Tech Day*, Paris.

[31] E. Köher and R. Flierl, Verbrennungsmotoren.

17 Appendix

17.1 Combustion Calibration

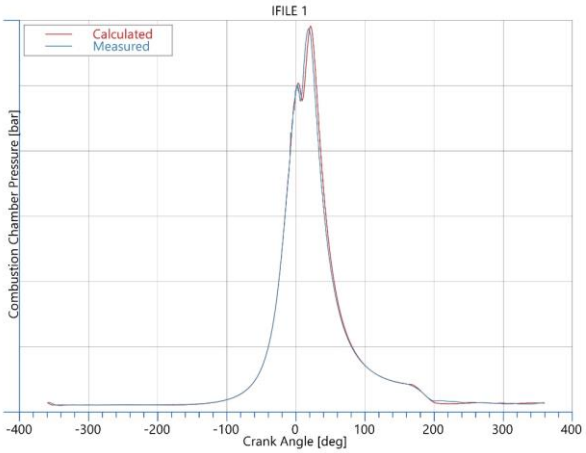

Figure 134: Calibration pressure trace IFILE 1

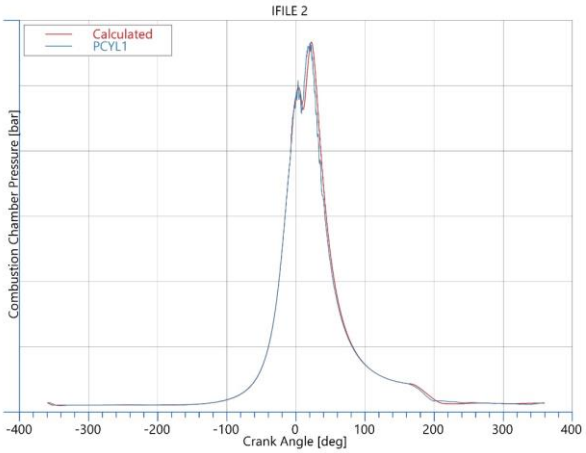

Figure 135: Calibration pressure trace IFILE 2

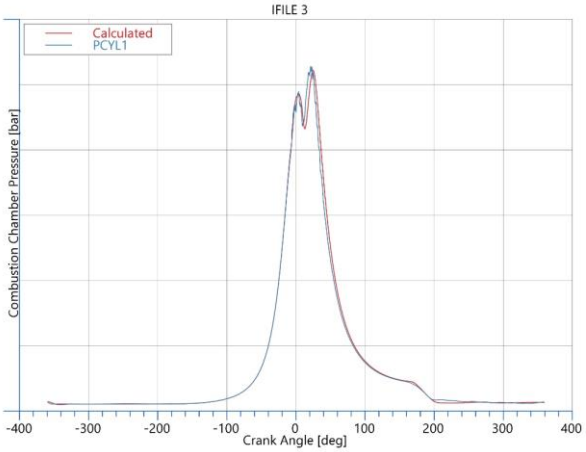

Figure 136: Calibration pressure trace IFILE 3

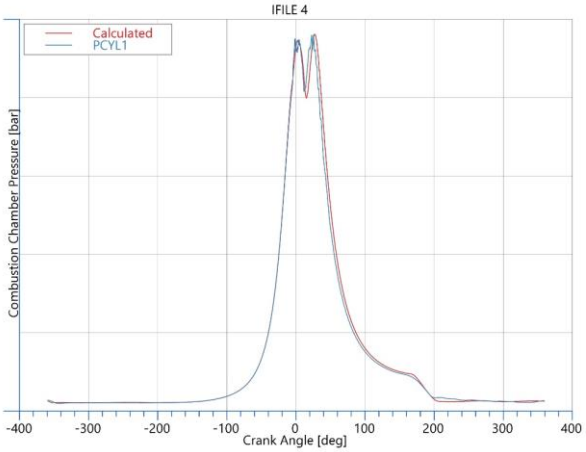

Figure 137: Calibration pressure trace IFILE 4

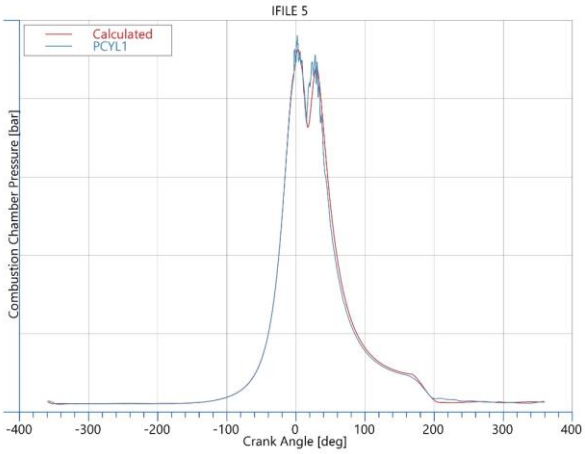

Figure 138: Calibration pressure trace IFILE 5

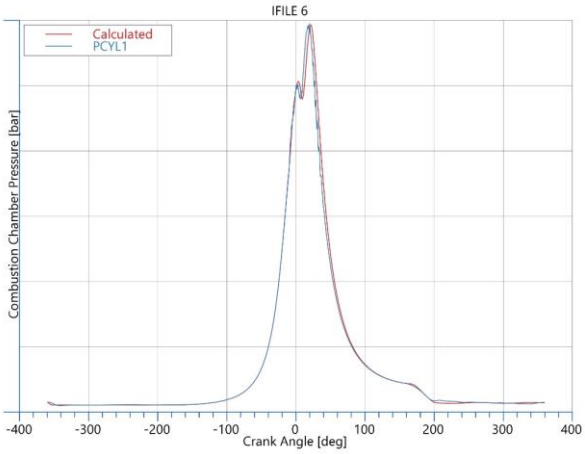

Figure 139: Calibration pressure trace IFILE 6

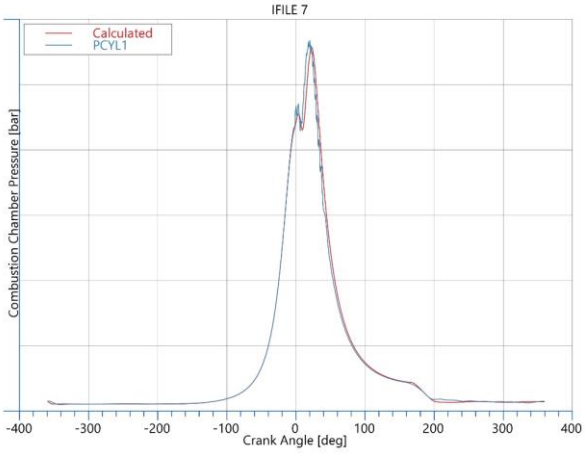

Figure 140: Calibration pressure trace IFILE 7

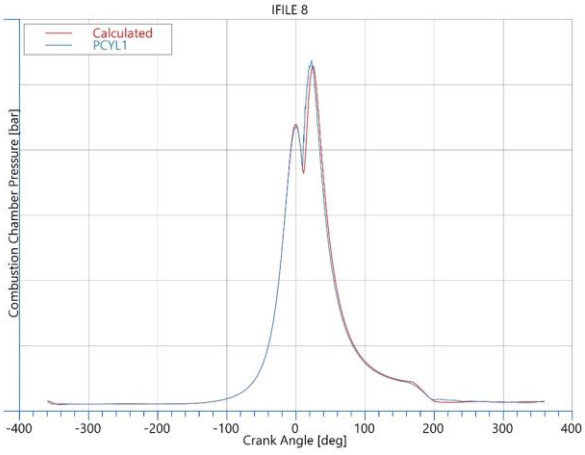

Figure 141: Calibration pressure trace IFILE 8

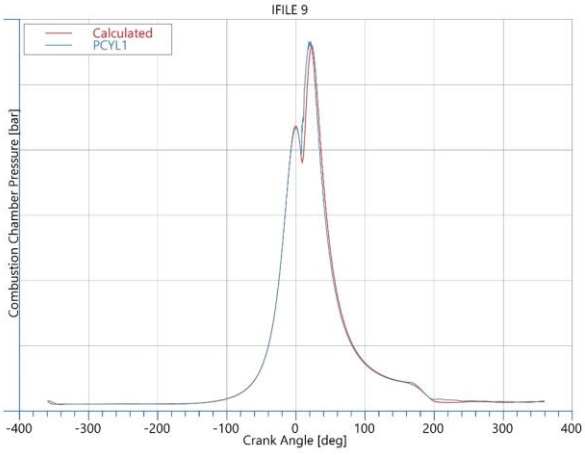

Figure 142: Calibration pressure trace IFILE 9

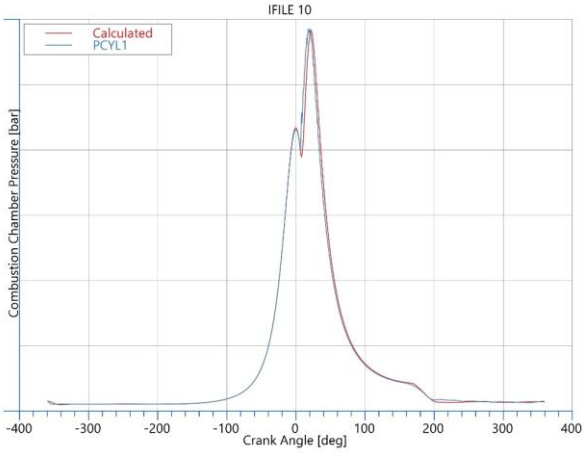

Figure 143: Calibration pressure trace IFILE 10

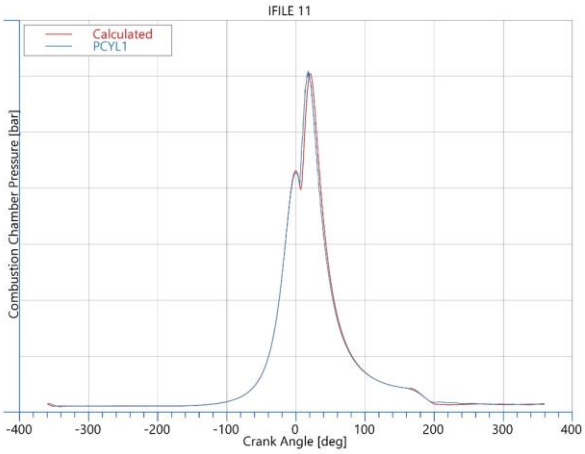

Figure 144: Calibration pressure trace IFILE 11

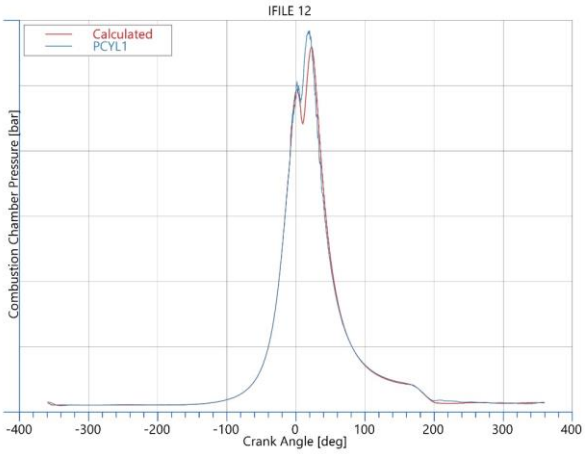

Figure 145: Calibration pressure trace IFILE 12

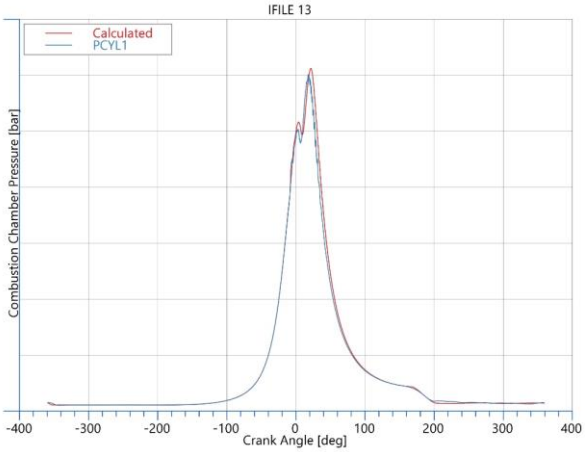

Figure 146: Calibration pressure trace IFILE 13

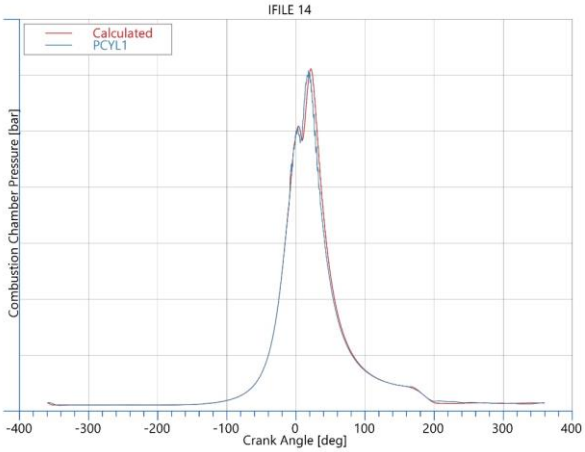

Figure 147: Calibration pressure trace IFILE 14

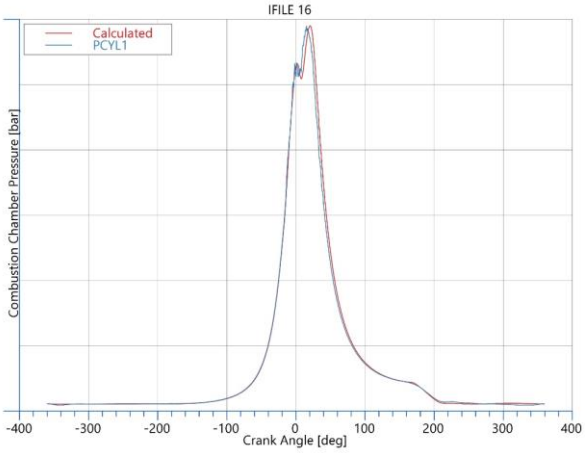

Figure 148: Calibration pressure trace IFILE 16

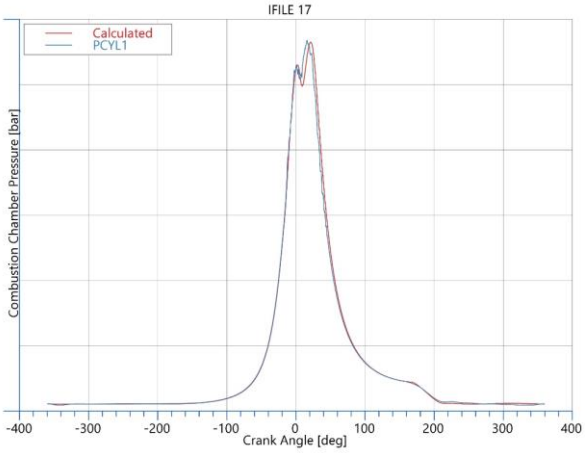

Figure 149: Calibration pressure trace IFILE 17

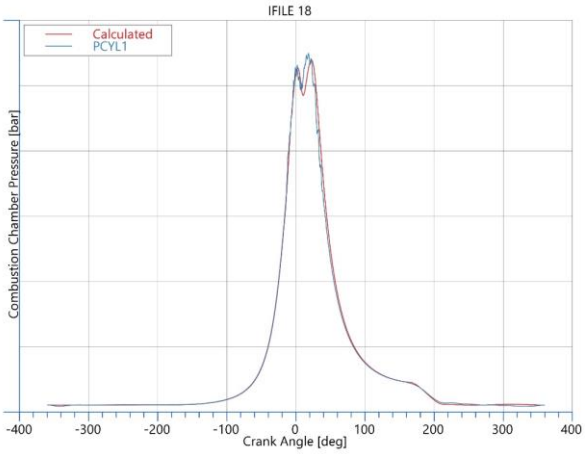

Figure 150: Calibration pressure trace IFILE 18

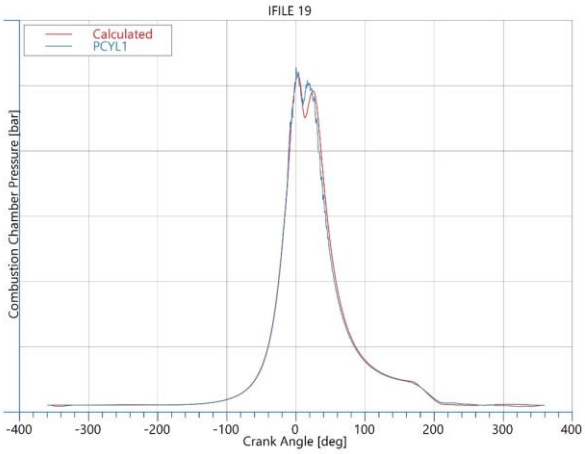

Figure 151: Calibration pressure trace IFILE 19

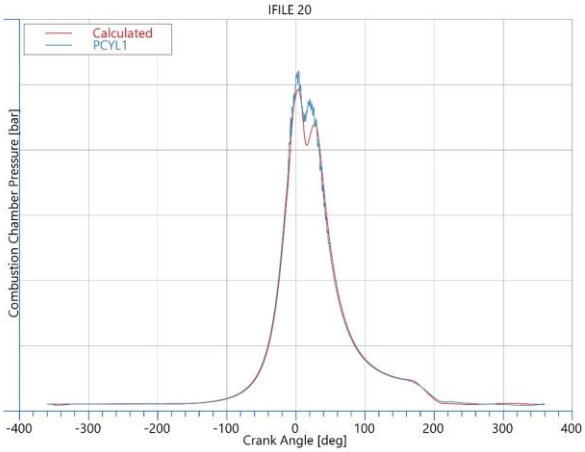

Figure 152: Calibration pressure trace IFILE 20

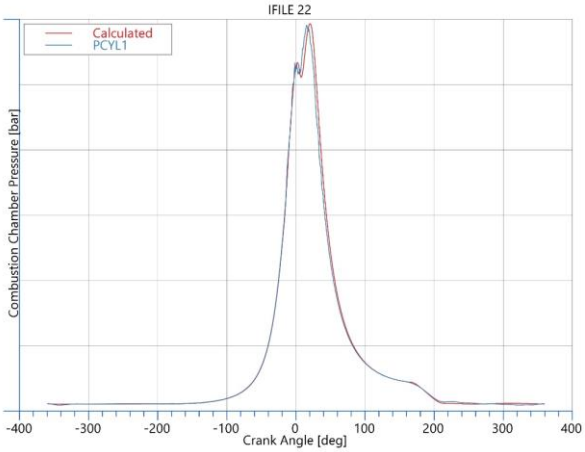

Figure 153: Calibration pressure trace IFILE 22

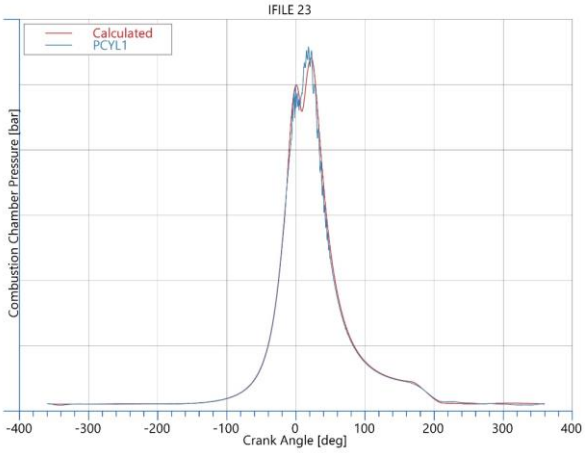

Figure 154: Calibration pressure trace IFILE 23

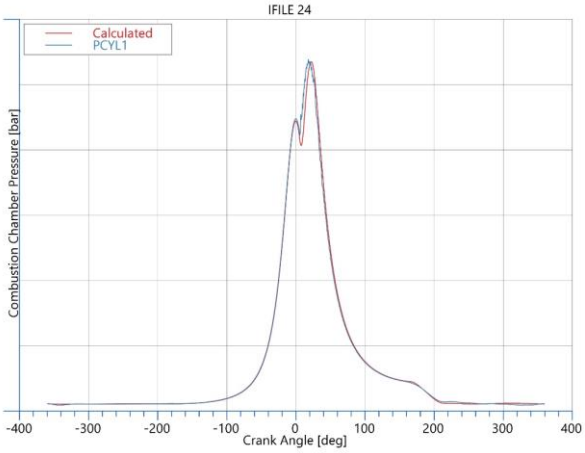

Figure 155: Calibration pressure trace IFILE 24

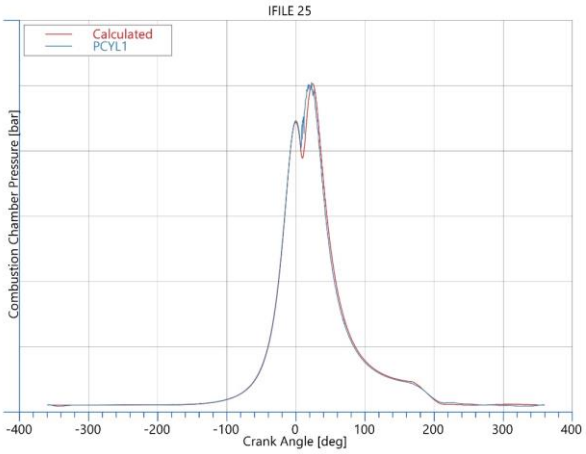

Figure 156: Calibration pressure trace IFILE 25

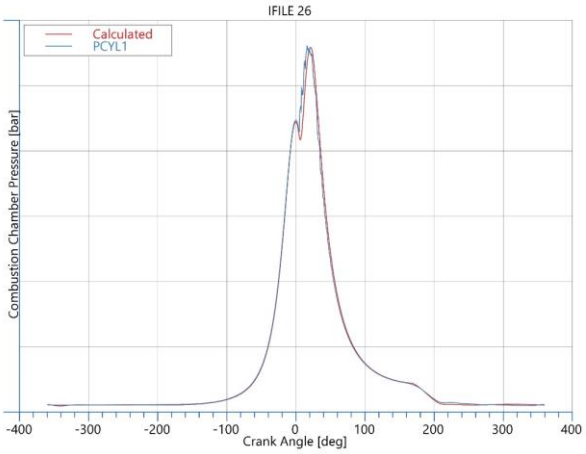

Figure 157: Calibration pressure trace IFILE 26

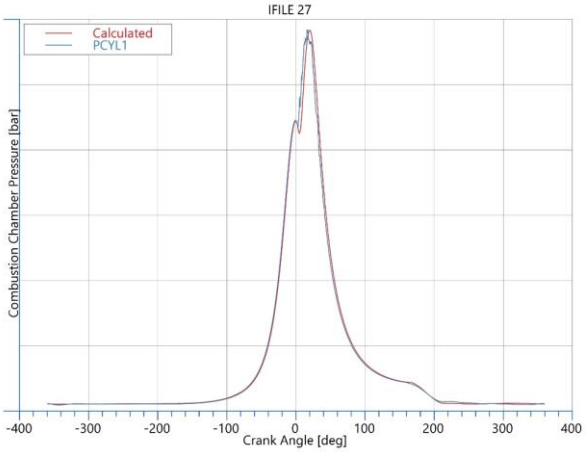

Figure 158: Calibration pressure trace IFILE 27

17.2 MBD Model Comparison Acceleration Signal Time Domain

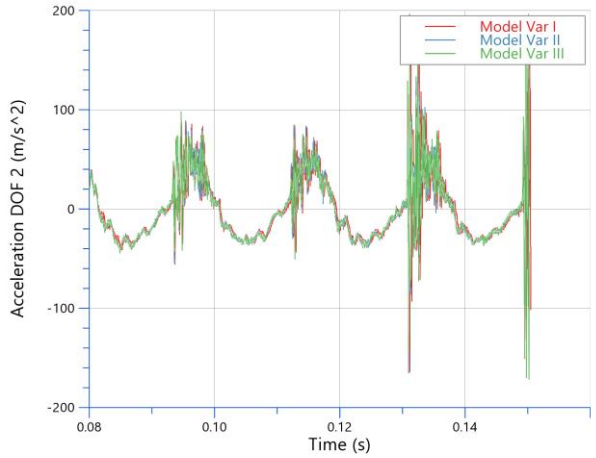

Figure 159: Valvecover node 3809299 DOF 2 - IFILE 1 1500rpm

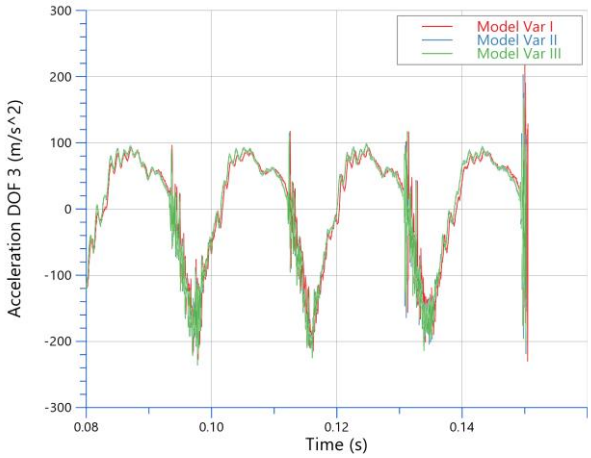

Figure 160: Valvecover node 3809299 DOF 3 - IFILE 1 1500rpm

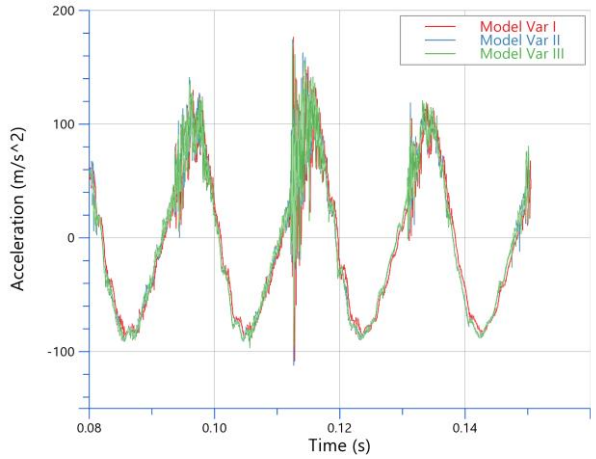

Figure 161: Power unit node 1527335 DOF 3 - IFILE 1 1500rpm

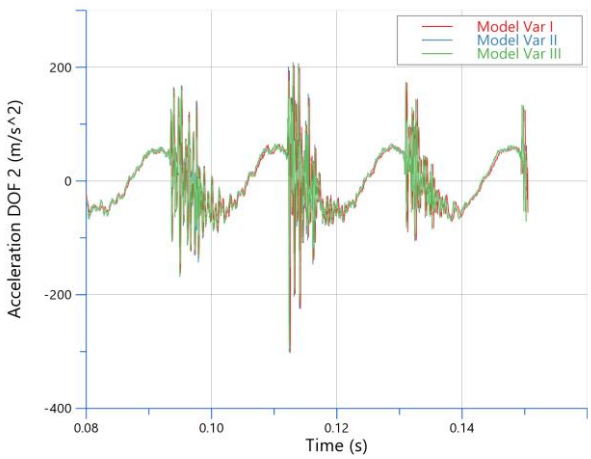

Figure 162: Front bracket node 4127437 DOF 2 - IFILE 1 1500rprm

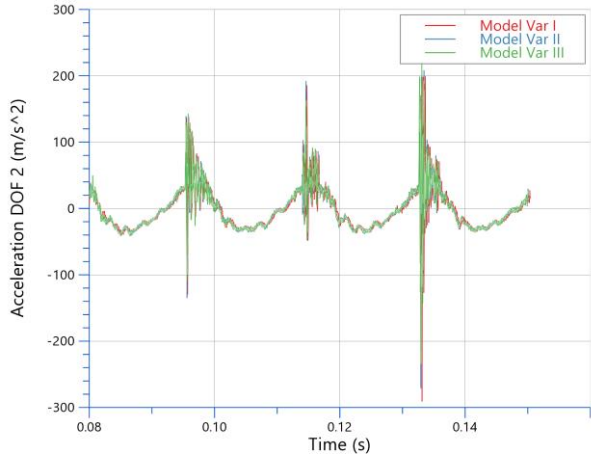

Figure 163: Valvecover node 3809299 DOF 2 - IFILE 8 1500rpm

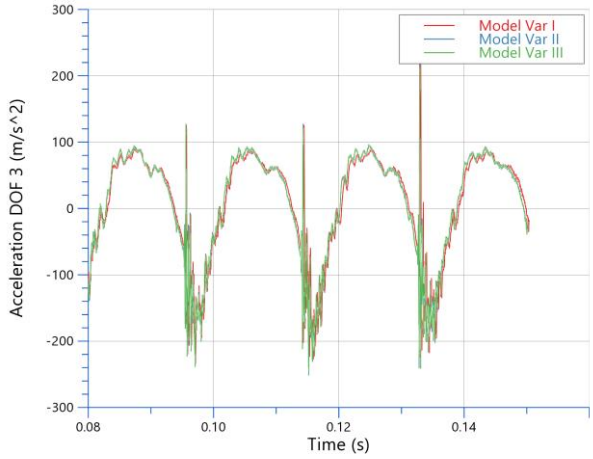

Figure 164: Valvecover node 3809299 DOF 3 - IFILE 8 1500rpm

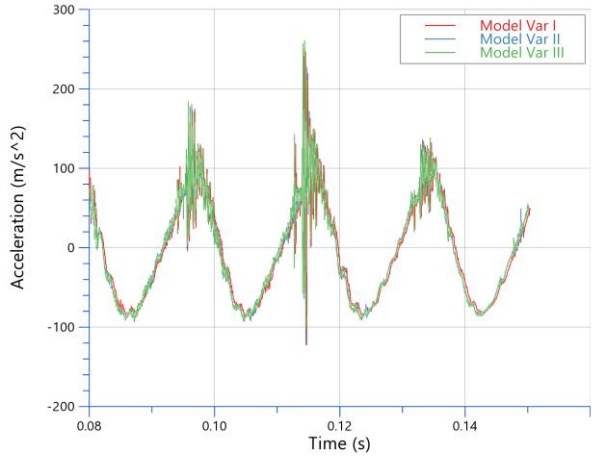

Figure 165: Power unit node 1527335 DOF 3 - IFILE 8 1500rpm

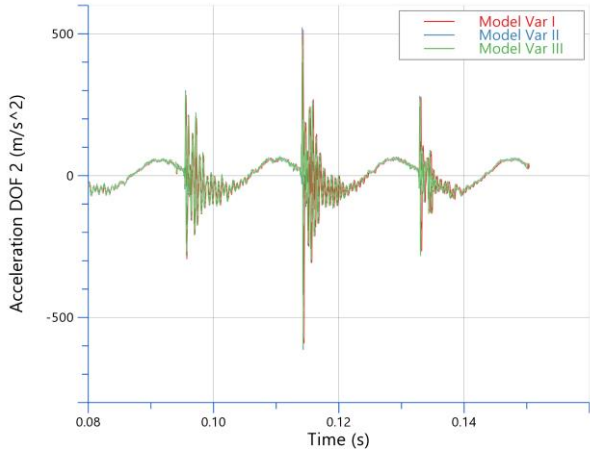

Figure 166: Front bracket node 4127437 DOF 2 - IFILE 8 1500rprm

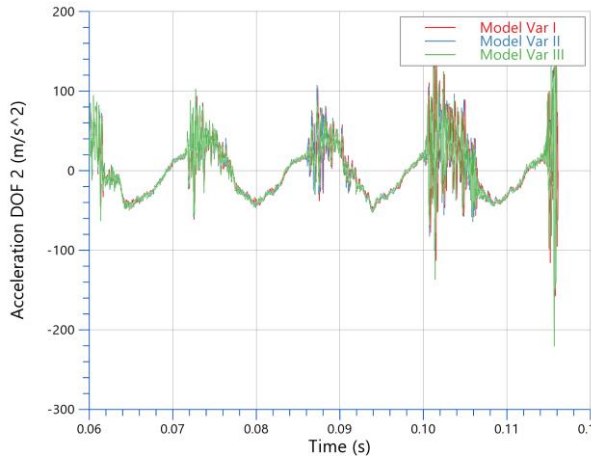

Figure 167: Valvecover node 3809299 DOF 2 - IFILE 22 2000rpm

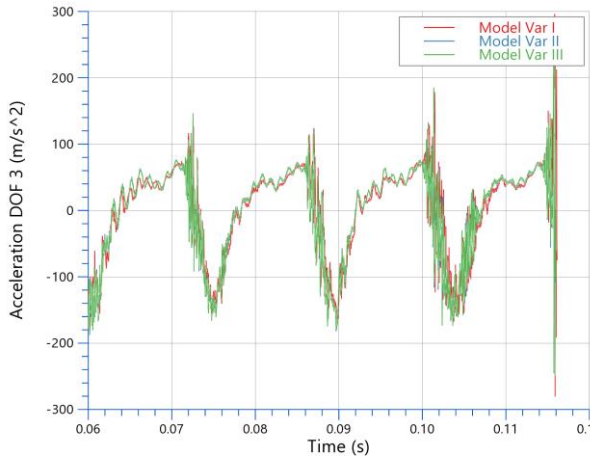

Figure 168: Valvecover node 3809299 DOF 3 - IFILE 22 2000rpm

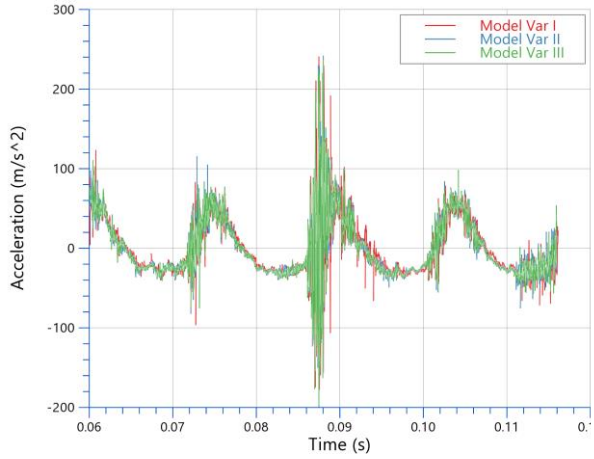

Figure 169: Power unit node 1527335 DOF 3 - IFILE 22 2000rpm

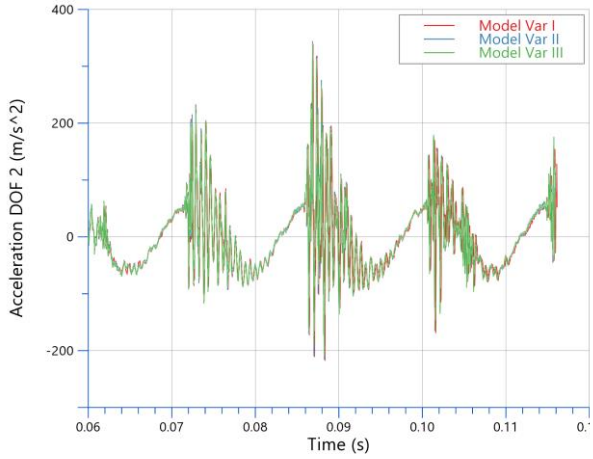

Figure 170: Front bracket node 4127437 DOF 2 - IFILE 22 2000rprm

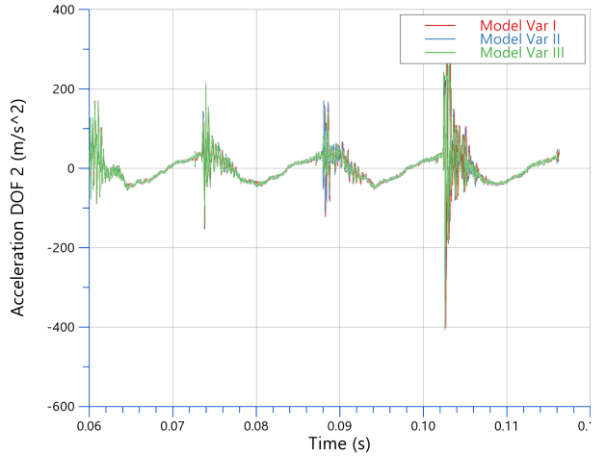

Figure 171: Valvecover node 3809299 DOF 2 - IFILE 25 2000rpm

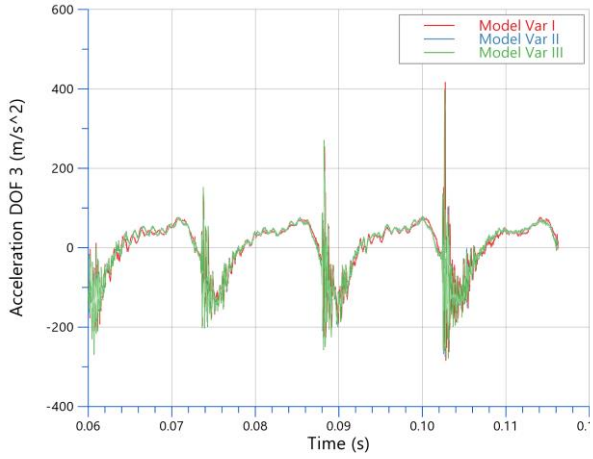

Figure 172: Valvecover node 3809299 DOF 3 - IFILE 25 2000rpm

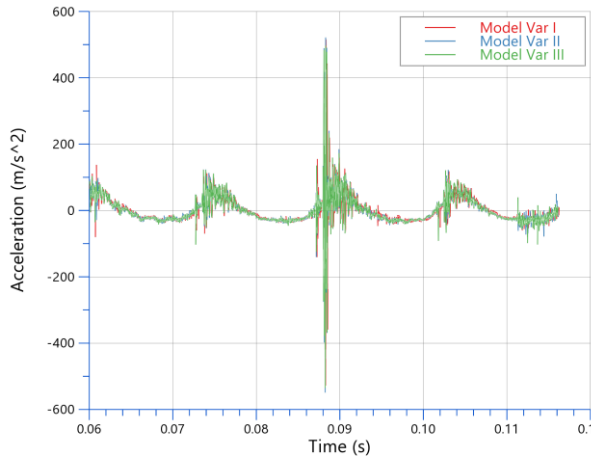

Figure 173: Power unit node 1527335 DOF 3 - IFILE 25 2000rpm

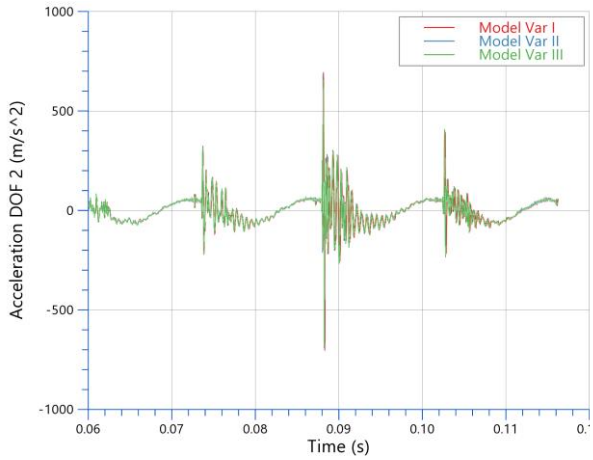

Figure 174: Front bracket node 4127437 DOF 2 - IFILE 25 2000rprm

17.3 1/3 Octave Frequency Bands

Table 22: 1/3 Octave frequency bands [27]

1/3 Octave Number [-]	Center Frequency [Hz]	Lower Frequency [Hz]	Upper Frequency [Hz]
1	16	14.1	17.8
2	20	17.8	22.4
3	25	22.4	28.2
4	31.5	28.2	35.5
5	40	35.5	44.7
6	50	44.7	56.2
7	63	56.2	70.7
8	80	70.7	89.1
9	100	89.1	112
10	125	112	141
11	160	141	178
12	200	178	224
13	250	224	282
14	315	282	355
15	400	355	447
16	500	447	562
17	630	562	708
18	800	708	891
19	1000	891	1122
20	1250	1122	1413
21	1600	1413	1778
22	2000	1778	2239
23	2500	2239	2818
24	3150	2818	3548
25	4000	3548	4467